UNIVERSITEIT VAN PRETORIA
UNIVERSITY OF PRETORIA
YUNIBESITHI YA PRETORIA

An optical investigation of implantation damage in GaAs superlattices

by

Kibreab Mebrahtom Haile

Submitted in partial fulfilment of the requirements for the degree

Magister Scientiae

in the Faculty of Natural and Agricultural Science
University of Pretoria
Pretoria

February 2004

© University of Pretoria

UNIVERSITEIT VAN PRETORIA
UNIVERSITY OF PRETORIA
YUNIBESITHI YA PRETORIA

An optical investigation of implantation damage in GaAs superlattices

by

Kibreab Mebrahtom Haile

Supervisor: Professor D. J. Brink

Faculty: Natural and Agricultural Sciences

Department: Physics

Degree: Magister Scientiae

Abstract

In this work tunability, implantation damage and recovery of GaAs doping superlattices implanted with hydrogen ions were studied. The applicability of two models of the optical properties of semiconductors was also investigated. GaAs doping superlattices were implanted with 0.5 MeV hydrogen ions at doses of $10^{12}\ cm^{-2}$, $10^{14}\ cm^{-2}$ and $10^{16}\ cm^{-2}$. This gradually modifies their optical characteristics from superlattice behaviour to something resembling the bulk material and beyond. Such a processing technique therefore provides a convenient way of tuning the optical properties of a superlattice semi-permanently. A combined result of ellipsometry and near infrared reflectance measurements showed that a single effective oscillator as well as a more advanced three-parameter model could be applied to the virgin and ion-implanted doping superlattices. This allowed us to determine the dose dependent effective band gap as well as other model parameters. Photoluminescence as well as normal and resonance Raman techniques were applied to study hydrogen ion implantation damage and its recovery. These techniques showed that implantation damage could be reversed to a large extent by a simple thermal annealing step.

Acknowledgements

I would like to thank the following for their contribution towards the completion of this study:

1. My supervisor, professor D. J. Brink for his helpful guidance and support during this study.
2. My parents, brothers and sisters for their support and encouragement.

Contents

CHAPTER 1:

Introduction

1.1. Dispersion Theory..3

1.2. Refractive Index Measurement Above Band Gap...............................4

1.3. Photoluminescence And Raman Scattering..5

CHAPTER 2:

Dispersion Theory

2.1. Optical Constants...8

2.2. Kramers-Kronig Relations...10

2.3. Theoretical Models For The Evaluation Of Refractive Index...............10

2.3.1- Sellmeier Equation...11

2.3.2- Single-Oscillator Model...11

2.3.3- Modified Single Oscillator Model....................................12

2.4. Reflectance R...16

2.4.1- Reflection at a planer interface between two isotropic media.......16

2.4.2- Reflection by an ambient-film-substrate system.......................19

CHAPTER 3:

Ellipsometry And Polarized Light

3.1. Uniform Transverse-Electric (TE) Plane Waves Of Light......................23

3.1.1- The Jones Vector of a Uniform TE Plane Wave.......................23

3.1.2- The Wave Intensity...26

3.1.3- State of Polarization..26

3.2. Propagation of Polarized Light Through Polarizing Optical System.......27
3.2.1- Transmission Type device...27
3.2.2- Reflection Type Device...30
3.3. Operating Principle Of The Ellipsometer...................................32
3.3.1- Ellipsometry Transmission 32
3.4. Null Ellipsometry...35

CHAPTER 4:

Theoretical Considerations On Doping Superlattices

4.1- Structure Of A Doping Superlattice.......................................38
4.2- Electronic Structures...39
4.2.1- Self Consistent Calculation.......................................39
4.2.2- Effective Width Approximation...................................44
4.2.3- The Pumping Factor – r..48

CHAPTER 5:

Sample Parameters, Experimental Set-up, Measuring Techniques And Equipment Used

5.1. Sample Parameters...51
5.1.1- Growth of GaAs Doping Superlattice by OMVPE.................51
5.1.2- Post Growth Modification Of Doping GaAs Superlattice.........52
5.2. Refractive Index Measurements...53
5.2.1- Experimental Set-up...53
5.2.2- Equipment..54
5.2.3- Experimental Techniques...55

5.3. Near IR Reflectance Measurements..........59
5.3.1- Experimental Set-up..........59
5.3.2- Equipment..........60
5.3.3- Experimental Techniques..........61
5.3.4- Reflectance Calculation..........63
5.4 Photoluminescence And Resonance Raman Measurements..........63
5.4.1- Experimental Set-up..........63
5.4.2- Equipment..........64
5.4.3- Experimental Techniques..........65
5.5. Normal Raman Measurement..........66
5.5.1- Experimental Set-up..........67
5.5.2- Experimental Techniques..........68

CHAPTER 6:

Results And Discussion

6.1. Ellipsometry Measurement..........70
6.1.1- Evaluation of Ellipsometric Angles And Graphical Representation..........70
6.1.2- Graphical Comparison of Extinction Coefficient Values..........76
6.1.3- Optical Constants..........76
6.2. Near Infrared Reflectance Measurement..........78
6.2.1- Reflectance Spectrum..........78
6.2.2- Evaluation of Real Refractive Index..........81
6.3. Photoluminescence And Raman Measurements..........88
6.3.1a- Photoluminescence Measurement Before Annealing..........88
6.3.1b- Photoluminescence Measurement After Annealing..........91

6.3.2a- Normal Raman Measurement Before Annealing 93
6.3.2b- Normal Raman Measurement After Annealing.....................94
6.3.2c- Resonance Raman Measurement 95

CHAPTER 7:

Conclusion..100
Suggestion For Future Work...101

APPENDICES:

Appendix A..102
Appendix B..108

REFERENCES...110

UNIVERSITEIT VAN PRETORIA
UNIVERSITY OF PRETORIA
YUNIBESITHI YA PRETORIA

List of tables

6.1a. Slope of the Δ curves around $\Delta = 90^0$ for figures 6.1, 6.2 and 6.4..............72

6.1b. Optical constants n and k determined by ellipsometry

for bulk, virgin and ion implanted DSL's..77

6.2a. Single effective oscillator (SEO) parameter for bulk,

virgin and ion implanted DSL's..84

6.2b. Values for the Afromowitz parameters for bulk, virgin

and ion implanted DSL's...86

List of figures

2.1 The reciprocal susceptibility of bulk GaAs plotted versus $(E / E_p)^2$ 13
2.2 Representation of the $\varepsilon_2(E)$ spectrum of GaAs......................................15
2.3 Oblique reflection and transmission of a plane wave at the planar interface between two semi-infinite media 0 and 1..............................17
2.3 Oblique reflection and transmission of a plane wave by ambient-film-substrate system with parallel-plane boundaries.......................19

3.1 The PCSA (polarizer-compensator-sample (system)-analyzer) ellipsometer arrangement..31

4.1 Schematic diagram for n-p doping superlattice at ground state.....................42
4.2 Schematic diagram showing (a) doping profile (b) space-charge distribution and (c) band profile versus growth direction Z........................45

5.1 Layer sequence in the n-p doping superlattices......................................52
5.2 The Gartner Ellipsometer Model L 119..53
5.3 Schematic layout for the ellipsometry experiment...................................54
5.4 Schematic layout of 0.64 m Jobin Yvon Monochromator...........................61
5.5 Experimental layout for the near IR reflectance measurements showing all the equipment used...62
5.6 Schematic layout for photoluminescence and resonant Raman measurement...63
5.7 Photomultiplier multiplication process...65
5.8 Schematic layout of a typical experimental setup used in Raman scattering experiments...67

6.1 Best fit of model parameters to the experimental ellipsometric-angles for bulk GaAs with a He-Ne laser beam at 632.8 nm (a) 594nm (b) and 543.5nm (c)....72

6.2 Best fit of model parameters to the experimental ellipsometric-angles for virgin (a) and ion implanted GaAs DSL's samples, dose = $10^{12}\,cm^{-2}$ (b) (He-Ne at 632.8nm)....73

6.3 Best fit of model parameters to the experimental ellipsometric-angles for ion implanted GaAs DSL's, dose = $10^{14}\,cm^{-2}$ (c) and $10^{16}\,cm^{-2}$ (d) (He-Ne at 632.8nm)....73

6.4 Best fit of model parameters to the experimental ellipsometric-angles for virgin (a) and ion implanted GaAs DSL's samples, dose = $10^{12}\,cm^{-2}$ (b) (He-Ne at 594 nm)....74

6.5 Best fit of model parameters to the experimental ellipsometric-angles for ion implanted GaAs DSL's, dose = $10^{14}\,cm^{-2}$ (c) and $10^{16}\,cm^{-2}$ (d) (He-Ne at 594 nm)....74

6.6 Best fit of model parameters to the experimental ellipsometric-angles for virgin (a) and ion implanted GaAs DSL's samples, dose = $10^{12}\,cm^{-2}$ (b) (He-Ne at 543.5 nm)....75

6.7 Best fit of model parameters to the experimental ellipsometric-angles for ion implanted GaAs DSL's, dose = $10^{14}\,cm^{-2}$ (c) and $10^{16}\,cm^{-2}$ (d) (He-Ne at 543.5 nm)....75

6.8 Near infrared room temperature reflectance spectra for bulk GaAs and a virgin doping superlattice....80

6.9 Near infrared room temperature reflectance spectra for hydrogen ion-implanted GaAs doping superlattices....80

6.10 Plot of inverse susceptibility $\chi^{-1} = (n^2 - 1)^{-1}$ versus photon energy squared (E^2) for bulk GaAs and for a virgin doping superlattice..................82

6.11 Plots of inverse susceptibility $\chi^{-1} = (n^2 - 1)^{-1}$ versus $(E / E_p)^2$ for bulk GaAs..82

6.12 Plot of inverse susceptibility $\chi^{-1} = (n^2 - 1)^{-1}$ versus E^2 for hydrogen ion implanted GaAs doping superlattice..............................84

6.13 Plot of refractive index versus photon energy for bulk, virgin DSL and hydrogen ion implanted GaAs doping superlattice.............................87

6.14 Photoluminescence spectra of virgin and ion-implanted DSL's (DSLH12, DSLH14 and DSLH16)..89

6.15 Recovery of ion-implanted DSL's after thermal annealing according to PL measurements for ion-implanted DSL's.........................92

6.16 Raman spectra of virgin and ion implanted DSL excited by 514 nm laser light and recorded in the back scattering configuration.......................93

6.17 Raman spectra for 514 nm laser excitation after thermal annealing at 500^0..95

6.18 Single particle resonant Raman spectra of ion implanted DSL's excited by 632.8 nm laser light in a Z(XZ)X 90^0 scattering configuration...............97

6.19 Recovery of ion-implanted DSL's after thermal annealing at $500^0 C$ according to single particle resonant scattering....................................98

CHAPTER 1

Introduction

1.1. Dispersion Theory..3

1.2. Refractive Index Measurement Above Band Gap....................4

1.3. Photoluminescence And Raman Scattering...........................5

CHAPTER 1

Introduction

Extensive theoretical and experimental studies of a different type of artificial semiconductor in the form of a superlattice composed of ultrathin n-and p-doped homogeneous semiconductor layers have recently been made [1-3]. These superlattices have a number of interesting properties such as a tunable effective band gap, long lifetime of photoexcited carriers, quantization of carriers in space-charge induced-potential wells, a tunable two-dimensional electronic subband structure and tunable absorption coefficients. Electrons and holes are spatially separated (indirect gap in real space). Due to the spatial separation of electrons and holes, the compensating charge of excess carriers that are induced electrically or optically, decreases the amplitude of the space-charge-induced superlattice potential and thus increases the effective gap. In our present work the possibility of tuning the doping superlattice properties semi-permanently by subjecting it to high-energy (0.5Mev) hydrogen ion implantation is studied. Different implantation doses were used to shift the effective band gap from its ground state value to that of the bulk material.

The doping superlattices (DLS) used in this experiment have the following design parameters: thickness $d_n = d_p = 40nm$, DSL's period $80nm$, number of periods 30 and total DSL thickness $2.4\mu m$. The n layers were doped with Te: $n_D = 10^{18} cm^{-3}$, whereas the p-layers were doped with Zn: $n_A = 10^{18} cm^{-3}$.

The main theoretical and experimental approaches used in this work are discussed in chapters two to five. Chapter 6 provides a discussion and interpretation of the experimental results. The rest of this chapter is intended to give a brief introduction to the main concepts and techniques used in this work.

1.1- Dispersion Theory

The optical constants, such as the real refractive index n, extinction coefficient k, absorption coefficient α, and reflectance R, are of great technological importance for various optical and optoelectronic device applications. Knowledge of the refractive index of semiconductors in the energy range below the lowest direct band gap is also of interest in this respect. Extensive studies concerning this subject already exist, some of them resulting in quite accurate calculations [4,6]. However, these models are not very general, as they require the evaluation of some parameters by empirical methods. As a result, physical insight is limited.

The frequency or wavelength dependence of the optical constants in a dielectric may be obtained from a single effective oscillator model (SEO), which considers the solid as an assembly of oscillators, which are set into forced vibration by the radiation. The single effective oscillator model, in terms of the dispersion energy E_d and oscillator energy E_p is given as [4,7]

$$n(E)^2 - 1 = \frac{E_p E_d}{E_p{}^2 - E^2} \qquad \textbf{1.1}$$

The refractive index dispersion data below the interband absorption edge in more than 100 widely different solids and liquids were analyzed using the SEO model [4]. The near gap optical properties of a material are dominated by the absorption edge of the semiconductor. A model that takes this into account is that of M.A. Afromowitz [5]. In this work we show that a single effective oscillator (SEO) model developed by Wemple and DiDomenico [4] as well as the more advanced three-parameter model of Afromowitz [5] could be applied to the ion implanted DSL's.

Applying this theoretical approach to experimental ellipsometry and near infrared reflectance measurements on a series of GaAs DSL's implanted with hydrogen at doses ranging from $10^{12}\ cm^{-2}$ to $10^{16}\ cm^{-2}$, allowed us to determine the dose dependent effective band gap E_g as well as the other model parameters. In this way we could determine the implantation dose required to change the DSL's into something resembling the bulk material.

In the work of M.A. Afromowitz the lowest direct band gap is used. For a superlattice this corresponds to the effective band gap, which is quite difficult to determine experimentally, as it depends on the degree of optical excitation of the material. The electronic excitation spectrum of a semiconductor is generally described in terms of a frequency dependent complex electronic dielectric constant $\varepsilon(\omega) = \varepsilon_1(\omega) + i\varepsilon_2(\omega)$, where $\varepsilon_1(\omega)$ and $\varepsilon_2(\omega)$ are the real and imaginary parts, respectively. It is well known that the real part of the dielectric constant $\varepsilon_1(\omega)$ can be obtained by the Kramers-Kronig (KK) transform of the imaginary part $\varepsilon_2(\omega)$. Hence the desired response information can be obtained, if one is able to determine either the real ($\varepsilon_1(\omega)$) or imaginary ($\varepsilon_2(\omega)$) parts. The KK transform is the basic relation used in relating the SEO model to that of the modified Afromowitz model.

1.2- Refractive Index Measurement Above Band Gap

The demand for rapid, non-destructive analysis of surfaces and thin films, especially films and surfaces occurring in different device technologies, activated an interest in ellipsometric evaluation. Ellipsometry enables optical constants of materials to be determined with high accuracy and is therefore a valuable aid in solving a wide variety of problems in different disciplines.

The fact that ellipsometric measurements can be performed in any ambient is a definite advantage over other surface-science techniques for industrial applications. In ellipsometry, one measures the change in polarization state of a linearly polarized

beam of light after non-normal reflection from the sample to be studied. The polarization state can be defined by two parameters, for example, the relative phase and relative amplitude of the orthogonal electric-field components of a polarized light wave. On reflection both electric field components are modified in a linear way, and therefore a single ellipsometric measurement provides two independent parameters. Such measurements may be interpreted to yield the optical constants of the reflecting material or, when the reflecting material is a film-covered substrate, the thickness and optical constants of the film.

For the measurement of optical constants of substrates, ellipsometry has the advantages over conventional techniques of applicability to strongly absorbing media and simplicity of measurement and sample preparation. Ellipsometry can be applied to surface films throughout the thickness range from partial mono-atomic coverage up to microns [8]. There is no need to use the KK relations to relate the real and the imaginary parts, since it gives both values independently. D.J. Brink et al [9] used a Gartner L119 single-wavelength ellipsometer with a He-Ne (632.8) laser source to investigate radiation-induced changes to GaAs DSL structure by comparing the complex index of reflection of untreated and a α - particle irradiated sample. In our present work, we studied the change in the complex refractive index of GaAs DSL's induced by hydrogen ion implantation. Ellipsometry with three different laser sources were used in this experiment.

1.3- Photoluminescence And Raman Scattering

Ion implantation is a key technology in the preparation of doped semiconductors with controlled impurity profiles for device applications. Manufacturing and designing highly sophisticated semiconductors rely on the ability of characterization and probing of these materials. Optical characterization is one of the best ways, because the sample is unaltered, as the measurement itself does not cause damage. The optical beam, which is generally a laser beam, can easily be manipulated.

Two of the main optical characterization techniques are photoluminescence (PL) and Raman spectroscopy (RS). In PL, light separates the charge carriers within the band or impurity structure of a semiconductor. Their subsequent recombinations then produce characteristic light emission. In RS, the energy of an incoming photon is altered by nonlinear interaction with phonons, carriers, or impurities in the material, to produce a frequency-shifted outgoing photon.

Several experimental investigations have been made with PL and RS measurement techniques. D. J. Brink et al [9] have studied the damaged induced in GaAs DSL's by α - particle irradiation and its recovery after annealing using PL. H. W. Kunert et al [10,11] used PL and Raman techniques to study the effect of α, Ar^{+} and N^{+} ion implantation in GaAs nipi DSL's. PL and RS (Normal and resonant) techniques were used to investigate the hydrogen implantation induced damage in np DSL's in our present work.

CHAPTER 2

Dispersion Theory

2.1. Optical Constants...8

2.2. Kramers-Kronig Relations...10

2.3. Theoretical Models For The Evaluation

Of Refractive Index...10

2.3.1- Sellmeier Equation...11

2.3.2- Single-Oscillator Model...11

2.3.3- Modified Single Oscillator Model...12

2.4. Reflectance R...16

2.4.1- Reflection at a planer interface between

two isotropic media 16

2.4.2- Reflection by an ambient-film-substrate system.....................19

CHAPTER 2

Dispersion Theory

2.1- Optical Constants

It is convenient in the theoretical treatment of dispersion to consider separately the contributions to the dielectric constant due to the bound and the free electron. The free electron gives higher contribution for the dielectric constant in metal whereas the contribution from the bound electron is high for non-conducting materials. In semiconductors, both contributions are important; the bound electrons give rise to the intense absorption on the short-wavelength side of the main absorption edge while at long wavelengths free-carrier absorptions become significant [6].

The optical properties of a medium at all photon energies E= $h\omega/2\pi$ can be describe by the complex dielectric function

$$\varepsilon(\omega) = \varepsilon_1(\omega) + i\varepsilon_2(\omega), \qquad \textbf{2.1}$$

where $\varepsilon_1(\omega)$ and $\varepsilon_2(\omega)$ are the real and imaginary parts of the dielectric constant. The complex refractive index $N = (n(\omega) + ik(\omega))$ where n (ω) is the real refractive index and $k(\omega)$ is the imaginary part called extinction coefficient, also called attenuation index is related to the dielectric constant as:

$$N = [\varepsilon_1(\omega) + i\varepsilon_2(\omega)]^{1/2} \qquad \textbf{2.2}$$

The optical constants $n(\omega)$ and $k(\omega)$ are real and positive and can be determined by optical measurements. From equation 2.1 and 2.2, it follows that

$$\varepsilon_1(\omega) = n^2 - k^2, \tag{2.3a}$$

$$\varepsilon_2(\omega) = 2nk, \tag{2.3b}$$

$$n = \left(\frac{(\varepsilon_1(\omega)^2 + \varepsilon_2(\omega)^2)^{\frac{1}{2}} + \varepsilon_1(\omega)}{2} \right)^{\frac{1}{2}}, \tag{2.4a}$$

$$k = \left(\frac{[\varepsilon_1(\omega)^2 + \varepsilon_2(\omega)^2]^{\frac{1}{2}} - \varepsilon_1(\omega)}{2} \right)^{\frac{1}{2}}. \tag{2.4b}$$

The absorption coefficient α, which is a function of the real and imaginary parts of the dielectric constant, is given by [12]:

$$\alpha = \frac{4\pi k}{\lambda_0}, \tag{2.5}$$

where λ_0 is the wavelength of light in vacuum.

Fresnel's equations give values for the amplitudes of the electromagnetic fields of the reflected and refracted waves at a boundary between two media. The reflectance R, which is a measurable quantity, at normal incidence on a single interface (air-material interface) is given by:

$$R = \frac{(n-1)^2 + k^2}{(n+1)^2 + k^2}. \tag{2.6a}$$

For energies below the band gap or for a transparent region, in which $k = 0$, the real parts of the refractive index can be deduced from equation 2.6a and given as[13]:

$$n = \frac{(1+\sqrt{R})}{(1-\sqrt{R})}. \qquad \textbf{2.6b}$$

2.2- Kramers-Kronig Relations

Given some physical model, for example an oscillator or some absorbing centers in a solid, the dielectric constants $\varepsilon_1(\omega)$ and $\varepsilon_2(\omega)$ can be calculated. A general relationship between these two quantities, which allows one to be calculated if the other is known over a sufficiently wide frequency spectrum, is described by the following equations. These equations, known as the Kramers-Kronig (KK) relations, relate the real and imaginary parts of the dielectric constant. They are [14]

$$\varepsilon_1(\omega) = 1 + \frac{2}{\pi}\int_0^\infty \frac{\omega' \varepsilon_2(\omega')}{\omega'^2 - \omega^2} d\omega', \qquad \textbf{2.7a}$$

$$\varepsilon_2(\omega) = -\frac{2\omega}{\pi}\int_0^\infty \frac{\varepsilon_1(\omega')}{\omega'^2 - \omega^2} d\omega'. \qquad \textbf{2.7b}$$

2.3- Theoretical Models For The Evaluation Of Refractive Index

Knowledge of the refractive index of semiconductors in the energy range near or below the fundamental absorption edge is often of interest in device manufacturing. The magnitude of the refractive index is a function of the wavelength of the incident light. Some of the theoretical models used for calculating the refractive index dispersion in the energy range near or below the fundamental absorption edge are discussed below.

2.3.1- Sellmeier Equation

The refractive index dispersion can be given by the first-order Sellmeier equation [12].

$$N(\lambda)^2 = A + B\frac{\lambda^2}{\lambda^2 - C^2}, \qquad \textbf{2.8}$$

where λ is the light wavelength in vacuum. This equation is based on an empirical relation. The refractive-index dispersion obtained from this expression is, therefore, not through the KK relation and is valid only over a very limited energy range.

2.3.2- Single-Oscillator Model

Wemple and DiDomenico have proposed a semi-empirical single-effective-oscillator model to analyze refractive-index dispersion in more than 100 widely different solids and liquids at energies sufficiently below the direct band edge [4]. Their model requires two parameters, oscillator energy position E_p and dispersion energy E_d, where the imaginary part of the dielectric constant $\varepsilon_2(E)$ of the material is assumed to be a delta function at E_p and the strength of an effective oscillator at energy E_p was defined to be $\frac{\pi E_d}{2}$ [5]. Introducing these quantities into the following equation, based on the KK relation (Appendix A-1),

$$\varepsilon_1(E') = 1 + \frac{2}{\pi}\int_0^\infty \frac{E\varepsilon_2(E)}{E^2 - E'^2}dE, \qquad \textbf{2.9}$$

we obtain

$$n(E)^2 - 1 = \frac{E_p E_d}{E_p^2 - E^2}, \qquad \textbf{2.10a}$$

which can be rewrite as

$$\frac{1}{n(E)^2 - 1} = \frac{E_p}{E_d} - \frac{1}{E_p E_d}E^2. \qquad \textbf{2.10b}$$

Experimental verification of the above equation can be obtained by plotting the inverse of susceptibility $1/\chi = 1/(n^2 - 1)$ versus square of the photon energy (E^2). Some typical results are shown in references [4-6]. The left hand side of equation 2.10a is defined as the susceptibility:

$$\chi(E) = n(E)^2 - 1. \qquad \textbf{2.10c}$$

This model will give reasonable results for photon energies well below the absorption edge in semiconductors. It is noted, however that these energies are not of immediate interest for devices such as the semiconductor hetero-junction laser. A more complex model is therefore needed and this will be discussed in the next section.

2.3.3- Modified Single Oscillator Model

The above single oscillator model starts to fail when one approaches to the absorption edge. To see the invalidity of this model near to the direct band gap, one can start by expanding the Kramers-Kronig relation's equation 2.9. In materials exhibiting a band gap, the dielectric real part $\varepsilon_1(E)$ in the energy region below the direct band gap, in which $\varepsilon_2(E)$ may be taken as zero, is related to the optical absorption above the gap by:

$$\varepsilon_1(E') - 1 = n(E')^2 - 1 = \frac{2}{\pi}\int_{E_g}^{\infty} \frac{E\varepsilon_2(E)}{E^2 - E'^2} dE, \qquad \textbf{2.11}$$

for $E' < E_g \leq E$.

E_g is the direct band gap and we have identified $\varepsilon_1(E)$ with the square of the refractive index n. Expanding equation 2.11 in a power series, the following is obtained (Appendix A part 2):

$$\varepsilon_1(E') - 1 = \chi(E') = \frac{2}{\pi}\int_{Eg}^{\infty} \varepsilon_2(E)\left[\frac{1}{E} + \frac{E'^2}{E^3} + \frac{E'^4}{E^5} + \ldots\right] dE, \qquad \textbf{2.12}$$

where $\chi(E')$ is the susceptibility.

Integrating each term in the above equation separately gives a power series expansion for susceptibility

$$\chi(E') = M_{-1} + M_{-3}E'^{2} + M_{-5}E'^{4} + \ldots, \qquad \textbf{2.13}$$

where the coefficients are the moments of the $\varepsilon_2(E)$ spectrum, which are given by

$$M_i = \frac{2}{\pi}\int_{Eg}^{\infty} \varepsilon_2(E)E^i dE, \qquad \textbf{2.14}$$

with $i = -1, -3, -5, \ldots$.

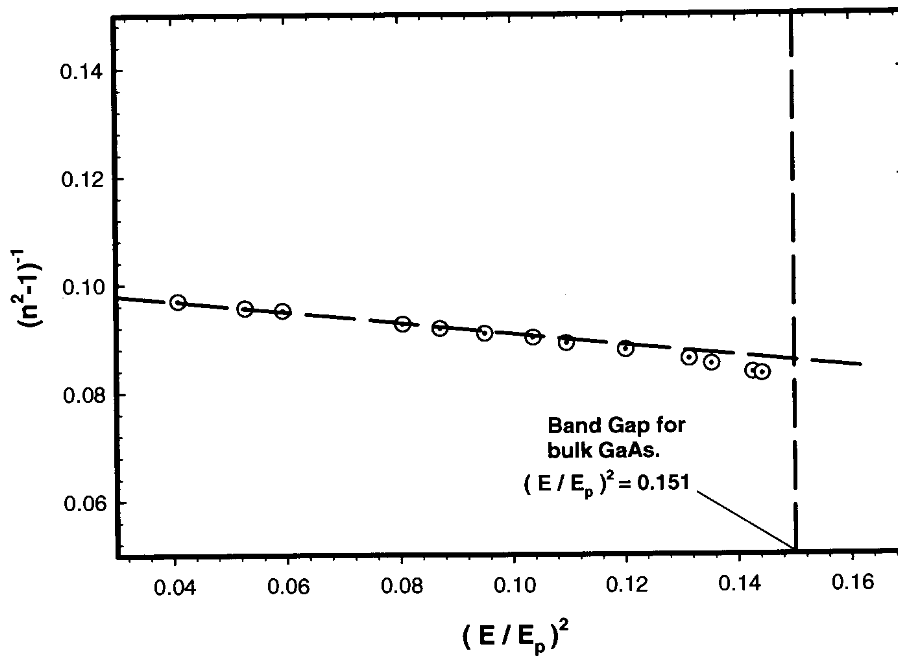

Figure 2.1a. The reciprocal susceptibility of bulk GaAs plotted versus $(E/E_p)^2$, *where* E *is the photon energy and* E_P *is the energy position parameter in the single-effective-oscillator [5]. The dashed line (vertical) represents the room temperature band gap of bulk GaAs.*

The moments of higher order in the above equation weight the low-energy spectrum, and their contribution to the susceptibility become significant only as E approaches E_g. As the single-effective-oscillator model does not represent the low-energy range of the $\varepsilon_2(E)$ spectrum accurately, one should expect a discrepancy between the model and the data as E approaches E_g, as illustrated in figure 2.1a [5].

Afromowitz has suggested an improved model for the variation of the imaginary part of the dielectric constant $\varepsilon_2(\omega)$ with photon energy in semiconductors. This model is constructed using an empirical form, which agrees closely with the data on the low-energy side of the spectrum (figure 2.1b). The model with three parameters is as follows:

$$\varepsilon_2(E) = \begin{cases} \eta E^4, & E_g \le E \le E_f \\ 0, & otherwise \end{cases} . \qquad \textbf{2.15}$$

Direct substitution of this form into the moment equation 2.14 results in

$$M_{-1} = \frac{\eta}{2\pi}\left(E_f{}^4 - E^4{}_g\right), \qquad \textbf{2.16}$$

$$M_{-3} = \frac{\eta}{\pi}\left(E_f{}^2 - E^2{}_g\right). \qquad \textbf{2.17}$$

Expanding equation 2.10a in a power series gives:

$$n(E)^2 - 1 = \frac{E_d}{E_p} + E^2\frac{E_d}{E_p{}^3} + E^4\frac{E_d}{E_p{}^5} + E^6\frac{E_d}{E_p{}^7} + \ldots . \qquad \textbf{2.18}$$

Constraining the susceptibility $\chi(E)$ calculated from the modified model (2.13) to fit the data at low energy to the order of E^2 and equating with equation 2.18 we get

$$\chi(E) = \frac{E_d}{E_p} + E^2\frac{E_d}{E_p{}^3} = M_{-1} + M_{-3}E^2 . \qquad \textbf{2.19}$$

Where the new parameters E_f and η in equation 2.15 can be determined by equating like terms in the above equation as:

$$\frac{\eta}{2\pi}(E_f^4 - E_g^4) = \frac{E_d}{E_p} \quad \text{and} \quad \frac{\eta}{\pi}(E_f^2 - E_g^2) = \frac{E_d}{E_p^3},$$

then we obtain

$$E_f = (2E_p^2 - E_g^2)^{\frac{1}{2}}, \qquad 2.20$$

$$\eta = \frac{\pi E_d}{2E_p^3(E_p^2 - E_g^2)}. \qquad 2.21$$

The actual $\varepsilon_2(E)$ spectrum of GaAs compared with that of the empirical model (dashed curve) and the single-effective-oscillator model is shown in the figure2.1b below [5].

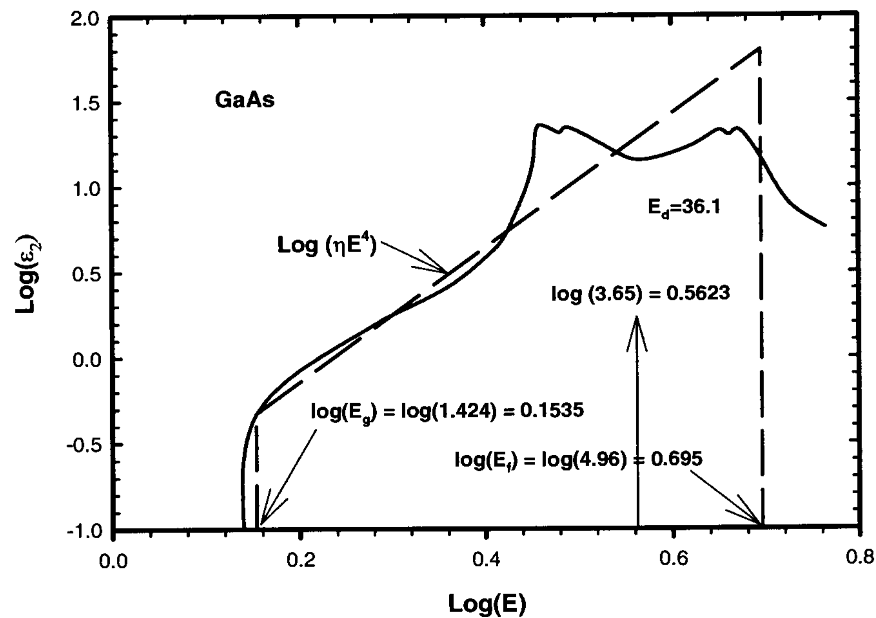

Figur2.1b. Representation of the $\varepsilon_2(E)$ spectrum of GaAs. The solid curve is calculated from data [5,15]. The delta function represents the single-effective-oscillator model. The dashed curve is the empirical model used in this calculation [5].

The dashed line fits reasonably to the actual curve in the low-energy side of the $\varepsilon_2(E)$ spectrum. This is the region, which contribute most heavily to the higher order moments, which are important in predicting the index of refraction for energies approaching E_g. Substituting equation 2.15 into 2.12, we get the final expression for the dielectric susceptibility ($n(E)^2$ -1) (Appendix A part 2):

$$\chi(E) = M_{-1} + M_{-3}E^2 + \frac{\eta}{\pi}E^4 \ln\left\{\frac{E_f^2 - E^2}{E_g^2 - E^2}\right\}, \qquad \textbf{2.22a}$$

which can also be written as:

$$n(E)^2 - 1 = \frac{E_d}{E_p} + \frac{E_d E^2}{E_p^3} + \frac{\eta E^4}{\pi}\ln\{\frac{2E_p^2 - E_g^2 - E^2}{E_g^2 - E^2}\}. \qquad \textbf{2.22b}$$

The parameters E_d, E_P, and E_g appearing in equations 2.21 and equation 2.22 are known for many binary semiconductors and may be calculated for ternary and quaternary compounds by interpolation. Afromowitz gave these parameters values for $Al_xGa_{1-x}As$, $GaAs_{1-x}P_x$, and $In_xGa_{1-x}P$ alloys [5].

2.4- Reflectance R

2.4.1- Reflection at a planer interface between two isotropic media

When a light wave is incident on a surface, it is a common observation that part is reflected and part is transmitted. It is found experimentally that the fraction of the total energy, which is reflected, depends on the index of refraction n of the material.

UNIVERSITEIT VAN PRETORIA
UNIVERSITY OF PRETORIA
YUNIBESITHI YA PRETORIA

Figure 2.2a.

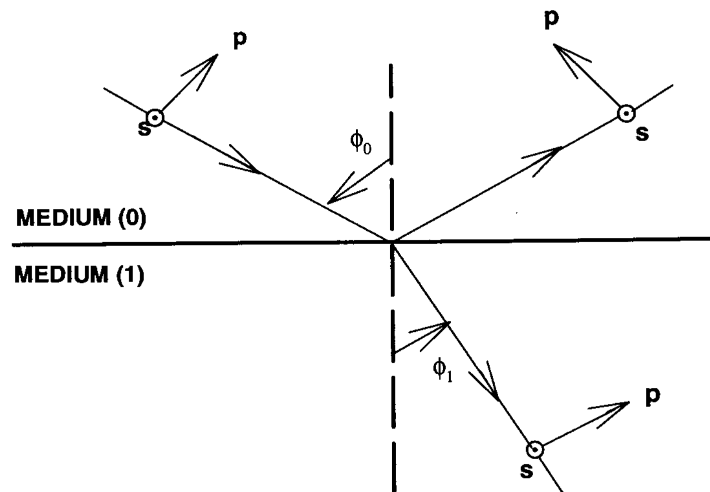

Figure 2.2a shows the oblique reflection and transmission of a plane wave at the planar interface between two semi-infite media 0 and 1.

Consider the reflection of an optical plane wave at a planar interface between two semi-infinite homogeneous optically isotropic media 0 and 1 with complex indices of refraction N_0 and N_1, respectively. The total fields inside media 0 and 1 obey Maxwell's equations and the usual boundary condition (BC) at the interface (figure 2.2a). Snell's law relates the angle of incidence ϕ_0 and refraction ϕ_1 as follows:

$$N_1 Sin\phi_1 = N_0 Sin\phi_0 . \tag{2.24}$$

The amplitude and polarization of the reflected wave can be determined from the continuity of the tangential components of the electric E and magnetic H field vectors across the interface. Let (E_{ip}, E_{is}), (E_{rp}, E_{rp}) and (E_{tp}, E_{ts}) represent the complex amplitude of the components of the electric vectors of the incident, reflected and transmitted waves, respectively.

Matching the tangential E and H fields across the interface leads to [16 pp 272],

$$\frac{E_{rp}}{E_{ip}} = r_p = \frac{N_1 \cos\phi_0 - N_0 \cos\phi_1}{N_1 \cos\phi_0 + N_0 \cos\phi_1}, \qquad \textbf{2.24a}$$

$$\frac{E_{rs}}{E_{is}} = r_s = \frac{N_0 \cos\phi_0 - N_1 \cos\phi_1}{N_0 \cos\phi_0 + N_1 \cos\phi_1}, \qquad \textbf{2.24b}$$

$$\frac{E_{tp}}{E_{ip}} = t_p = \frac{2 N_0 \cos\phi_0}{N_0 \cos\phi_1 + N_1 \cos\phi_0}, \qquad \textbf{2.24c}$$

$$\frac{E_{ts}}{E_{ip}} = t_s = \frac{2 N_0 \cos\phi_0}{N_1 \cos\phi_1 + N_0 \cos\phi_0}, \qquad \textbf{2.24d}$$

which are Fresnel's complex-amplitude reflection (r) and transmission (t) coefficients for the p and s polarizations. We can write the complex Fresnel's coefficients as

$$r_p = |r_p| e^{j\delta_{rp}}, \qquad \textbf{2.25a}$$

$$r_s = |r_s| e^{j\delta_{rs}}, \qquad \textbf{2.25b}$$

$$t_p = |t_p| e^{j\delta_{tp}}, \qquad \textbf{2.25c}$$

$$t_s = |t_s| e^{j\delta_{ts}}. \qquad \textbf{2.25d}$$

Where $|t_p|$ and $|r_p|$ give the ratios of the amplitudes of the electric vectors of the transmitted and reflected waves respectively to that of the incident wave for p polarization and similarly for $|t_s|$ and $|r_s|$ for s polarization. δ_{rp} and δ_{tp} are the phase shifts upon reflection and refraction of the p polarization of light respectively, and similarly for δ_{rs} and δ_{ts}. In addition to polarization, the reflectance R is a measurable quantity and is given by

$$R_p = |r_p|^2, \qquad \textbf{2.26a}$$

for p polarization and

$$R_s = |r_s|^2, \qquad \textbf{2.26b}$$

for s polarization.

For normally incident light from the first medium (air n = 1) to the second medium equation 2.26 will be given by equation 2.6a.

2.4.2- Reflection by an ambient-film-substrate system

As shown in figure 2.2b, we assume that the film has plane parallel boundaries of separation (film thickness) d_1 and is sandwiched between semi-infinite ambient (immersion) and substrate media.

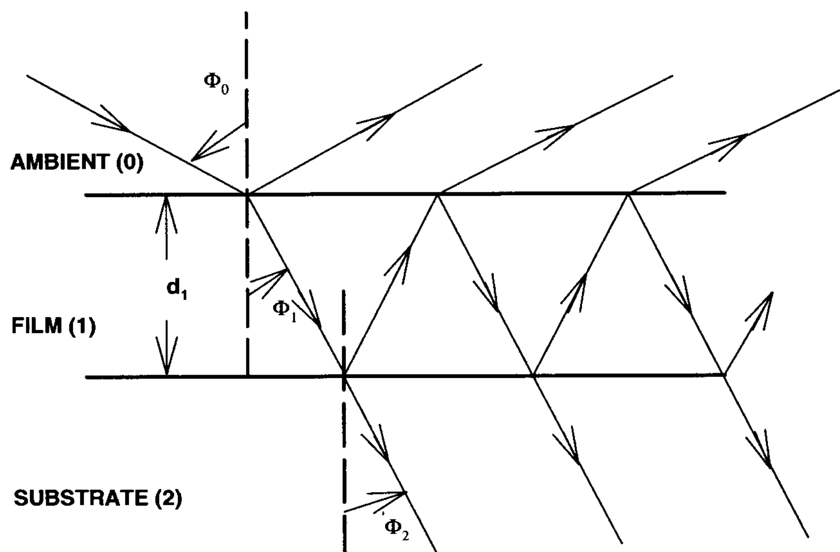

Figure 2.2b shows the oblique reflection and transmission of a plane wave by ambient (0)-film (1)-substrate (2) system with plane parallel boundaries.

The ambient, the film and the substrate are all homogeneous and optically isotropic, with complex indices of refraction N_0, N_1 and N_2, respectively. We assume that

when the incident wave first meets the 0-1interface, part of it is reflected in medium 0 and part is refracted in to the film, according to the interface Fresnel's transmission and reflection coefficients. The refracted wave inside the film subsequently suffers multiple internal reflections at the 1-0 and 1-2 film-bounding interfaces, which are, in general, not perfectly reflecting. Thus each time the multiply reflected wave in the film strikes the 1-0 or 1-2 interface, a component wave is leaked (refracted) into the semi-infinite ambient or substrate medium, respectively.

If the Fresnel reflection and transmission coefficients at 0-1(1-0) and 1-2 interfaces are denoted by $r_{01}, t_{01} (r_{10}, t_{10})$ and r_{12}, t_{12} respectively, the complex amplitudes of the successive partial plane waves that make up the resultant reflected wave in medium 0 are given by $r_{01}, t_{01}t_{10}r_{12}e^{-j2\beta}, t_{01}t_{10}r_{10}r_{12}^{2}e^{-j4\beta}, t_{01}t_{10}r_{10}^{2}r_{12}^{3}e^{-j6\beta}, \ldots$, where β is the phase change that the multiply-reflected wave inside the film experiences as it traverses the film once from one boundary to the other. In terms of the free space wavelength λ_0, the film thickness d_1, the film complex index of refraction N_1 and the (complex) angle of refraction in the film ϕ_1, the phase angle (film phase thickness) is given by [16]

$$\beta = 2\pi(\frac{d_1}{\lambda_0})N_1 \cos\phi_1, \qquad \textbf{2.27a}$$

or applying Snell's law

$$\beta = 2\pi(\frac{d_1}{\lambda_0})(N_1^2 - N_0^2 \sin^2\phi_0)^{\frac{1}{2}}, \qquad \textbf{2.27b}$$

where ϕ_0 is the angle of incidence in medium 0.

Addition of the partial wave leads to an infinite geometric series for the total reflected amplitude R (*total complex- amplitude reflection).*

$$\mathrm{R} = r_{01} + t_{01}t_{10}r_{12}e^{-j2\beta} + t_{01}t_{10}r_{10}r_{12}^{2}e^{-j4\beta} + t_{01}t_{10}r_{10}^{2}r_{12}^{3}e^{-j6\beta} + \ldots \qquad \textbf{2.28}$$

Substituting $r_{01} = -r_{10}$ and $t_{01}t_{10} = 1 - r_{01}^2$ (as can be proved from equations 2.24) we get:

$$\mathrm{R} = \frac{r_{01} + r_{12}e^{-j2\beta}}{1 + r_{01}r_{12}e^{-j2\beta}}. \qquad \textbf{2.29}$$

This equation is valid when the incident wave is linearly polarized either parallel (p) or perpendicular (s) to the plane of incidence. Thus, we may restore the information on polarization by adding the p and s subscripts. The interface Fresnel's complex reflection coefficient can be evaluated from equation 2.24. The product of equation 2.29 with its complex conjugate ($R = \mathrm{R}^* \cdot \mathrm{R}$) will give the corresponding value for the reflectance R of the material. And for a normal angle of incidence it is given by:

$$R = \mathrm{R}^* \cdot \mathrm{R} = \left\{\frac{CD + AB\sin^2 2\beta}{D^2 + F^2 \sin^2 2\beta}\right\}^2 + \left\{\frac{(BC - AD)\sin^2 2\beta}{D^2 + B^2 \sin^2 2\beta}\right\}^2 \qquad \textbf{2.30}$$

Where

$$A = (N_2 - N_1)(N_1 + N_2)$$

$$B = (N_1 - N_0)(N_2 - N_1)$$

$$C = (N_1 - N_0)(N_1 + N_2) + (N_2 - N_1)(N_1 + N_0)\cos 2\beta$$

$$D = (N_1 + N_0)(N_1 + N_2) + (N_2 - N_0)(N_1 - N_0)\cos 2\beta$$

$$\beta = 2\pi \frac{d_1 N_1}{\lambda_0}$$

This method of addition of multiple reflections becomes impractical when considering the reflection and transmission of polarized light at oblique incidence by a multilayer film between semi-infinite ambient and substrate media. Hence a two by two matrix method is usually used to derive the reflectivity of a multi-layer [16 pp 332-340].

117394855

b16376614

CHAPTER 3

Ellipsometry And Polarized Light

3.1. Uniform Transverse-Electric (TE) Plane Waves Of Light..23

3.1.1- The Jones Vector of a Uniform TE Plane Wave........................23

3.1.2- The Wave Intensity...26

3.1.3- State of Polarization..26

3.2. Propagation of Polarized Light Through Polarizing Optical Systems...27

3.2.1- Transmission Type device...27

3.2.2- Reflection Type Device..30

3.3. Operating Principle Of The Ellipsometer.................................32

3.3.1- Ellipsometry Transmission 32

3.4. Null Ellipsometry...35

CHAPTER 3

Ellipsometry And Polarized Light

3.1- Uniform Transverse-Electric (TE) Plane Waves Of Light

The electric vector of a linearly polarized uniform transverse-electric (TE) wave varies with position r and time t according to

$$\vec{E}(r,t) = [\tilde{E}\,cos(\omega t - \vec{\kappa}.\vec{r} + \delta)]\hat{u}, \qquad 3.1$$

$$\hat{u}\cdot\hat{u} = 1, \quad \vec{\kappa}\cdot\hat{u} = 0.$$

Where ω is the angular frequency, $\vec{\kappa}$ is the propagation vector and δ is a phase constant, which depends on the choice of origin. The polarization of this wave can be generalized from linear to elliptic by superposition of two linearly polarized waves with different polarization and phase. Equation 3.1 then becomes

$$\vec{E}(\vec{r},t) = [\tilde{E}\,cos(\omega t - \vec{\kappa}\cdot\vec{r} + \delta_1)]\hat{u} + [\tilde{E}'\,cos(\omega t - \vec{\kappa}\cdot\vec{r} + \delta_2)]\hat{u}', \qquad 3.2$$

$$\hat{u}\cdot\hat{u} = \hat{u}'\cdot\hat{u}' = 1, \ \vec{\kappa}\cdot\hat{u} = \hat{u}\cdot\hat{u}' = \vec{\kappa}\cdot\hat{u}' = 0.$$

3.1.1- The Jones Vector Of A Uniform TE Plane Wave

If it is assumed that the wave propagates along the positive direction of the z-axis of a xyz Cartesian coordinate system and if, in addition, the unit vectors $\hat{u}$ and $\hat{u}'$ are chosen parallel to the positive directions of the x- and y-axes respectively equation 3.2 becomes

$$\vec{E}(z,t) = [\tilde{E}_x\,cos(\omega t - \frac{2\pi}{\lambda}z + \delta_x)]\hat{x} + [\tilde{E}_y\,cos(\omega t - \frac{2\pi}{\lambda}z + \delta_y)]\hat{y}. \qquad 3.3$$

Because the wave is uniform, the electric field is the same at all points in a plane wave front, at a fixed z position and because it is traverse-electric (TE), there is no field component along the direction of propagation $\vec{\kappa} = (\frac{2\pi}{\lambda})\hat{z}$.

Equation 3.3 can be written in a more concise form by:

1- Writing 3.3 in a 2x2 matrix form as:

$$E(z,t) = \begin{bmatrix} \tilde{E}_x cos(\omega t - \frac{2\pi}{\lambda} z + \delta_x) \\ \tilde{E}_y cos(\omega t - \frac{2\pi}{\lambda} z + \delta_y) \end{bmatrix}. \qquad \textbf{3.4}$$

2- Separating the time and space components as:

$$E(z) cos(\omega t) = e^{-j2\pi z n/\lambda_0} \begin{bmatrix} \tilde{E}_x e^{j\delta_x} \\ \tilde{E}_y e^{j\delta_y} \end{bmatrix} cos(\omega t). \qquad \textbf{3.5}$$

Where n is the index of refractive and λ_0 is the vacuum wavelength.

3- Dropping the spatial information about the wave by considering the field over one fixed transverse plane Z = 0 of the xyz coordinate system.

$$E(0) = \begin{bmatrix} \tilde{E}_x e^{j\delta_x} \\ \tilde{E}_y e^{j\delta_y} \end{bmatrix}. \qquad \textbf{3.6}$$

The vector E (0) is called the *Jones vector* of the wave. The Jones vector contains complete information about the amplitudes and phases of the field components and hence about the polarization of the wave.

Equation 3.6 can be written in a more general form as

$$E = \begin{bmatrix} E_x \\ E_y \end{bmatrix}, \qquad 3.7$$

where $E_x = |E_x| e^{j\delta_x}$, $E_y = |E_y| e^{j\delta_y}$,

and the dependence on z can be explicitly included as

$$E(z) = e^{-j2\pi z n / \lambda_0} E(0). \qquad 3.8a$$

Writing this equation in a matrix form

$$\begin{bmatrix} E_{x'} \\ E_{y'} \end{bmatrix} = \begin{bmatrix} e^{-j2nz\pi / \lambda_0} & 0 \\ 0 & e^{-j2nz\pi / \lambda_0} \end{bmatrix} \begin{bmatrix} E_x \\ E_y \end{bmatrix}. \qquad 3.8b$$

Which is the transformation of a Jones vector under a coordinate translation parallel to the direction of propagation (the primes referring to the new coordinate).
The Jones vector after a counter clockwise coordinate rotation through an angle α about the z-axis is given by

$$E_{x',y'} = R(\alpha) E_{x,y}, \qquad 3.9$$

where the rotation matrix $R(\alpha)$ is given by

$$R(\alpha) = \begin{bmatrix} \cos\alpha & \sin\alpha \\ -\sin\alpha & \cos\alpha \end{bmatrix}. \qquad 3.10$$

3.1.2- The Wave Intensity

The wave intensity I is simply expressed as the sum of the squared amplitudes of the component oscillations along two mutually orthogonal directions.

$$I = |E_x|^2 + |E_y|^2 = E_x^\bullet \cdot E_x + E_y^\bullet \cdot E_y, \qquad 3.11$$

and in a more compact form

$$I = E^+ \cdot E, \qquad 3.12$$

where E^+ is the Hermitian adjoint of E, defined as the complex conjugate of the transpose of the matrix.

3.1.3- State Of Polarization

Information about the ellipse of polarization can be extracted from the two-component cartesian Jones vector of equation 3.7, if we take the ratio

$$\chi = \frac{E_y}{E_x} = \frac{|E_y|}{|E_x|} e^{j(\delta_y - \delta_x)}, \qquad 3.13$$

where

$$\gamma = \frac{|E_y|}{|E_x|}, \ \arg(\chi) = \delta_y - \delta_x .$$

For $(\delta_y - \delta_x) = 0, \pi$ the polarization is linear and for $(\delta_y - \delta_x) \neq 0, \pi$ the polarization becomes elliptic. Circular polarization is a special case of elliptical polarization; that is for $(\delta_y - \delta_x) = \pm \frac{1}{2}\pi$ and $|E_y| = |E_x|$.

3.2- Propagation Of Polarized Light Through Polarizing Optical Systems

3.2.1- Transmission Type Device

Polarizer and quarter wave plate:

For a light wave propagating through an isotropic medium, the outgoing (E_o) and the incoming (E_i) Jones vectors are related by a transformation matrix called the *Jones matrix* T and it is written as follows

$$\begin{bmatrix} E_{ox} \\ E_{oy} \end{bmatrix} = T \begin{bmatrix} E_{ix} \\ E_{iy} \end{bmatrix} = \begin{bmatrix} e^{-j2nd\pi/\lambda_0} & 0 \\ 0 & e^{-j2nd\pi/\lambda_0} \end{bmatrix} \begin{bmatrix} E_{ix} \\ E_{iy} \end{bmatrix}. \qquad \mathbf{3.14}$$

Where n is the refractive index of the isotropic medium of thickness d and λ_0 is the wavelength of the light in vacuum. For an absorbing medium n is substituted by $n-ik$ (k is the extinction coefficient). The wave propagating through the medium will be retarded by $2nd\pi/\lambda_0$, and the medium is called an *isotropic retarder* (or phase-plate).

Suppose light is travelling in a direction perpendicular to the optical axis of a medium, which is uniaxially linearly birefringent and transparent. If the wave is linearly polarized parallel to the optical axis, the wave will experience a specific refractive index n_e and will travel at speed c / n_e, if the wave is orthogonal to the optical axis, the wave will experience a different refractive index n_o and will travel at a speed c / n_o. Where n_o and n_e are called the ordinary and extraordinary refractive indices of the medium respectively.

For waves having components parallel (x) and perpendicular (y) to the optical axis, the effect of the propagation through a distance d is described by

$$\begin{bmatrix} E_{ox} \\ E_{oy} \end{bmatrix} = T \begin{bmatrix} E_{ix} \\ E_{iy} \end{bmatrix} = \begin{bmatrix} e^{-j2n_e d\pi/\lambda_0} & 0 \\ 0 & e^{-j2n_o d\pi/\lambda_0} \end{bmatrix} \begin{bmatrix} E_{ix} \\ E_{iy} \end{bmatrix}. \qquad \mathbf{3.15a}$$

Here the medium is acting as a *linear retarder (like a quarter wave plate)*.
One can rewrite the transmission matrix T as

$$T = e^{-j\delta_1} \begin{bmatrix} 1 & 0 \\ 0 & e^{-j\delta} \end{bmatrix}, \qquad \mathbf{3.15b}$$

where $\delta_1 = 2\pi n_e d / \lambda_0$ and $\delta = \frac{2\pi d}{\lambda_0}(n_0 - n_e)$.

The quantity $(n_o - n_e)$ is called the *birefringence of the medium.* For negative birefringence the x (optical axis) and y-axes are called the *fast* and *slow* axes respectively.

For a medium, which is both isotropically- refracting and isotropically- absorbing at the same time, a plane wave is retarded and attenuated, after travelling a distance d. This medium acts as an *isotropic retarder and absorber.* This can be described by a Jones matrix by direct substitution of the complex index of refraction ($n - ik$) in place of the real index of refraction n in equation 3.14 and is given by

$$T = \begin{bmatrix} e^{-j2(n-k)d\pi/\lambda_0} & 0 \\ 0 & e^{-j2(n-k)d\pi/\lambda_0} \end{bmatrix}, \qquad \mathbf{3.16}$$

k is the called the extinction coefficient (attenuation) of the medium.

The amplitude of oscillation of the electric field (linear, circular or elliptic) decay with distance according to

$$A(d) = A(0)e^{-\frac{1}{2}\alpha d}, \qquad 3.17$$

while the intensity of the wave $I = A^2$ fall off as

$$I(d) = A^2(0)e^{-\alpha d} \quad , \qquad 3.18$$

where $A(0)$ is the initial amplitude and

$$\alpha = \frac{4\pi k}{\lambda_0}, \qquad 3.19$$

is the absorption coefficient. Since the absorption and refraction properties of the medium are both isotropic, the ellipse of polarization remains unchanged.

If the medium is uniaxially linearly dichroic, a linearly polarized wave will be attenuated by different amounts depending upon the direction of the vibration with respect to the optical axis. Let k_e and k_0 be the extraordinary and ordinary extinction coefficients for light linearly polarized parallel and perpendicular to the optical axis respectively. The Jones matrix can then be obtained by generalizing equation 3.16 as follows

$$T = e^{-j2nd\pi/\lambda_0}\begin{bmatrix} e^{-j2k_e d\pi/\lambda_0} & 0 \\ 0 & e^{-j2k_0 d\pi/\lambda_0} \end{bmatrix}. \qquad 3.20$$

Which can be rewritten as

$$T = e^{-j2nd\pi/\lambda_0}\begin{bmatrix} e^{-\frac{1}{2}\alpha_1 d} & 0 \\ 0 & e^{-\frac{1}{2}\alpha_2 d} \end{bmatrix} = e^{-j2nd\pi/\lambda_0} e^{-\frac{1}{2}\alpha_1 d}\begin{bmatrix} 1 & 0 \\ 0 & e^{-\frac{1}{2}\alpha d} \end{bmatrix}, \qquad 3.21$$

where $\alpha_1 = \frac{4\pi k_e}{\lambda_0}$, $\alpha_2 = \frac{4\pi k_0}{\lambda_0}$ and $\alpha = \frac{4\pi}{\lambda_0}(k_0 - k_e)$,

represent the extraordinary, ordinary and relative absorption coefficients, respectively. The quantity $(k_0 - k_e)$ is called *dichroism*. The medium acts as a *linear partial polarizer*. A special case of the linearly dichroic device is an *ideal linear polarizer*. In this case $k_e = 0$, $k_0 = \infty$ and the Jones matrix assumes the simple form.

$$T = e^{-j2nd\pi/\lambda_0}\begin{bmatrix} 1 & 0 \\ 0 & 0 \end{bmatrix} \qquad 3.22$$

3.2.2- Reflection-Type-Device

A reflected electric field E_r from a sample (S) can be given as a product of the Jones reflection matrix $\Re$ and the incident electric field E_I as $E_r = \Re E_I$, where the reflection Jones matrix is given by:

$$\Re = \begin{bmatrix} r_p & 0 \\ 0 & r_s \end{bmatrix} = \begin{bmatrix} |r_p|e^{-j\delta_P} & 0 \\ 0 & |r_s|e^{-j\delta_S} \end{bmatrix}. \qquad 3.23$$

Figure 3.1 shows a typical ellipsometer arrangement. A well collimated beam of monochromatic circularly or unpolarized (natural) light from the source L is passed through the linear polarizer P and a linear retarder or compensator C. Light incident to the sample S is polarized and the state of polarization is controlled by the azimuth positions of the polarizer and compensator around the beam axis. The linear analyser A followed by a photodetector D analyzes the modified state of polarization of the light beam reflected from the sample. The orientation of the polarizer, compensator and analyzer around the beam axis are specified by the azimuth angles P, C and A, respectively.

P and A define the orientation of the polarizer and analyser transmission axes t, while the azimuth C defines the orientation of the compensator's fast axis f. All azimuth angles are measured from the optical axis x. In order to follow the state of polarization of the beam passing through the ellipsometer, we describe the beam by its Jones vector and the optical elements by their Jones matrices. A principal frame is a coordinate system in which the (Cartesian) Jones matrix of an optical component is diagonal (it is assumed that the same system is used at both input and output sides of the optical system). Switching between two coordinate system changes the Jones vector in a manner determined by the rotation $R(\alpha)$ (or $R(-\alpha)$) matrix (equation 3.10).

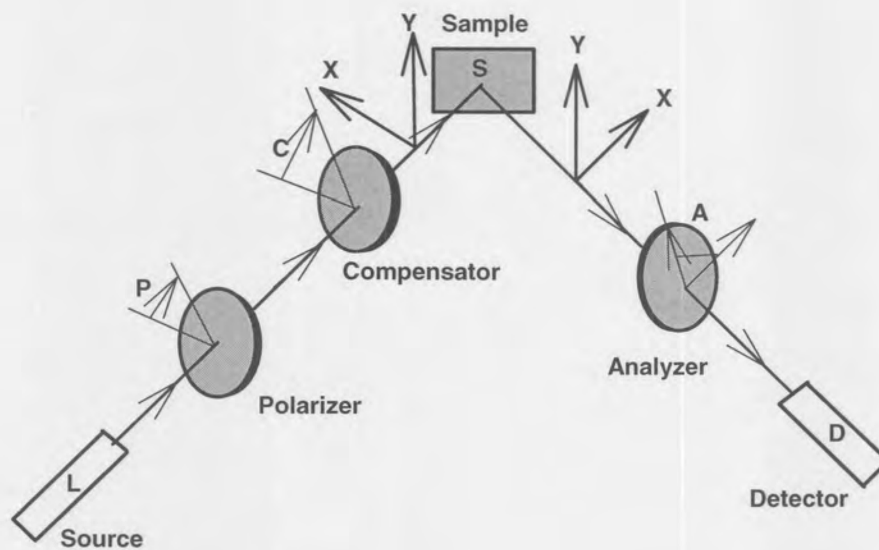

Figure 3.1 The PCSA ellipsometer arrangement with a polarizing section that consists of a linear polarizer P and a compensator C, an analyzing section that consist of a linear analyser A and an optical system S (sample).

3.3- Operating Principle Of The Ellipsometry

3.3.1- Ellipsometer Transmission

The polarizer and the analyser have transmit (t) and extinguish (e) axes with the transmit axis at angles P and A to the x-axis respectively (figure 3.1). The compensator (quarter wave plate in this case) has fast (f) and slow (s) axes with the fast axis at an angle C to the x-axes. For unpolarized or circularly polarized light incident on the polarizer the output becomes linearly polarized, and is given by

$$E_{PO}^{te} = A_P \begin{bmatrix} 1 \\ 0 \end{bmatrix}, \qquad 3.24$$

where the superscript denotes the coordinate system while the first subscript denotes the ellipsometer component and the second either its input (I) or output (O). A_p is a complex constant. The coordinate system t-e has to be rotated through the angle $\alpha =$ -(P-C) to change to the new fast (f) slow (s) system at the input side of the compensator.

$$E_{CI}^{fs} = R(-(P-C))\, E_{PO}^{te},$$

$$= A_p \begin{bmatrix} cos(P-C) & -sin(P-C) \\ sin(P-C) & cos(P-C) \end{bmatrix} \begin{bmatrix} 1 \\ 0 \end{bmatrix},$$

$$= A_P \begin{bmatrix} cos(P-C) \\ sin(P-C) \end{bmatrix}. \qquad 3.25$$

The Jones matrix for the compensator in the f-s system is given by

$$T_C^{fs} = A_C \begin{bmatrix} 1 & 0 \\ 0 & e^{-j\delta_C} \end{bmatrix},$$

hence the electric vector at the output side of the compensator

$$E_{CO}^{fs} = T_C^{fs} E_{CI}^{fs} = A_C A_P \begin{bmatrix} 1 & 0 \\ 0 & e^{-j\delta_C} \end{bmatrix} \begin{bmatrix} cos(P-C) \\ sin(P-C) \end{bmatrix} = A_C A_P \begin{bmatrix} cos(P-C) \\ e^{-j\delta_C} sin(P-C) \end{bmatrix}. \qquad \textbf{3.26}$$

To examine the effect of the sample (S) upon reflection the coordinate system has to be changed from f-s to x-y or p-s. Rotating f-s through an angle of -C does this.

$$E_{SI}^{ps} = R(-C)\, E_{CO}^{fs},$$

$$= A_C A_P \begin{bmatrix} cos(C) & -sin(C) \\ sin(C) & cos(C) \end{bmatrix} \begin{bmatrix} cos(P-C) \\ e^{-j\delta_C} sin(P-C) \end{bmatrix},$$

$$= A_C A_P \begin{bmatrix} cos\,C\, cos(P-C) - e^{-j\delta_C} sin\,C\, sin(P-C) \\ sin\,C\, cos(P-C) + e^{-j\delta_C} cos\,C\, sin(P-C) \end{bmatrix}. \qquad \textbf{3.27}$$

The electric field vector after reflection from the sample is

$$E_{SO}^{ps} = E_{SO}^{xy} = T_S^{ps} E_{SI}^{ps} = \begin{bmatrix} r_p & 0 \\ 0 & r_s \end{bmatrix} E_{SI}^{ps},$$

where r_p and r_s are the complex amplitude reflection coefficients for p and s polarized light. Therefore

$$E_{SO}^{ps} = A_C A_P \begin{bmatrix} r_p [cos\,C\, cos(P-C) - e^{-j\delta_C} sin\,C\, sin(P-C)] \\ r_s [sin\,C\, cos(P-C) + e^{-j\delta_C} cos\,C\, sin(P-C) \end{bmatrix}. \qquad \textbf{3.28}$$

Rotate the p-s system through an angle A to change to the t-e system at the analyser

$$E^{te}_{AI} = R(A)\, E^{ps}_{SO}$$

$$= A_C A_P \begin{bmatrix} \cos A & \sin A \\ -\sin A & \cos A \end{bmatrix} \begin{bmatrix} r_p[\cos C\cos(P-C) - e^{-j\delta_c}\sin C\sin(P-C)] \\ r_s[\sin C\cos(P-C) + e^{-j\delta_c}\cos C\sin(P-C)] \end{bmatrix}, \qquad \textbf{3.29}$$

$$= A_C A_P \begin{bmatrix} r_p\cos A[\cos C\cos(P-C) - e^{-j\delta_c}\sin C\sin(P-C)] + r_s\sin A[\sin C\cos(P-C) + e^{-j\delta_c}\cos C\sin(P-C)] \\ -r_p\sin A[\cos C\cos(P-C) - e^{-j\delta_c}\sin C\sin(P-C)] + r_s\cos A[\sin C\cos(P-C) + e^{-j\delta_c}\cos C\sin(P-C)] \end{bmatrix}$$

Finally at the analyser output,

$$E^{te}_{AO} = T^{te}_{A} E^{te}_{AI} = A_A \begin{bmatrix} 1 & 0 \\ 0 & 0 \end{bmatrix} E^{te}_{AI},$$

$$= A_A A_C A_P \begin{bmatrix} r_p\cos A[\cos C\cos(P-C) - e^{-j\delta_c}\sin C\sin(P-C)] + r_s\sin A[\sin C\cos(P-C) + e^{-j\delta_c}\cos C\sin(P-C)] \\ 0 \end{bmatrix}$$

$$= A_T \begin{bmatrix} L \\ 0 \end{bmatrix}, \qquad \textbf{3.30}$$

Where $A_T = A_A A_C A_P$ and

$L = r_p\cos A[\cos C\cos(P-C) - e^{-j\delta_c}\sin C\sin(P-C)] + r_s\sin A[\sin C\cos(P-C) + e^{-j\delta_c}\cos C\sin(P-C)]$

The intensity (I) of the light emerging from the analyser is given by

$$I = E^{+}E$$

where E^{+} is the Hermitian adjoint of E

$$\therefore \qquad I = E^{te+}_{AO} E^{te}_{AO} = |A_T|^2 |L|^2 = G|L|^2, \qquad \textbf{3.31}$$

where $G = |A_T|^2 = |A_A|^2 |A_C|^2 |A_P|^2$ and $|L|^2 = L^{*} \cdot L$.

Hence the detected signal intensity can be written as a function of ellipsometer parameters: $I = f(P, C, A, e^{-j\delta_c}, r_{p,} r_s)$ and the parameters are

- The azimuth angle setting P, C and A
- The slow and fast relative complex amplitude transmission of the compensator
- The s and p Fresnel's complex reflection coefficients of the optical system.

For fixed angles $\delta_C = \frac{\pi}{2}$ and $C = \frac{\pi}{4}$ equation 3.31 is a periodic function of the polarizer and the analyser azimuth angles with a period of π. Thus if a null is obtained at (P, A), an infinite number of trivially related nulls are obtained at $(P \pm m\pi, A \pm n\pi)$, where m and n are integers.

3.4- Null Ellipsometry

Null ellipsometry is based on finding a set of azimuth angles for the polarizer, compensator and analyser (P, C, A) such that the light flux emerging from the analyser is extinguished. Besides the three azimuth angles, the relative retardation δ_C of the compensator is a fourth parameter that can be adjusted in a search for the null condition, if a variable-retardation compensator is used. Ideally the null condition corresponds to a zero detected signal ($I = 0$), which implies that $L = 0$. Fixing the value of the relative retardation (δ_C) at an angle equal to $\pi / 2$ and applying the null condition to equation 3.30 we obtain

$$\rho = \frac{r_p}{r_s} = -tan\,A\left\{\frac{tan\,C + e^{-j\delta_c}\,tan(P-C))}{1 - e^{-j\delta_c}\,tan\,C\,tan(P-C)}\right\}, \quad 3.32$$

Where ρ is the ratio of Fresnel reflection coefficients r_p and r_s for p and s polarization respectively for one set of nulling angles (P, C, A). The ratio ρ can therefore be measured with ellipsometry.

For fixed values of $\delta_C = \frac{\pi}{2}$ and $C = \frac{\pi}{4}$, equation 3.31 will reduce to

$$\rho = -\tan A \exp[-j2(P - \frac{1}{4}\pi)]. \tag{3.33}$$

If (P, A) represent one set of nulling angles, an associated pair $(P', A') = (P + \frac{1}{2}\pi, \pi - A)$ represents another distinct set of angles. One can rewrite ρ in terms of its magnitude $|\rho|$ and its phase Δ as

$$\rho = \frac{|r_p| e^{j\delta_p}}{|r_s| e^{j\delta_s}} = |\rho| e^{j\Delta}, \tag{3.34}$$

Where

$$\left. \begin{aligned} |\rho| &= \tan A \equiv \tan\psi \\ \Delta &\equiv -2P \pm \frac{1}{2}\pi = \delta_P - \delta_S \end{aligned} \right\} \tag{3.35}$$

Then $\rho = \tan\psi e^{i\Delta} = \frac{r_p}{r_s}$. **3.36**

The angles $\psi (0^0 \leq \psi \leq 90^0)$ and $\Delta (0^0 \leq \Delta \leq 360^0)$ are called *ellipsometric angles* of the reflector (sample). ψ is the angle whose tangent gives the ratio of the amplitude attenuation (or magnification) while Δ gives the difference between the phase shifts experienced upon reflection by the p and s polarizations, respectively.

UNIVERSITEIT VAN PRETORIA
UNIVERSITY OF PRETORIA
YUNIBESITHI YA PRETORIA

CHAPTER 4

Theoretical Considerations On Doping Superlattices

4.1- Structure Of A Doping Superlattice.....................................38

4.2- Electronic Structures...39

4.2.1- Self Consistent Calculation...39

4.2.2- Effective Width Approximation.....................................44

4.2.3- The Pumping Factor – **r**..48

CHAPTER 4

Theoretical Considerations On Doping Superlattices

4.1- Structure Of A Doping Superlattice

Semiconductor doping superlattices (DSL's) are composed of a sequence of ultra-thin crystalline layers of alternating doping of n- and p- type, in some cases separated by undoped (i) intrinsic layers (n-i-p-i crystal). In a compositional superlattice, the two different semiconductors with different band gaps should have a nearly equal lattice constant to minimize lattice mismatch. But a doping superlattice consists of a homogeneous material modulated only by a periodic n- and p- doping. The amounts of impurities used for the doping are relatively small and hence induce only a minor distortion of the crystal lattice of the host material.

A superlattice has some striking features: (1) In a doping superlattice the conduction and the valence bands are modulated by a periodic space charge potential created by the dopants. As a result the conduction band minima are shifted by half a superlattice period with respect to the electron state near the top of the valence band (indirect band in real space). (2) A large deviation of electron and hole concentrations from the equilibrium values even at very low excitation intensities. This is due to the enhancement of the electron and hole recombination lifetime relative to that of the bulk. (3) This deviation of carrier concentration varies the space charge, which result in a substantial change of the effective energy gap. The effective gap of the DSL is thus no longer a fixed parameter of the system, but a quantity, which may be tuned by changing the non- equilibrium electron and hole concentrations. Such doping superlattice structures can be grown by the organo- metallic vapour phase epitaxy (OMVPE) process.

4.2- Electronic Structures

4.2.1- Self Consistent Calculation

The periodic potential in a doping superlattice is exclusively space charge induced. This is in contrast to the compositional superlattices, where the different band gap of the components induces periodic variations of the band edges. A particular advantage of doping superlattices with respect to the theoretical treatment of the electronic structure is that we are dealing with a homogeneous semiconductor, which is only modulated by the superposition of a periodic superlattice potential. For a doping superlattice with no other impurities present than shallow donors and acceptors, one can express the space-charge distribution of the individual doping atoms by a homogeneous distribution function $en_D(z)$ for donors and $-en_A(z)$ for acceptors varying periodically in superlattice direction z; where n_D and n_A represent the donor and acceptor concentration respectively. Then the charge distribution of these impurities is given as [2]

$$\rho_O(z) = e[n_D(z) - n_A(z)]. \qquad \textbf{4.1}$$

The contribution of these bare ionized impurities to the superlattice potential $v_O(z)$ is then given by the solution of the Poisson equation (in SI units):

$$\frac{\partial^2 v_O(z)}{\partial z^2} = \frac{e}{\varepsilon_R \varepsilon_o} \rho_O(z) = \frac{e^2}{\varepsilon_R \varepsilon_o}[n_D(z) - n_A(z)]. \qquad \textbf{4.2}$$

where ε_R and ε_0 are the static dielectric constant of the bulk semiconductor and the permittivity of free space. Poisson's equation is subjected to the boundary conditions:

$$\left|\frac{\partial v_O(z)}{\partial z}\right|_{z=0} = 0, \quad v_O(0) = 0.$$

In one dimension equation 4.2 has a solution [1]:

$$v_i(z) = \frac{e^2}{\varepsilon_0 \varepsilon_R} \int_0^z dz' \int_0^{z'} dz'' [n_D(z) - n_A(z)], \qquad 4.3$$

Except for the case of a compensated doping superlattice, which contains the same amount of donors and acceptors per period d, i.e.

$$\int_{-d/2}^{d/2} dz n_D(z) = \int_{-d/2}^{d/2} dz n_A(z), \qquad 4.4$$

the condition of macroscopic neutrality of the crystal requires a periodic electron or hole space charge distribution –en(z) or ep(z), respectively. These mobile charges provide a Hartree contribution to the superlattice potential [1]

$$v_H(z) = \frac{e^2}{\varepsilon_R \varepsilon_o} \int_0^z dz' \int_0^{z'} dz'' [-n(z) + p(z)]. \qquad 4.5$$

The exchange and correlation correction due to the free charge carriers can also be taken into account by adding the factor $V_{XC}(z)$ to the superlattice potential (P. Ruden and G.H.Döhler 1983) [2]

$$V_{XC}(z) = -0.611\left(\frac{e^2}{4\pi\varepsilon_R\varepsilon_o}\right)\left(\frac{4\pi}{3n(z)}\right)^{\frac{-1}{3}} \qquad 4.6$$

The final superlattice self-consistent potential $v_{sc}(z)$ is the sum of the bare ion contribution (4.3), the Hartree part (4.5) and the exchange and correlation potential (4.6)

$$v_{sc}(z) = v_i(z) + v_H(z) + v_{XC}(z) \qquad 4.7$$

For a known shape of the superlattice potential $v_{sc}(z)$ the discrete energy eigenvalues $\varepsilon_{i,\mu}$ can be obtained for the electrons and holes in the potential wells by solving the

Schrödinger equation. The self-consistent one-particle Schrödinger equation, which have to be solved, is [1]

$$\{-(\hbar^2 / 2m_i)\Delta + v_{sc}(z)\}\phi_{i.\mu.\kappa.}(r) = \varepsilon_{i.\mu}(\kappa)\phi_{i.\mu.\kappa.}(r) \qquad \textbf{4.8}$$

The subscript i stands for electrons in the conduction band (c), light (vl) and heavy holes (vh) and possibly spin-orbit split-off holes (vs). The index $\mu = 0, 1, 2, \ldots$ and the wave vector κ are the quantum numbers of the subbands.

Separating the quasifree particle solution for propagation parallel to the doping layer with kinetic energy $\hbar^2\kappa_{||}^2 / 2m_i$ from the z-dependent motion in the superlattice direction one obtains

$$\phi_{i.\mu.\kappa.}(r) = exp(i\kappa_{||}r_{||})u_{i.\kappa_0}(r)\xi_{i.\mu.\kappa_z}(z) \qquad \textbf{4.9}$$

where $u_{i.\kappa_0}(r)$ is the lattice periodic parts of the Bloch function of the i-band at κ_0 and $\xi_{i.\mu.\kappa_z}(z)$ is the envelope function of the i, μ subband with momentum κ_z. The Schrödinger equation then reduces to

$$[\frac{-\hbar^2}{2m_i}\frac{d^2}{dz^2} + v_{sc}(z)]\xi_{i.\mu.\kappa_z}(z) = \varepsilon_{i.\mu}(\kappa_z)\xi_{i.\mu.\kappa_z}(z) \qquad \textbf{4.10}$$

and the subband energies become

$$\varepsilon_{i.\mu}(\kappa) = \hbar^2\kappa_{||}^2 / 2m_i + \varepsilon_{i.\mu}(\kappa_z) \qquad \textbf{4.11}$$

The κ_z dependence of $\varepsilon_{i.\mu}(\kappa_z)$ in equations 4.10 and 4.11 may be disregarded by neglecting the interaction between neighbouring potential wells and the envelope function becomes:

$$\xi_{i.\mu.\kappa_z}(z) = \sum_m exp(i\kappa_z md)\xi_{i.\mu.}(z - md). \qquad \textbf{4.12}$$

Where $\varepsilon_{i.\mu}$ and $\xi_{i.\mu.}(z)$ are the eigenvalues and eigenfunctions for a single potential well.

For a compensated ground state homogeneously doped superlattice with a periodic variation of n-and p-type material, $n_D(z+d)=n_D(z)=n_A(z+d)=n_A(z)$, $d_n=d_P$, and $d_i=0$ where z is the direction of periodicity, d_n and d_P are the thicknesses of the n-and p-layers and d is the superlattice period respectively (see figure 4.1).

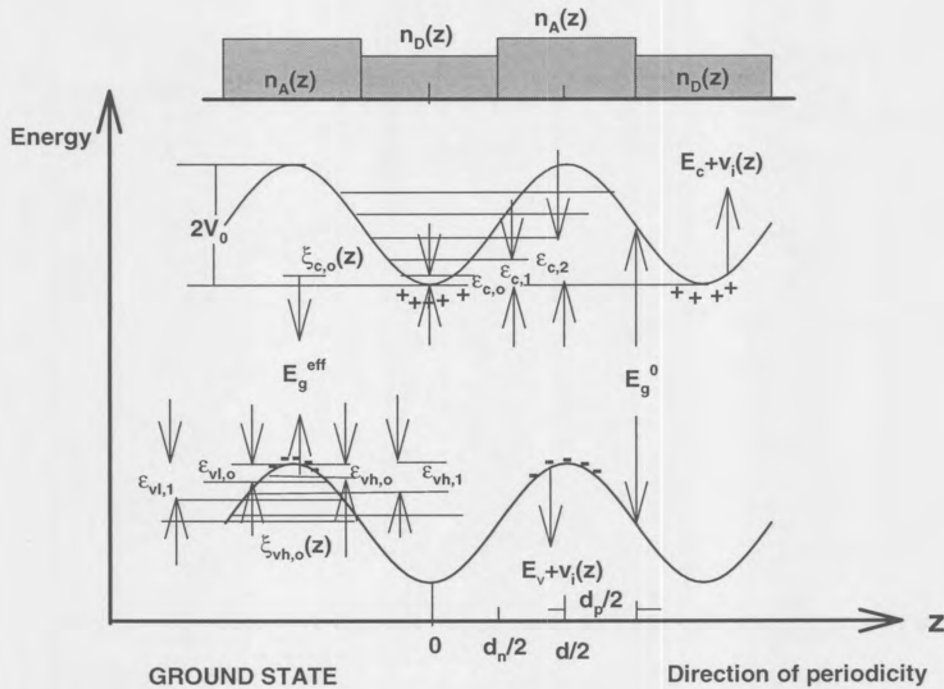

Figure 4.1 Schematic diagram for n-p doping superlattice at ground state.

The periodic space-charge potential of a DSL with the above design parameters contains only the bare ionized impurity potential $v_i(z)$, where $v_i(z)$ is parabolic and from equation 4.2 has amplitude of [1]

$$v_O(z)=\frac{e^2 n_D d_n^2}{8\varepsilon_R\varepsilon_o}, \qquad \textbf{4.13}$$

ignoring the contribution from the Hartree potential (4.5) and the exchange and correlation correction (4.6). The subband energies and the envelope wave functions are exact solutions of the harmonic oscillator within the parabolic part of the respective potential, with

$$\varepsilon_{c,\mu} = \hbar[\frac{n_D}{\varepsilon_0 \varepsilon_R m_c}]^{1/2}[\mu + \frac{1}{2}], \text{ (in eV).} \quad \textbf{4.14a}$$

and

$$\varepsilon_{v,\mu} = \hbar[\frac{n_A}{\varepsilon_0 \varepsilon_R m_v}]^{1/2}[\mu + \frac{1}{2}], \text{ (in eV).} \quad \textbf{4.14b}$$

for electrons and holes (light and heavy) respectively.

Energy values given by equations (4.14) are the offset values from the bottom of the potential well in which the electrons and holes are situated. The band edge energy should be included to obtain the total energy from which the effective band gap can be calculated. Total electron energy in the conduction band is therefore

$$\varphi_c = E_g^0 - V_0 + \varepsilon_{c,\mu}, \quad \textbf{4.15a}$$

and the total energy in the valence band is

$$\varphi_v = V_0 - \varepsilon_{vh,\mu}, \quad \textbf{4.15b}$$

The effective band gap is then given by

$$E_g^{eff,0} = \varphi_c - \varphi_v,$$

$$= E_g^0 - 2V_0 + \varepsilon_{c,0} + \varepsilon_{vh,0}. \quad \textbf{4.16a}$$

The ground state effective band gap at room temperature (300k) for $d_n = d_P = 40$ nm is given by

$$E_g^{eff} = E_g^0 - 2V_0 + \varepsilon_{c,0} + \varepsilon_{vh,0} = (1.422 - 0.55 + 0.021 + 0.07)eV \cong 0.963 eV \quad \textbf{4.16b}$$

4.2.2- Effective width approximation

Usually, the so-called effective width approximation is used to describe the DSL potential $v_0(z)$, which include flat and linear neutral parts and parabolic sections in between. This approach is especially suitable at low temperatures and for large superlattice periods $d = d_n + d_p + 2d_i$ [17]. In another variation n-i-p-i crystals constitute a semiconductor structure with a series of n and p types in between which undoped regions can be arranged. Figure 4.2a shows homogeneously doped n and p layers of thickness d_n and d_p with donor concentration n_D and acceptor concentration n_A, respectively, with intrinsic layers of thickness d_i in between. The rectangular blocks represent the homogeneous doping profiles, which are symmetric with respect to the origin, placed in the middle of an n-type doped layer.

G.H.Döhler et al (1982) [3] calculated the periodic space charge potential of such a nipi superlattice with the following approximations. (1)- Assume that the impurity space charge is exactly neutralized in the central region of width d_n^o and d_p^o in the respective n-and p-layers by free carriers, whereas the impurity space charge is uncompensated in the remaining fractions of the doping layers of width [3]

$$2d_n^+ = d_n - d_n^0 \qquad \textbf{4.17a}$$

and

$$2d_p^- = d_p - d_p^0, \qquad \textbf{4.17b}$$

respectively, due to the free carrier diffusion into the intrinsic layers where electrons and holes neutralize each other (See figure 4.2b). (2)- Any subband effects resulting from the quantization of the motion in the direction of periodicity may be neglected, if the layers are sufficiently thick.

UNIVERSITEIT VAN PRETORIA
UNIVERSITY OF PRETORIA
YUNIBESITHI YA PRETORIA

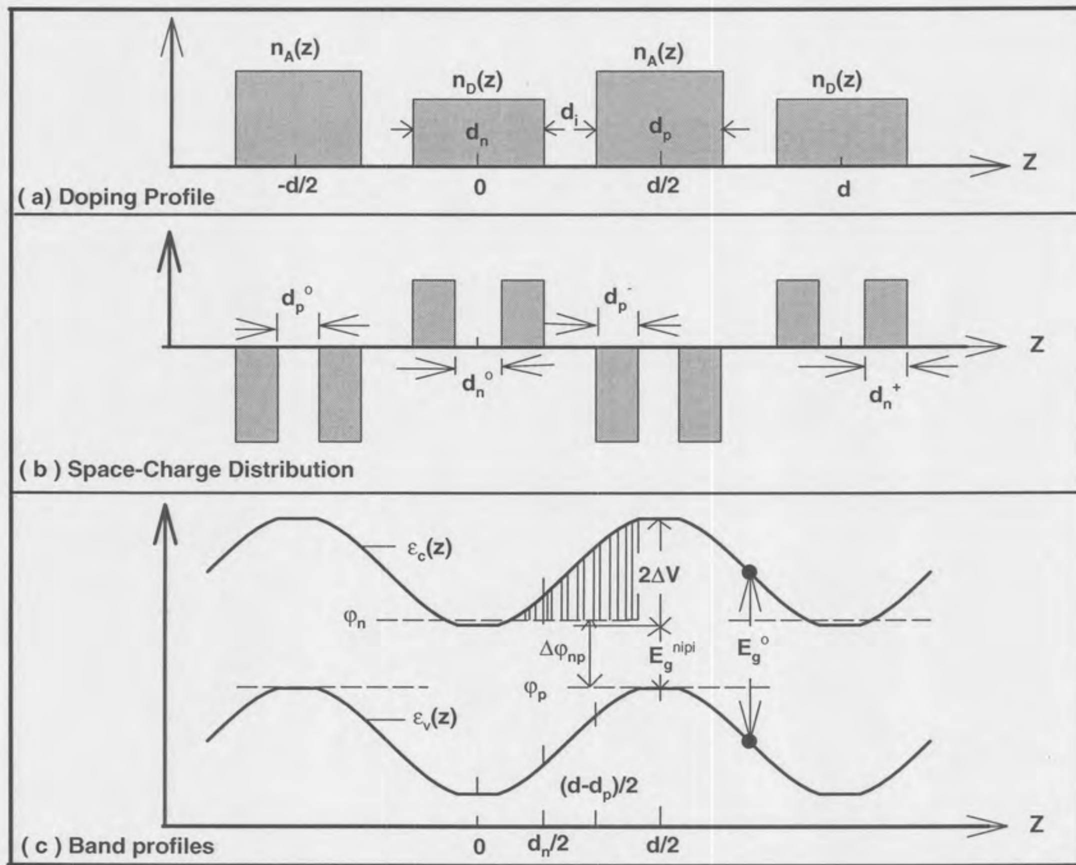

Figure 4.2 Schematic diagram showing (a) doping profile (b) space-charge distribution and (c) band profile versus growth direction Z in a periodic nipi doping structure at given layer thickness d_n, d_p and d_i and doping concentrations n_D, n_A and $n_i = 0$ in the n- and p-doped and intrinsic layers, respectively.

The electron and hole two-dimensional density per n- and p-layer are given as

$$n^{(2)} = n_D d_n^0 \text{ and } p^{(2)} = n_A d_P^0, \tag{4.18}$$

respectively.

From the condition for macroscopic neutrality of the crystal it follows that:

$$n_D d_n^+ = n_A d_P^-. \tag{4.19}$$

And then the two-dimensional electron and hole density can be rewritten as

$$n^{(2)} = p^{(2)} + n_D d_n - n_A d_P. \tag{4.20}$$

See figure 4.2c for the space charge potential calculation. The periodic space charge potential $v_O(z)$ for $-d/2 < Z < d/2$ will be the contribution from the neutral part of the doped layer (1), the ionized region (2) and the intrinsic layer (3). The space charge potential in the corresponding regions is then [3]:

(1) Constant in the neutral part of the doping layers, i.e.,

$$v_O(z) = \begin{cases} 0 & \text{for } |z| < \frac{d_n^0}{2} \\ 2\Delta V & \text{for } (\frac{d - d_P^0}{2}) < |z| < \frac{d}{2} \end{cases}, \quad 4.21$$

(2) Parabolic in the ionized impurity regions, i.e. in SI units,

$$v_O(z) = \begin{cases} (\frac{e^2 n_D}{2\varepsilon_0 \varepsilon_R})(|z| - \frac{d_n^0}{2})^2 & \text{for } \frac{d_n^0}{2} < |z| < \frac{d_n}{2} \\ 2\Delta V - (\frac{e^2 n_A}{2\varepsilon_0 \varepsilon_R})(|z| - \frac{d - d_P^0}{2})^2 & \text{for } \frac{d - d_P}{2} < |z| < \frac{d - d_P^0}{2} \end{cases}, \quad 4.22$$

(3) Linearly increasing in the intrinsic layers i.e.,

$$v_O(z) = (\frac{e^2 n_D d_n^+}{\varepsilon_0 \varepsilon_R})(\frac{d_n^+}{2} + |z| - \frac{d_n}{2}) \quad \text{for } \frac{d_n}{2} < |z| < (\frac{d - d_p}{2}). \quad 4.23$$

And the amplitude or the total modulation width $2\Delta V$ of the space-charge potential (see figure 4.1c) is given by

$$2\Delta V = v_O(\frac{d}{2}) - v_O(0) = (\frac{e^2}{\varepsilon_0 \varepsilon_R})[\frac{n_D (d_n^+)^2}{2} + \frac{n_A (d_P^-)^2}{2} + n_D d_n^+ d_i]. \quad 4.24$$

The potential $v_O(z)$ is modulating the conduction and the valence bands. For the band edge one has

$$\varepsilon_c(z) = E_c + v_O(z), \quad \textbf{4.25a}$$

and

$$\varepsilon_v(z) = E_v + v_O(z), \quad \textbf{4.25b}$$

with

$$E_c = E_v + E_g^0. \quad \textbf{4.25c}$$

Therefore, the effective energy gap E_g^{nipi} of the doping superlattice, i.e., the energy difference between the lowest electron states in conduction band and the uppermost hole states in valence bands, is reduced by $2\Delta V$ compared with the unmodulated bulk value E_g^0 due to the periodic space-charge potential (quantum effects are neglected)

$$E_g^{nipi} = \varepsilon_c(z=0) - \varepsilon_v(z=d/2) = E_g^0 - 2\Delta V. \quad \textbf{4.26}$$

the difference between electron and hole quasi-Fermi-levels $\Delta\varphi_{np}$ corresponds approximately to E_g^{nipi} as long as there are neutral regions of a finite width, d_n^0 and d_P^0, in the doping layers.

For a thin layer or for d_n^0 and d_P^0 equal to zero, the space charge potential $v_O(z)$, (4.22) and (4.23) and the amplitude 4.24 can easily be shown to reduce to [2]:

$$v_O(z) = \begin{cases} \left(\dfrac{e^2 n_D}{2\varepsilon_0\varepsilon_R}\right) z^2 & for \ |z| \le \dfrac{d_n}{2} \\ 2\Delta V - \left(\dfrac{e^2 n_A}{2\varepsilon_0\varepsilon_R}\right)\left(\dfrac{d}{2} - |z|\right)^2 & for \ \dfrac{d}{2} - |z| \le \dfrac{d_p}{2} \end{cases}, \quad \textbf{4.27}$$

for the parabolic parts in the doping layers,

$$v_O(z) = \left(\frac{e^2 n_D}{2\varepsilon_0\varepsilon_R}\right)\left(|z| - \frac{d_n}{4}\right) \quad \text{for } \frac{d_n}{2} \le |z| \le \left(\frac{d - d_p}{2}\right), \quad \textbf{4.28}$$

for linear parts in the intrinsic regions and

$$2\Delta V = \left(\frac{e^2}{\varepsilon_0 \varepsilon_R}\right)\left(\frac{n_D d_n^{\ 2}}{8} + \frac{n_A d_P^{\ 2}}{8} + \frac{n_D d_n d_i}{2}\right), \qquad \textbf{4.29a}$$

is the maximum height of $v_O(z)$ (total modulation depth) [2]

Which also reduces to

$$2\Delta V = \frac{e^2 n_D d_n^2}{4\varepsilon_0 \varepsilon_R}\ , \qquad \textbf{4.29b}$$

for $d_p = d_n$, $n_A = n_D$ and $d_i = 0$.

4.2.3- The Pumping Factor -r

In the formulation of D.V.Ushakov et al (1997) [17], for optically or electrically excited DSL's a pumping factor r is introduced in the expressions for the effective doped layer width, equation 4.17. And hence the effective doped layer width is now given as:

$$2d_n^+ = d_n\left(1 - \frac{n^{(2)}}{n_D d_n}\right) = d_n(1-r), \qquad \textbf{4.30a}$$

$$2d_p^- = d_p\left(1 - \frac{p^{(2)}}{n_A d_p}\right) = \frac{n_D d_n}{n_A}(1-r), \qquad \textbf{4.30b}$$

where

$$r = \frac{n^{(2)}}{n_D d_n}\ , \qquad \textbf{4.30c}$$

is the pumping factor [17]. From macroscopic electroneutrality condition follows the equality

$$p^{(2)} = n^{(2)} + n_A d_p - n_D d_n = n^{(2)} + N, \qquad \textbf{4.31}$$

where N is given by $N = n_A d_p - n_D d_n$.

The pumping factor r is a function of the two-dimensional carrier concentration ($n^{(2)}$ and $p^{(2)}$) and varies between almost zero and up to one for a highly excited superlattice. The potential profile depth as a function of this pumping factor can easily be derived from equation 4.24 with appropriate substitutions (Appendix B). And this is written as follows:

$$2\Delta V = \frac{e^2 n_D d_n}{4\varepsilon_0\varepsilon_R}[2d_i + \frac{(n_A + n_D)}{2n_A}d_n][1-r]\left\{1 - \frac{r}{1 + \frac{4n_A d_i}{(n_A + n_D)d_n}}\right\}, \qquad \textbf{4.32}$$

and this will reduce to

$$2\Delta V = \frac{e^2 n_D d_n}{4\varepsilon_0\varepsilon_R}[2d_i + d_n][1-r]\left\{1 - \frac{r}{1 + \frac{2d_i}{d_n}}\right\}, \qquad \textbf{4.33}$$

for $n_A = n_D$ and $d_n = d_p$. And for DSL without the intrinsic layer, 4.32 reduces to

$$2\Delta V = \frac{e^2 n_D d_n^2}{4\varepsilon_0\varepsilon_R}[1-r]^2. \qquad \textbf{4.34}$$

Equations 4.32-4.34 show that the pumping factor has a larger influence for a compensated superlattice without the intrinsic layers.

UNIVERSITEIT VAN PRETORIA
UNIVERSITY OF PRETORIA
YUNIBESITHI YA PRETORIA

CHAPTER 5

Sample Parameters, Experimental Set-up, Measuring Techniques And Equipment Used

5.1. Sample Parameters..51
5.1.1- Growth of GaAs Doping Superlattice by OMVPE....................51
5.1.2- Post Growth Modification Of Doping GaAs Superlattice..........52
5.2. Refractive Index Measurements....................................53
5.2.1- Experimental Set-up..53
5.2.2- Equipment..54
5.2.3- Experimental Techniques..55
5.3. Near IR Reflectance Measurements.................................59
5.3.1- Experimental Set-up..59
5.3.2- Equipment..60
5.3.3- Experimental Techniques..61
5.3.4- Reflectance Calculation..63
5.4. Photoluminescence And Resonance Raman Measurements..............63
5.4.1- Experimental Set-up..63
5.4.2- Equipment..64
5.4.3- Experimental Techniques..65
5.5. Normal Raman Measurement..66
5.5.1- Experimental Set-up..67
5.5.2- Experimental Techniques..68

CHAPTER 5

Sample Parameters, Experimental Set-up, Measuring Techniques And Equipment Used

Sample parameters, measuring techniques, experimental set-up and equipment used throughout the whole experiment will be discussed in this chapter. This chapter is divided in to four parts: part A concentrates on sample parameters, part B will discuss the ellipsometry measurements, part C will cover the near infrared reflectance measurements, and part D will concentrate on photoluminescence and Raman (resonant and normal) measurements.

Part A:

5.1- Sample Parameters

5.1.1- Growth of GaAs doping superlattices by OMVPE

The GaAs doping superlattice (DSL) structures were grown by low-pressure OMVPE on semi-insulating GaAs substrates at a temperature of 650°C. Purified hydrogen was used as the carrier gas with a flow rate of $600\,cm^3\,/\,min$. Trimethylgallium (TMG) and arsine (AsH_3) were used as the group III and V sources for the growth of GaAs, with a III/V ratio of 1/150. In the doping superlattices, the n-layers were doped with tellurium atoms to produce a donor concentration of $n_D = 10^{18}\,atom\,/\,cm^3$ and the p-layers were doped with zinc atoms to produce an acceptor concentration of $n_A = 10^{18}\,atom\,/\,cm^3$. The doping concentrations in the DSL's were chosen to be as

high as possible in order to produce a large space charge potential at the p-n interfaces, and thus achieve a large modulation of the host band structure. An undoped GaAs buffer layer 0.5micron thick was first deposited on the GaAs substrate. The first superlattice layer deposited on the buffer layer was p-doped, while the last (top) layer was n-doped in the sample. In this experiment the thicknesses of the n-doped (d_n) and p-doped (d_p) layers of the DSL's are the same and equal to 40nm.

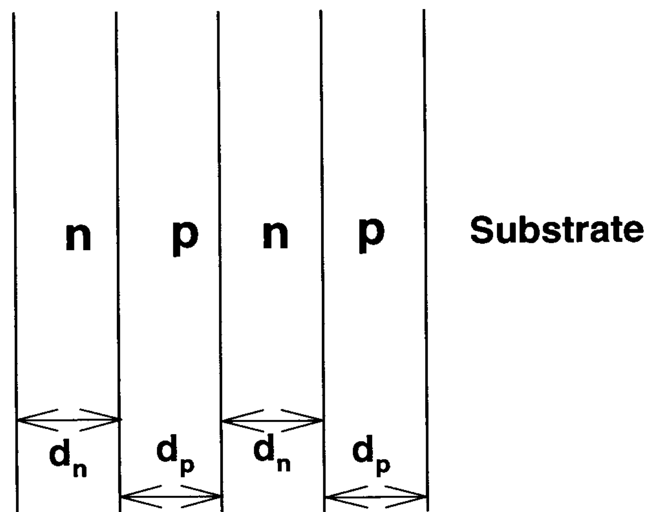

Figure 5.1 shows the layer sequence in the 'np' doping superlatice. The layer thickness d_n=d_p=40nm.

5.1.2- Post Growth Modification Of GaAs Doping Superlattices

Four pieces of GaAs doping superlattices were cut from the same disc. Three pieces were implanted with hydrogen ions while one remained virgin. The hydrogen ions were implanted with a beam diameter of about 2mm. The hydrogen implantation doses for the three samples were $10^{12}\,cm^{-2}$, $10^{14}\,cm^{-2}$ and $10^{16}\,cm^{-2}$. Ellipsometry, near infrared reflectance, PL and Raman measurements were taken for these samples. After these measurements, the samples were annealed at high temperature for about two hours, to remove implantation related damage. The sample with $10^{12}\,cm^{-2}$

implantation dose was annealed at a temperature of $500^{0}C$, while the other two samples, with higher implantation dose, needed to be annealed for another two hours at a temperature of $600^{0}C$. This temperature is about the maximum for annealing of GaAs without affecting the atomic ratio due to sublimation of As.

Part B:

5.2- Refractive Index Measurements

This section will discuss the experimental set-up, equipment used and experimental procedures performed for measuring the ellipsometric angles Psi (Ψ) and Delta (Δ).

5.2.1- Experimental Set-up

In this section the experimental set-up and equipment used will be discussed in brief. Figure 5.2a shows the Gartner Ellipsometer Model L 119, and figure 5.2b shows a schematic layout of the experimental set-up used, where A, M, P and QW stand for aperture, mirror, polarizer and quarter wave plate.

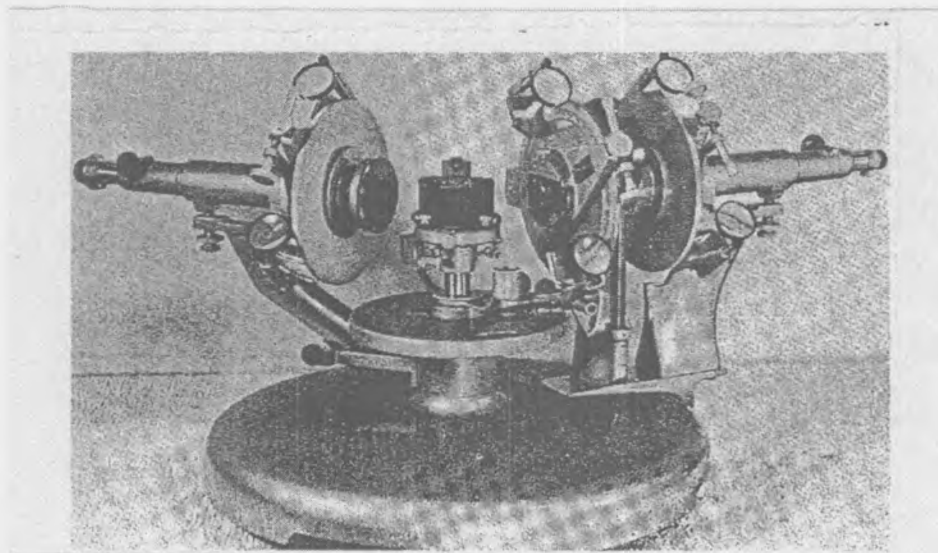

Figure 5.2 (a) The Gartner Ellipsometer Model L 119.

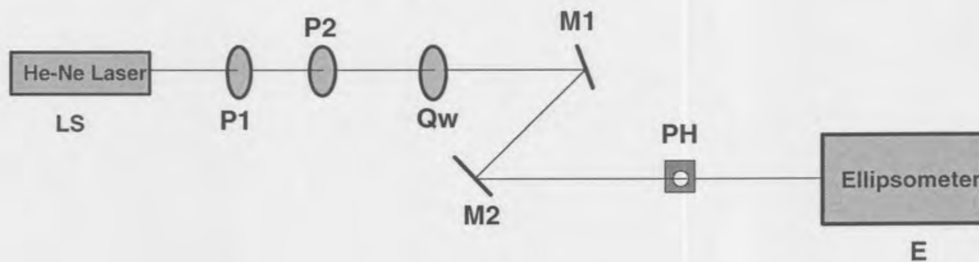

Figure 5.2b. The schematic layout for the ellipsometry experiment.
The layout shows the He-Ne laser source (LS), polarizers (P1 and P2), quarter wave plate (QW), mirrors (M1 and M2), pinhole (PH) and the Ellipsometer (E).

5.2.2- Equipment

The equipment used in this experiment is shown in figure 5.2b. This section will describe the components of the ellipsometer.

5.2.2.1- Components Of Ellipsometry

1-The Polarizer:

An iris diaphragm or pinhole entrance aperture is mounted on a 250mm collimator with 28.4mm aperture, having rack and pinion focusing. The objective mount of the collimator supports a 6.25in diameter divided circle assembly with a 14mm Glan-Thompson prism centred and aligned to the rotational bearing. The angular position of the prism is read with two opposing verniers to an accuracy of 0.01 degree. Each vernier is equipped with a right-angle mirror and an adjustable magnifier. The divided circle assembly rotates through 360 degrees and a fine motion tangent screw assembly is provided.

2- Compensator:

A similar divided circle assembly, complete with opposing verniers, mirrors, magnifiers and fine motion tangent adjustment supports a rotating dovetail mount, designed to accommodate a suitably mounted (mica) quarter wave plate.

3- The Analyzer:

The final component is a telescope and rotating Glan-Thompson prism assembly identical to the collimator but supported by a bearing, which permits it to rotate around a central axis to change the angle of incidence and reflection to and from the substrate surface. This angle is measured with a horizontally divided circle, diameter 6.5/8 in., divided into increments of 20 minutes and read by opposing verniers to an accuracy of 20 seconds.

5.2.3- Experimental Techniques

The experimental procedure for the measurement of ellipsometric angles will be given in this section. This section is divided in to two parts: part one is devoted to the calibration of Ellipsometer while part two discusses the measuring procedure.

5.2.3.1- Ellipsometer Calibration

The analyser, compensator (quarter wave plate) and the polarizer circle should be calibrated before taking measurements to avoid offsets of the actual 0 degree settings. The following steps were used for the calibration of the ellipsometer in the order: analyser-polarizer and finally the compensator. One can also do it the other way round (polarizer- analyser and compensator).

1- Calibration Of The Analyzer Circle

- Steer the probe beam through the aperture to the telescope of the ellipsometer while the quarter wave plate is in position.
- Mount a clean quartz plate, for which the refractive index is known, in the sample holder. The quartz plate must be thick enough or coated at the back (black) to avoid additional reflections from the back surface.
- Set the ellipsometer table to 180^0.
- Rotate the sample (quartz) holder until the reflected beam retraces to the incoming laser beam. Fine tune left/right and up/down with the three levelling screws attached to the sample holder for final adjustments.
- Rotate the table through $180^0 - \theta_B$, where θ_B is the Brewster angle, and fasten. This angle differs for the different probe beams used. The probe beams (He-Ne-laser) used are red (632.8nm), yellow (594nm), and green (543.5nm) and the corresponding Brewster angles for quartz are $55^0 32' \cong 55.53^0$, $55^0 34' \cong 55.57^0$ and $55^0 36' \cong 55.60^0$ respectively.
- Rotate the telescope until the ellipsometer table shows an angle equal to the Brewster angle.
- Set the analyser circle to zero transmission to locate the zero position of the analyser (analyser is at horizontal). This setting shows the deviation ΔA from the actual analyser position, which is at 0^0 (ΔA could be ≥ 0 or ≤ 0). ΔA must be subtracted from the reading A_R to find the correct analyser position ($A = A_R - \Delta A$).

2- Calibration Of The Polarizer Circle

- Remove the quartz plate. Rotate the telescope back to $124^0 28' \cong 124.47^0$, $124^0 26' \cong 124.43^0$ and $124^0 24' = 124.40^0$ for the red, yellow and green laser beams respectively.
- Rotate the table back to 180^0 and check that the beam still passes through the telescope.

- Remove the quarter wave plate and leave the analyser at zero transmission (ΔA).
- Set the polarizer to the zero beam transmission position. This setting is the 90^0 setting of the polarizer (polarizer is vertical). Let ΔP (≥ 0 or ≤ 0) be the deviation of the polarizer from the actual value at zero transmission setting. ΔP must be subtracted from the reading P_R to find the correct polarizer position ($P = P_R - \Delta P$).

3- Calibration Of The Quarter Wave Plate Circle (Compensator)

- Replace the quarter wave plate (compensator).
- With table at 180^0 the polarizer is set at $+45^0 + \Delta P$ and the analyser at $-45^0 + \Delta A$.
- The setting that extinguishes the beam will give the desired inclination of $+45^0$ of the fast axis of the compensator. The compensator circle was set at and locked in this orientation. Now the ellipsometer is calibrated.

5.2.3.2- Measurements Of The Ellipsometric Angles

In this section the measurement techniques will be discussed step by step. Three different probe beams at different intensity were used in this experiment. All measurements were performed in air in a dark room over a range of angles of incidence between 50^0 and 80^0 inclusive in steps of 5^0. For each and every angle of incidence five measurements were taken and the average values were recorded to minimize the experimental error. A monochromatic beam passed through a variable polarizer (P) to produce light with a known polarization state. This light interacts with the optical system (sample) and its polarization is modified. A variable polarization analyser measures the modified state of polarization at the output. The procedure is as follows (Refer to figure 5.2b):

- Steer the probe beam through the ellipsometer.
- Mount the sample in the sample holder and set the ellipsometer table to 180^0 and fasten. Note that the sample holder and ellipsometer table rotate separately about the same axis.
- Rotate the sample holder until the reflected beam retraces the incoming beam and fasten the holder. The overlap is checked on the pinhole (see figure 45.2b). Use the levelling screws if necessary.
- Turn the ellipsometer table to 180^0 minus angle of incidence.
- Swing the telescope to the angle of incidence and fine-tune it to get the reflected beam to pass through the centre of the analyzer.
- Adjust the analyzer circle and the polarizer circle in such a way that the reflected light through the analyzer extinguishes. These extinction settings of the analyzer and the polarizer were determined by the direct visual method.
- Two possible extinction settings of the analyzer (A_R and A'_R) and the polarizer (P_R and P'_R) are always found. The extinction setting A_R, and A'_R should always be in the fourth and first quadrant respectively while P'_R is either in the first or second and $P'_R > P_R$. The deviation ΔA and ΔP must be subtracted from the readings before evaluation.

Extinction Settings:

The extinction settings of the polarizer and analyzer were obtained by the direct visual method. This is done by direct viewing of the reflected beam with a Gauss eyepiece on the telescope while simultaneously adjusting the analyzer and polarizer circles. This method suffers from the disadvantage that measurements must be made in a dark room.

Variation of intensity:

The second polarizer P2 shown in fig5.2b was set at horizontal and remained fixed throughout the whole experiment. The first polarizer P1 was used to vary the

intensity, as a DSL is very sensitive to the illuminating laser power (intensity). The quarter wave plate (QW) with its fast axis set at 45^0 to the optical axis was located after the horizontal polarizer. Hence the light beam incident to the ellipsometer aperture becomes circularly polarized. Having a circularly polarized beam will avoid the false null position relating to the laser source instead of the sample. The pinhole (PH) was used for the back reflection adjustment.

Part C:

5.3- Near Infrared Reflectance Measurements

In this section, the experimental set-up, equipment, experimental techniques and method of obtaining reflectance will be discussed briefly.

5.3.1- Experimental Set-up

The schematic layout of the experimental set up and instrumentation used for the near infrared room temperature measurements are shown in figure 5-3b (section 5.3.3). A 0.64m Jobin Yvon monochromator with a cooled germanium photodiode and lock-in amplifier was used for this experiment. The germanium photodiode is connected to a 200V high voltage source. The slit width was set to 1mm, which gave a resolution of 12 angstrom. The spectral recording was made with a step length of 5 angstrom. Samples were illuminated with a collimated white light beam about 1mm wide from a low power (20W) tungsten halogen lamp at an angle of incidence of 5^0 measured from the sample normal. The reflected signal from the sample, which passed through the collimating lens and horizontal polarizer, was chopped at about 15 Hz before passing through the entrance slit of the monochromator. This was necessary because a lock-in amplifier was used to process the recorded signal. The incident polarization (horizontal) of the light was maintained after reflection by putting a second polarizer between the sample and the monochromator. This prevents depolarization, which may

occur due to reflection. Reflected light was focused by a lens of 100mm focal length on to the entrance slit of the monochromator.

5.3.2- Equipment

This section gives a brief discussion on the operation of the equipment used in the near IR measurements.

1- Germanium Photodiode

The reflectance measurement was made in the wavelength range 8000-to 15000 angstrom. A solid-state detector (germanium photodiode) was used to detect signal in this wavelength range. This detector operates at liquid-nitrogen temperature. The solid-state detector is basically a reverse biased p-n junction diode. When photons with energy greater than the band gap (0.74ev(~16740 angstrom) for germanium at $0^0 C$) pass through the junction electron-hole pairs are produced in the junction. The internal electric field in the depletion zone sweeps the electrons towards the n-side of the junction and the holes towards the p-side. This current is recorded by the lock-in amplifier. The reverse bias is provided to ensure separation of the electrons and holes before recombination can occur.

Noise in photo detector

Noise can arise from the random generation and recombination of carriers, giving fluctuating carrier concentrations (in particular minority-carrier concentration) and also from the random diffusion (thermal noise) of carriers across the junction. This is minimized by cooling the detector.

2- Monochromator

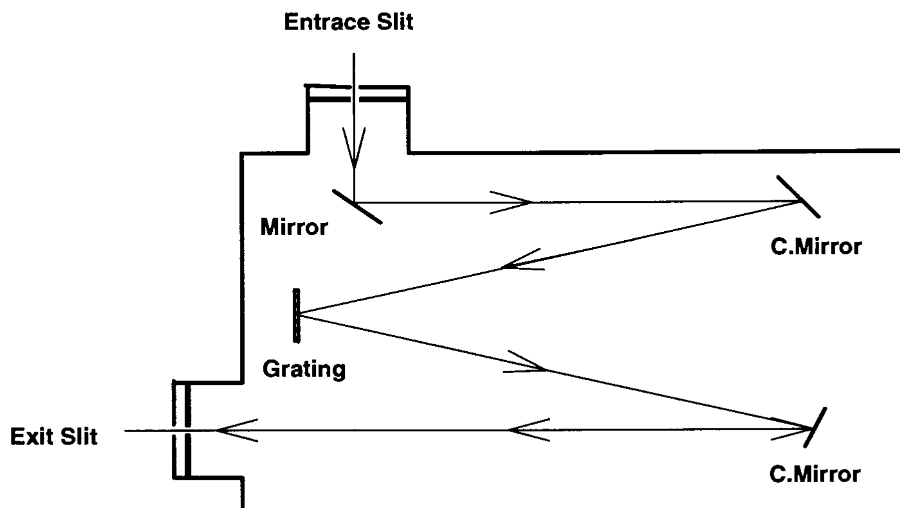

Figure 5.3-a Schematic layout of 0.64 m Jobin Yvon Monochromator.

When there is a need to separate light of different wavelengths with high resolution, a diffraction grating is usually the tool of choice. A large number of parallel, equally spaced slits (grooves) on a reflecting or transparent substrate constitute a diffraction grating. The grooves result in diffraction effects that concentrate reflected or transmitted light energy into discrete directions. With a large number of grooves the intensity maximum is very sharp and narrow, providing the high resolution required by spectroscopic applications. In this experiment, a 0.64m focal length concave mirror and a 1200 grooves/mm grating, Jobin Yvon Monochromator was used (figure 5.3a).

5.3.3- Experimental Techniques

This section is devoted to the experimental procedure used for the room temperature near infrared measurements.

UNIVERSITEIT VAN PRETORIA
UNIVERSITY OF PRETORIA
YUNIBESITHI YA PRETORIA

1- Measuring Procedure

- Mount the sample in the sample holder, illuminate it with white light at an angle of 5^0 and steer the reflected beam through the Monochromator onto the detector.
- Flush the optical path with dry nitrogen to minimize absorption by water vapour during the measurement.

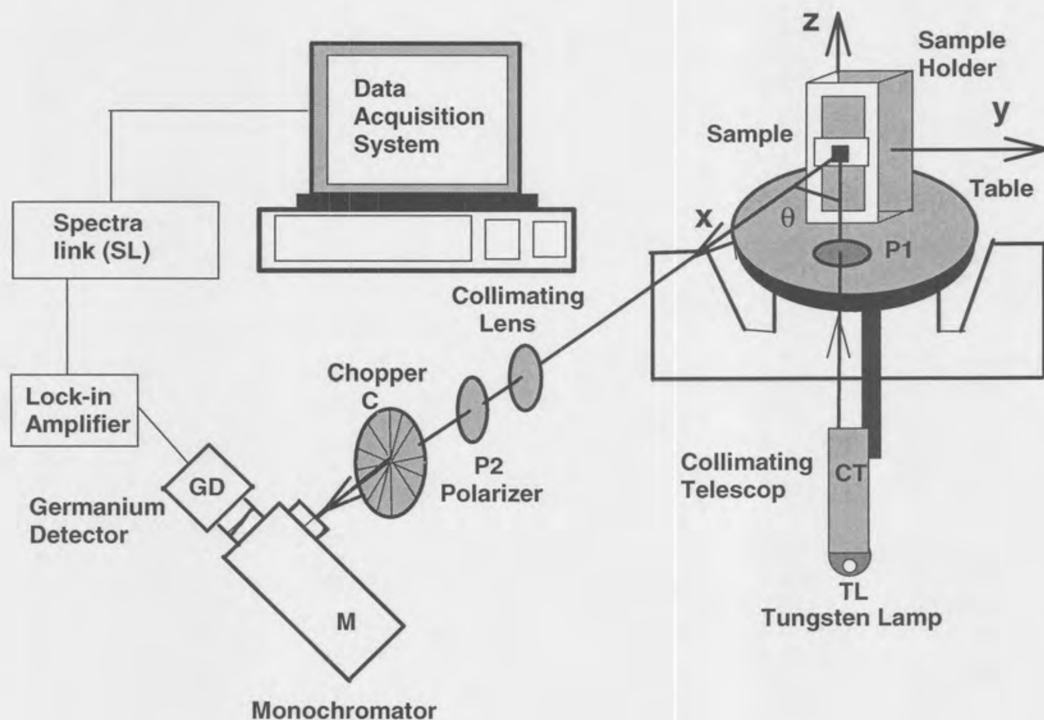

Figure 5.3b. Experimental layout for the near IR reflectance measurements showing all the equipment used. Tungsten lamp (TL), collimating telescope (CT), polarizer (P1 and P2), Mounted sample (S), collimating lens (L), chopper (C), monochromator (M), germanium detector (GD), lock in amplifier (LA), spectra-link (SL) and computer. θ is angle of incidence (magnified in the figure).

5.3.4- Reflectance Calculation

The reflected signals were recorded for all samples from 800nm to 1450nm in steps of 0.5 nm. Recorded spectra were divided point by point by a spectrum of the light source reflected from a gold reference mirror to compensate for the light source spectrum, monochromator transmission and detector efficiency.

Part D:

5.4- Photoluminescence And Resonance Raman Measurements

This section will give a brief description of the experimental set-up, equipment and experimental techniques.

5.4.1- Experimental Set-up

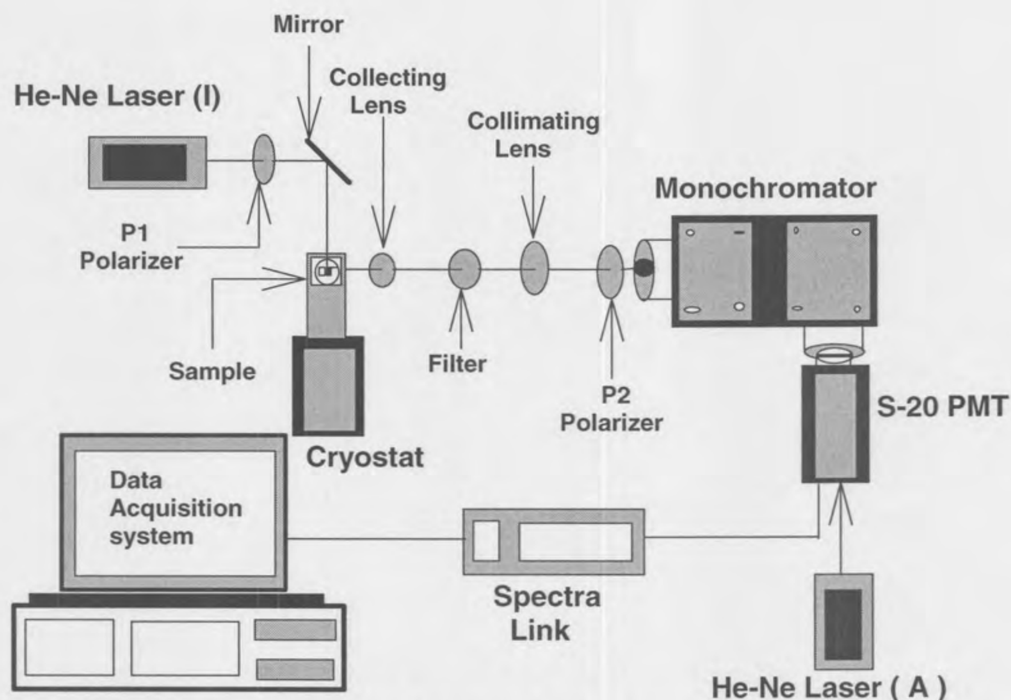

Figure 5.4a shows the schematic layout for photoluminescence and resonant Raman measurement.

The schematic layout of the experimental set-up and instrumentation used for photoluminescence (PL) and resonant Raman (inelastic light scattering) measurements is shown in figure 5-4a.

A 0.64m Jobin Yvon Monochromator with S-20 photomultiplier were used for this experiment. The slit width was set to 0.5mm. Samples were illuminated with a linearly polarized He-Ne (632.8nm) laser beam. The polarizer and filter shown in figure 5.4a were only used for the resonant Raman scattering (RR). The polarizer was used to vary the incident and the outgoing polarization of the laser, since this measurement is polarization sensitive. The scattered light was focused by a lens of 100mm focal length onto the entrance slit of the monochromator.

5.4.2- Equipment

1-Photomultiplier (PM)

Figure 5.4b shows a schematic diagram of the photomultiplier. The photomultiplier used for both resonant Raman and photoluminescence measurements was a S-20 with a photocathode made of $Na_2KSb-Cs$ for a wide spectral coverage (0.4 μm to 0.9 μm) and a low work function. The front of the photomultiplier tube (PMT) contains a photocathode, which emits electrons (photocurrent) when a photon strikes it (photoelectric effect). The photomultiplier also has numerous secondary electrodes, called dynodes (made of CsSb). Their potential is increased in succession along the length of the PM tube. The photomultiplier amplifies the photocurrent by accelerating the electrons onto successive surfaces (dynodes) from where additional electrons are ejected (figure 5.4b suggest the process). A resister chain is used to maintain a potential gradient between the dynode stages. This use of electron multiplication provides extremely low noise amplification of the initial photocurrent signal. The final current is collected by the anode.

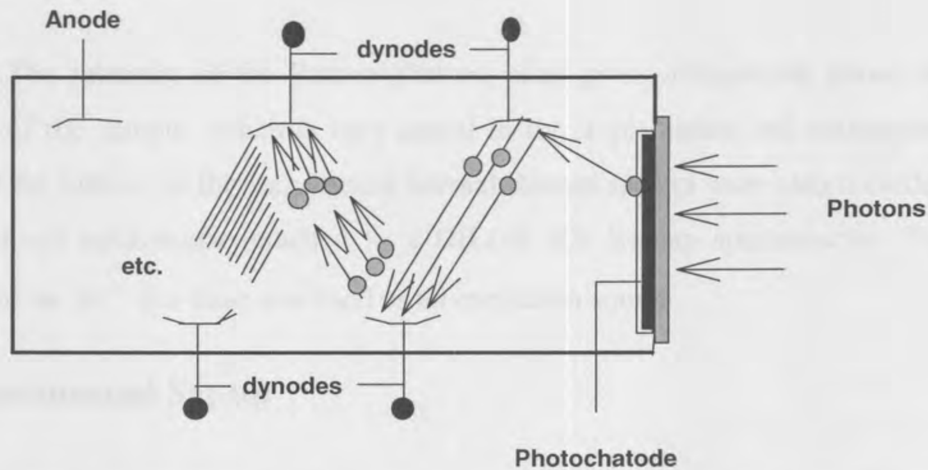

Figure 5.4b shows the photomultiplier multipliction process [18].

The quantum efficiency (QE) of the photocathode is defined as the number of the electrons emitted from the cathode per incident photon. (QE for S-20 PM is ~0.22 or ~22%).

$$QE = (S \times 1240 / \lambda) \times 100\%$$

$$S = I / P$$

$$I = Pe\lambda QE / hc$$

Where S is the radiant cathode sensitivity in A/W and λ, P and I are the wavelength in nm, the incident power in watt and the cathode current in ampere respectively. Other parameters have their usual meaning. Maximum PMT anode currents are limited to a mA or less. Even in total darkness you get a small anode current from a PM. This is caused by electrons thermally emitted from the photocathode and dynodes, and cooling the PMT can reduce this effect. It should be pointed out that a powered PMT should never be exposed to ordinary light levels, since it may require many hours to recover to its normal dark-current level.

5.4.3- Experimental Techniques

In this section we describe briefly the most common techniques used in PL and RS measurements for the characterization of DSL's material.

A wavelength range of 800 to 960 nm was used for the PL measurements while a 634- to 955 nm range was used for resonance Raman measurements. The He-Ne laser sources indicated by A and I in figure 5.4a were used for the alignment and excitation respectively. The laser spot from source A, which passed through the monochromator, collimating and collecting lenses should overlap to the spot due to laser source I at the sample. RR and PL measurements were made with an excitation power of 15mW He-Ne laser beam and at a sample temperature of 13 K.

The excitation source required for PL measurements may be any source that generates photons with sufficient energy to excite electron-hole pairs. In this work a He-Ne (cw) laser source at 632.8 nm was used. Photoluminescence measurements are generally performed well below room temperature. Cooling of the semiconductor samples results in sharper, more readily identifiable peaks. Lower temperature reduce the thermal broadening of the excited carrier energies, which at temperature T is roughly $K_B T$ [19 pp 79]. This gives a significant broadening that at room temperature is ~25meV, but reduce to ~6meV at 77k and less than 1meV at liquid helium temperatures.

Resonant Raman spectroscopy has proved to be a useful technique for measuring and studying the subband quantum levels. In this technique the exciting laser line has to be close to a strong, real interband excitation. For this experiment a He-Ne laser source at 632.8 nm was used. When a laser is incident on DSL's, the scattered light will be frequency shifted. The observed shift in frequency, which arise from the intersubband excitations, such as between $\mu = 0$ and $\mu = 1$ states in a quantum well will give information about the existence of discrete bound state and their spacing.

5.5- Normal Raman Measurement

Raman spectroscopy has become one of the most widely accepted techniques for the characterization of DSL materials. In particular, its application as a non-destructive technique for examining the damage that accompanies ion implantation is well

UNIVERSITEIT VAN PRETORIA
UNIVERSITY OF PRETORIA
YUNIBESITHI YA PRETORIA

established. The intensity of the Raman phonon peak gives information about the crystallinity of the sample, which is very useful in ion implantation and subsequent annealing of the DSL's. In this experiment normal Raman spectra were also recorded using a confocal microscope attached to a DILOR XY Raman spectrometer. The 514nm line of an Ar^+-ion laser was used as an excitation source.

5.5.1- Experimental Set-up

Figure 5.5 shows the schematic of a typical experimental setup used in Raman scattering experiments. A microscope objective lens is used to focus the laser beam onto the sample and the backscattered Raman signal is directed into a triple-pass spectrometer and then analyzed with a charge-coupled device (CCD) array.

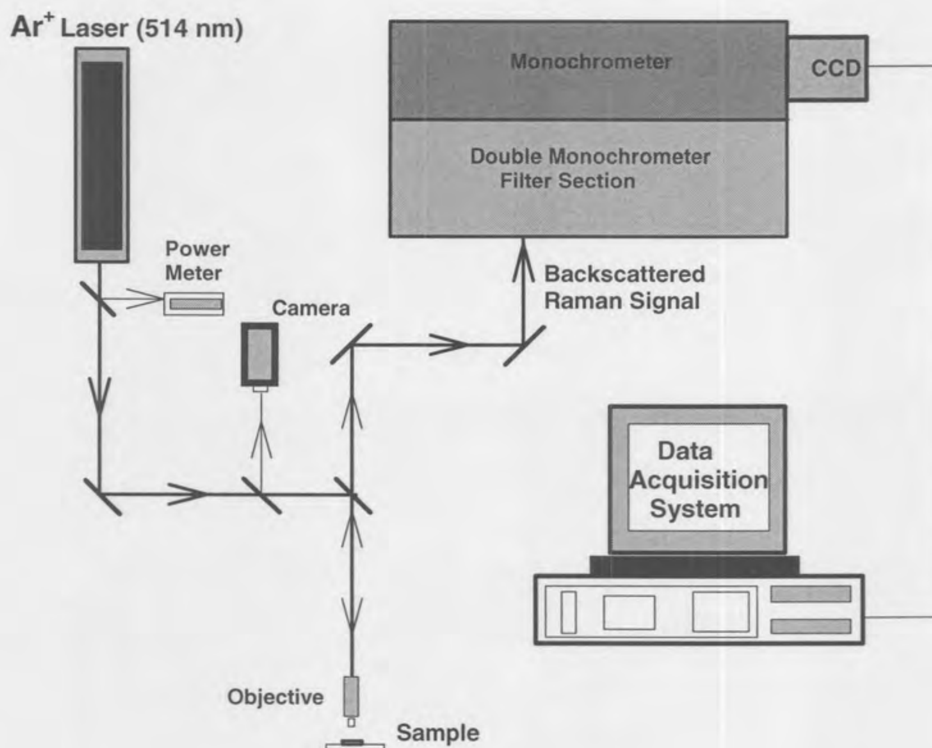

Figure 5.5 shows schematic of a typical experimental setup used in Raman scattering experiments (Adapted from [19] pp81).

5.5.2- Experimental Techniques

Light is scattered from the surface of a sample, the scattered light is found to contain mainly wavelengths that were incident on the sample (Rayleigh scattering) but also different wavelengths at very low intensities that represent an inelastic interaction of the incident light with the material. If the incident photon imparts part of its energy to the lattice in the form of phonons (phonon emission) it emerges as a lower-energy photon. This down-converted frequency shift is Stokes-shifted. And it is this weak Stocks-mode scattering that is usually monitored.

One of the main factors influencing the design of RS experiments is that the weak Raman signal is spectrally very near the exciting laser light. Thus the weak Raman phonon peak must be measured against a background of intense Rayleigh scattering. Raman measurements require a fairly strong laser source, well-designed optics to filter out the Rayleigh signal, and a sensitive detector to record a very weak signal.

A typical Raman experimental setup is shown in figure 5.5. The laser is focused on the DSL's with a lens and the signal usually is collected in a backscattering configuration. This Raman signal is directed into a double monochromator to discriminate against the unwanted Rayleigh light and spectrally resolve the signal.

Note that the same photoluminescence and Raman measurements were also made for the annealed samples.

CHAPTER 6

Results And Discussion

6.1. Ellipsometry Measurement..70

6.1.1- Evaluation of Ellipsometric Angles And Graphical Representation 70

6.1.2- Graphical Comparison of Extinction Coefficient Values..........76

6.1.3- Optical Constants..76

6.2. Near Infrared Reflectance Measurement 78

6.2.1- Reflectance Spectrum 78

6.2.2- Evaluation of Real Refractive Index 81

6.3. Photoluminescence And Raman Measurements..................88

6.3.1a- Photoluminescence Measurement Before Annealing 88

6.3.1b- Photoluminescence Measurement After Annealing 91

6.3.2a- Normal Raman Measurement Before Annealing 93

6.3.2b- Normal Raman Measurement After Annealing 94

6.3.2c- Resonance Raman Measurement 95

CHAPTER 6

Results And Discussion

In this chapter the experimental and theoretical results will be discussed. The experimental results obtained from single wavelength ellipsometer measurements, near infrared room temperature reflectance measurements, photoluminescence and Raman (normal and resonant) spectroscopy measurements are given in this chapter. The analysis of the results is also included in the corresponding parts of the measurement techniques used. For convenience this chapter is divided in to three sections in the following orders:

(1) Ellipsometry Measurements,
(2) Near Infrared Reflectance Measurements,
(3) Photoluminescence and Raman measurements.

6.1- Ellipsometry Measurement

6.1.1- Evaluation Of Ellipsometric Angles And Graphical Representation

The first problem to be addressed is how ψ and Δ are used to determine the sample's optical constants. From the experimental set-up for the ellipsometer discussed in the previous chapter, the experimental ellipsometric angle ψ_e and Δ_e, can be obtained from equations 3.32 and 3.35 [16]. Consider a single interface (air-solid absorbing substrate) with $(n-ik)$ the complex refractive index of the second absorbing medium, where n and k has the usual meaning. Using Fresnel's equations, it can be shown that [20,21]

$$n^2 - k^2 = sin^2(\phi)\left[1 + \frac{tan^2(\phi)[cos^2(2\psi) - sin^2(2\psi)sin^2(\Delta)]}{[1 + sin(2\psi)cos(\Delta)]^2}\right], \qquad \textbf{6.1}$$

$$2nk = \frac{sin^2(\phi)tan^2(\phi)sin(4\psi)sin(\Delta)}{[1 + sin(2\psi)cos(\Delta)]^2} \qquad \textbf{6.2}$$

Substituting the experimental ellipsometric angles ψ_e and Δ_e obtained into the above equations, one can determine the optical constants n and k for a single interface system. However in this experiment a doping superlattice, which is a multi-layer stack of n and p doped GaAs grown on a semi-insulating GaAs substrate plus the naturally existing oxide layer on top of the DSL is used. However the thickness of individual superlattice layer is much less than a wavelength of the incident laser beam. One can therefore treat the whole superlattice stack as a single layer by using an effective medium approach [22]. Therefore the samples are considered as an air-thin film (oxide layer)-substrate (DSL) system. For this system the equations become much more complicated because they are dependent on the refractive indices, the film thickness, the angle of incidence, and the wavelength. Hence a computer technique that shows the graphical representation of the dependence of ψ and Δ on the properties of the sample is used. This is done as follows:

The Fresnel's complex reflection coefficients, r_p and r_s, can be calculated using a matrix formalism of thin-film reflection [16] (pp333-340) and by estimating the unknown optical constants. This allows one to calculate the theoretical values for the ellipsometric angles, ψ_t and Δ_t. The estimates are then improved until a best match (on the graphic representation), according to a least squares method, is obtained between the theoretical (ψ_t and Δ_t) and experimental (ψ_e and Δ_e) ellipsometer angles. These estimates then give the optical constant values. Table 6.1b shows the optical constants obtained for the samples used in this experiment. The graphical representations for all probe beams used are shown below.

Figures 6.1a to 6.1c show ellipsometric angle versus angle of incidence for a bulk GaAs sample for three different probe beams.

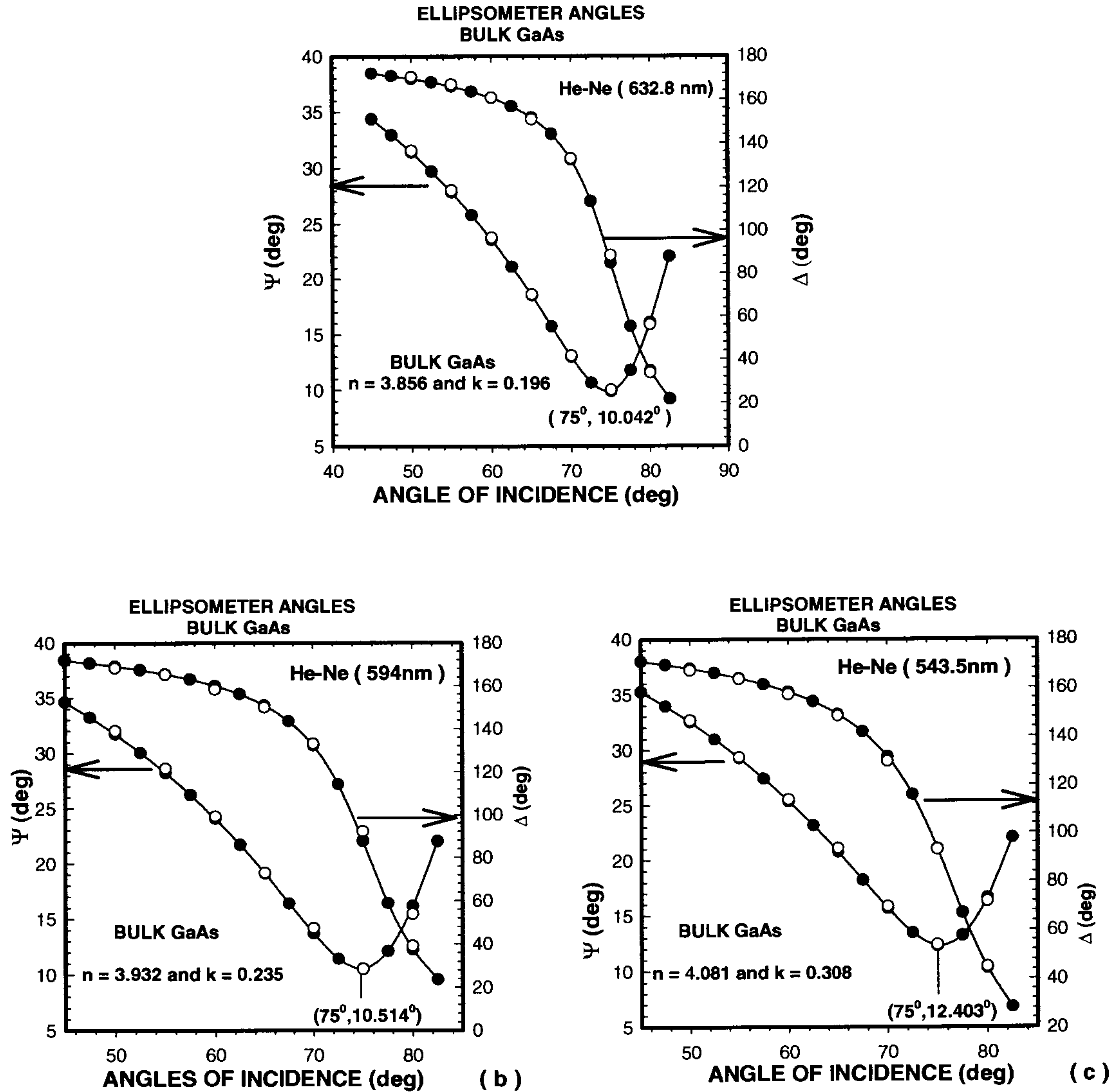

Figure 6.1. A best fit of model parameters to the experimental ellipsometric angles for bulk GaAs with a He-Ne laser beam at 632.8 nm (a) 594nm (b) and 543.5nm (c).

He-Ne (nm)	BULK	DSLH12	DSLH14	DSLV	DSLH16
Red (632.8)	-11.6	-22.0	-21.7	-19.9	-16.2
Yellow (594)	-11.1	-19.6	-18.9	-18.1	-14.3
Green(543.5)	-9.8	-17.9	-16.7	-16.1	-13.1

***Table 6.1a** shows slope of the Δ curves around $\Delta = 90^0$ for figures 6.1, 6.2 and 6.4.*

Figures 6.2a to 6.2d show ellipsometric angles versus angle of incidence for virgin and hydrogen implanted DSL's. A He-Ne laser at 632.8 nm is used as a probe beam.

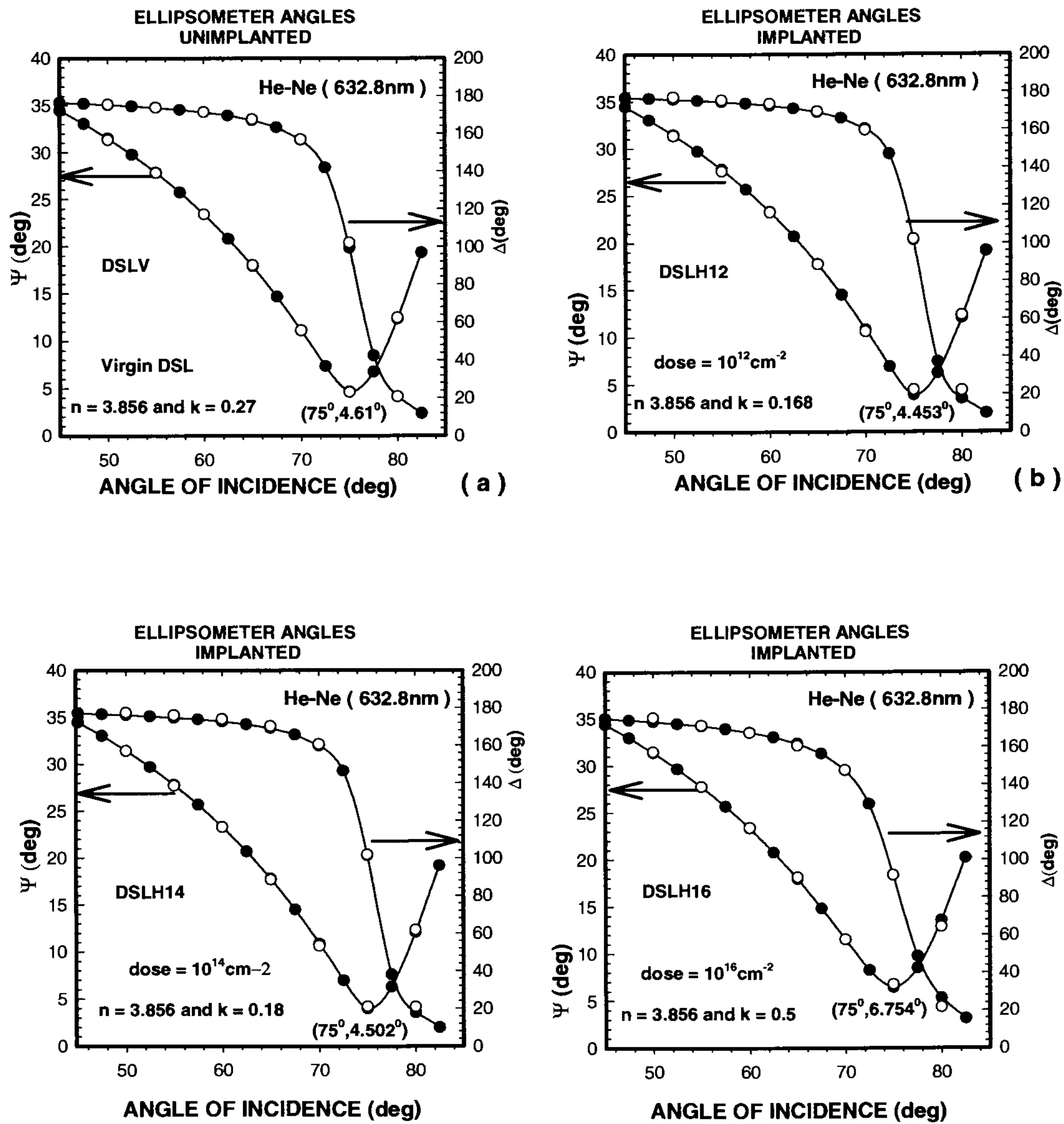

Figures 6.2(a to d) show a best fit of model parameters to the experimental ellipsometric angles for an unimplanted (virgin) GaAs doping superlattice sample (a) and for hydrogen implanted GaAs DSL samples with implantation doses 10^{12} cm^{-2} (DSLH12) (b), 10^{14} cm^{-2} (DSLH14) (c) and 10^{16} cm^{-2} (DSLH16) (d).

Figures 6.3a to 6.3d show ellipsometric angles versus angle of incidence for virgin and hydrogen implanted DSL's. A He-Ne laser at 594 nm is used as a probe beam.

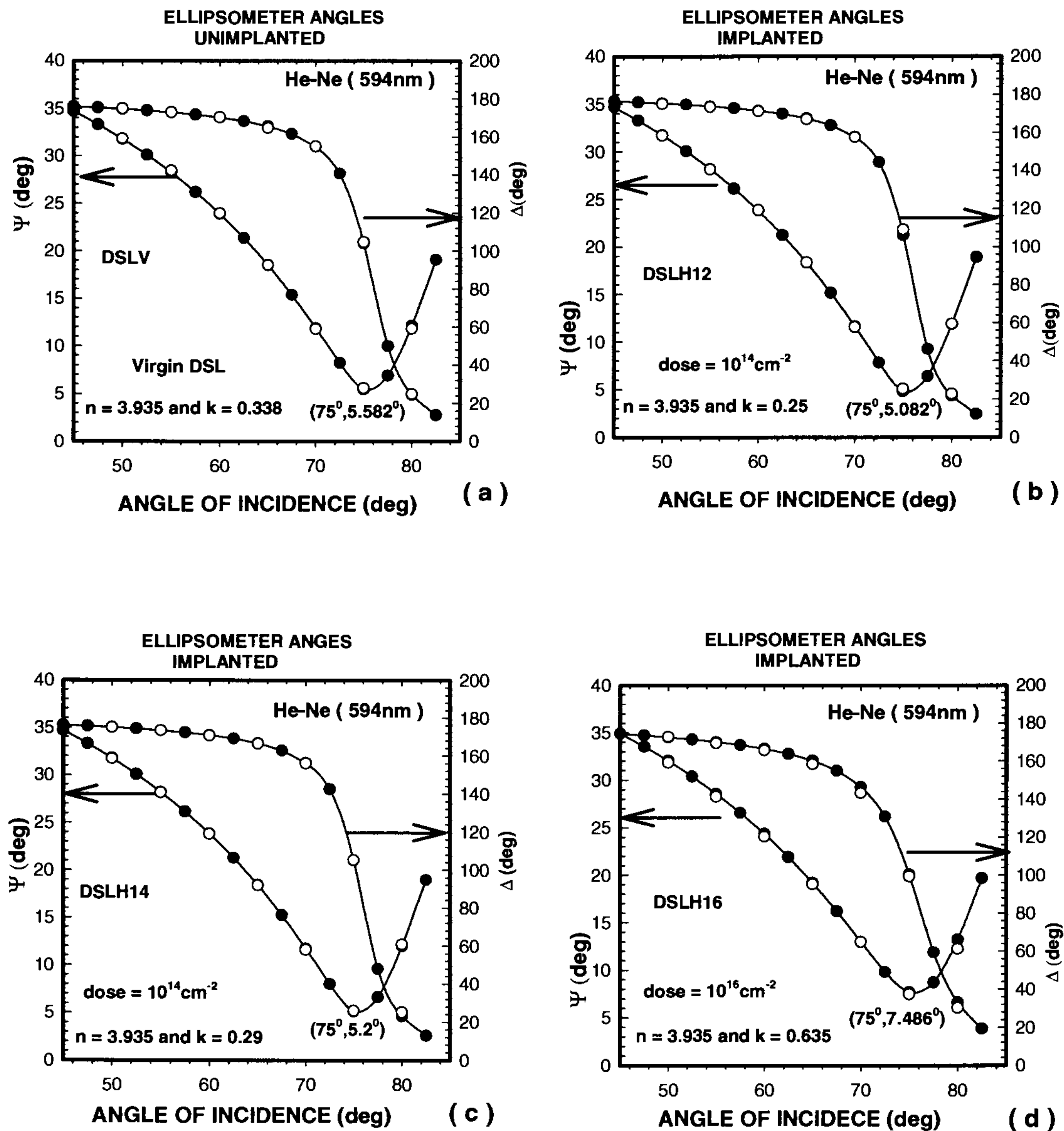

Figures 6.3(a to d) show a best fit of model parameters to the experimental ellipsometric angles for an unimplanted (virgin) GaAs doping superlattice sample (a) and for hydrogen implanted GaAs DSL samples with implantation doses 10^{12} cm^{-2} (DSLH12) (b), 10^{14} cm^{-2} (DSLH14) (c) and 10^{16} cm^{-2} (DSLH16) (d).

Figures 6.4a to 6.4d show ellipsometric angles versus angle of incidence for virgin and hydrogen implanted DSL's. A He-Ne laser at 543.5 nm is used as a probe beam.

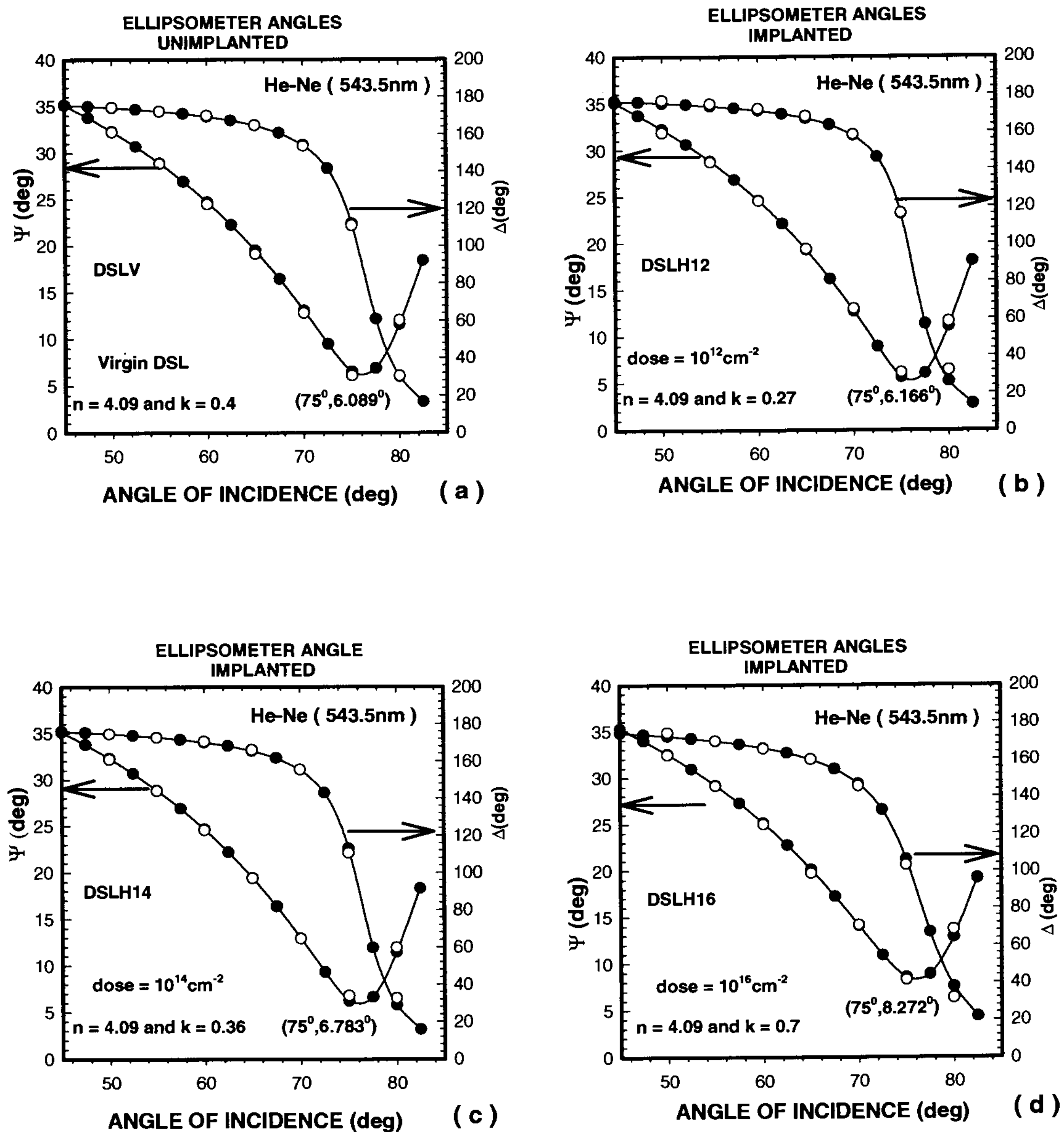

Figures 6.4(a to d) show a best fit of model parameters to the experimental ellipsometric angles for an unimplanted (virgin) GaAs doping superlattice sample (a) and for hydrogen implanted GaAs DSL samples with implantation doses 10^{12} cm^{-2} (DSLH12) (b), 10^{14} cm^{-2} (DSLH14) (c) and 10^{16} cm^{-2} (DSLH16) (d).

6.1.2- Graphical Comparison Of Extinction Coefficient Values

For an absorbing material such as a semiconductor (DSL) the reflectance $R_p = r_p^* \cdot r_p$ for p-polarized light does not reach zero as the angle of incidence is varied, but rather exhibits a minimum whose value depends on the extinction coefficient k. The ellipsometric angle ψ is a function of R_p, and it exhibits a minimum value around this point. Figures 6.1, 6.2, 6.3 and 6.4 all show the minimum values of ψ. Figures 6.2, 6.3 and 6.4 confirm that a GaAs DSL (virgin or implanted) with lower extinction coefficient has a lower value of ψ. The same characteristic feature of ψ as a function of extinction coefficient is shown in figure 6.1 for a bulk GaAs. The angle of incidence at which R_p is minimum is called the pseudo-Brewster angle. Another important angle of incidence is the principal angle at which the difference Δ between the phase-shifts δ_p and δ_s (3.35) experienced by s- and p- polarization upon reflection is 90^0. The difference between the pseudo-Brewster angle and the principal angle is usually small (less than 1^0 in the visible) and tends to zero as the extinction coefficient k approaches zero [16]. In contrast to transparent materials, absorbing materials (semiconductors) show a gradual change in Δ around the principal angle. The smaller the value of the extinction coefficient k, the more sharp the change in Δ (higher slope) around the principal angle. This characteristic feature is observed in this experiment if one compares the slope around the principal angle for each and every graphical representation in figures 6.1, 6.2, 6.3 and 6.4 (table 6.1a). The slopes of the Δ curve for angles of incidence θ where $70^0 < \theta < 80^0$, that is around the principal angle are tabulated in table 6.1a for the figures 6.1 to 6.4.

6.1.3- Optical Constant

In estimating the optical constants of the DSL the refractive index of the naturally existing thin transparent oxide layer was assumed to be 1.64. The thickness of this layer was also assumed somewhere between 2 and 6 nm [23]. Good model fits

were obtained for all samples at all wavelengths for a thickness of 4nm, which is consistent with the work of D.J. Brink et al [9]. Laser power were reduced to below 0.1mW (intensity $\approx 10^3 Wm^{-2}$) until a consistent, i.e. power independent, set of ellipsometric angles, ψ and Δ, were obtained. We assumed that the superlattice was essentially unexcited at these power levels. This intensity is somewhat lower than photo luminescence work [24] performed at intensity levels of around $2 \times 10^4 Wm^{-2}$, which resulted in a very low excitation level of a similar superlattice. The only remaining unknown quantity is then the complex index of refraction for the superlattice, treated as a single effective medium. A summary of best-fit parameter values is provided in table 6.1b.

GaAs Sample	Red 632.8nm		Yellow 549.0nm		Green 543.5nm	
	n	k	n	k	n	k
Bulk	3.856	0.196	3.932	0.235	4.081	0.308
DSLV	3.86	0.27	3.93	0.34	4.09	0.40
DSLH12	3.86	0.17	3.93	0.25	4.09	0.27
DSLH14	3.86	0.18	3.93	0.29	4.09	0.36
DSLH16	3.86	0.50	3.93	0.64	4.09	0.70

Table 6.1b. *Optical constants n (real refractive index) and k (extinction coefficient) determined by ellipsometry for bulk, virgin and ion implanted superlattices. Implantation doses are $10^{12} cm^{-2}$ (DSLH12), $10^{14} cm^{-2}$ (DSLH14) and $10^{16} cm^{-2}$ (DSLH16).*

As expected in a normally dispersive medium, both n and k increased slightly towards shorter wavelengths. That is, the wavelength of the probe laser is inversely proportional to the extinction coefficient of the material [25]. This is also consistent with the SEO model as the probe wavelengths are still well below the energy position, E_p, of the single oscillator model. For a superlattice the effective band gap is lower and therefore the photon energies for the three probe laser wavelengths are further

beyond the absorption edge than in a bulk material and hence a larger k value can be expected. As shown in table 6.1b, this was actually observed as k changed from 0.196 (bulk) to 0.27 (DSL). For the other two probe wavelengths at 594 and 543.5 nm, k changed from 0.24 to 0.34 and from 0.31 to 0.40 respectively. Within the accuracy of our experiment and in line with earlier observations [9] the real refractive index (above the band gap) for a DSL remains approximately the same as for bulk material.

As expected, ion-implantation results in optical changes. These changes manifest themselves as a change in the index of refraction n and also in extinction coefficient, k. Several papers have shown that the extinction coefficient k is a more sensitive indicator of damage than the refractive index n [9,25]. Values obtained in our present work also prove this sensitivity on k rather than on n (table 6.1b). The extinction coefficient k, that is direct measure of the damage created by implantation, changes rather slowly for the low dosage samples ($10^{12}\,cm^{-2}$ to $10^{14}\,cm^{-2}$ in this work) and then increases sharply for the higher dose ($10^{16}\,cm^{-2}$), (refer table 6.1b). In the work of Q. Kim et al [25] they have shown that for a Mg-ion-implanted GaAs sample, both the refractive index and extinction coefficient increased with implantation dose. This is also consistent with this work (for only the extinction coefficient) if a comparison is made between the values of the three implanted samples, DSLH12, DSLH14 and DSLH16 (refer table 6.1b). However, for the range of doses investigated, n was nearly unaffected by implantation. Hydrogen-ion implantation initially lowered the value of k to something close to the bulk material value, presumably due to the formation of traps at defect sites. At a very high implantation dose, however, k increased again by almost a factor of two.

6.2- Near Infrared Reflectance Measurement

6.2.1- Reflectance Spectrum

Near-infrared room-temperature reflectance measurements were taken with the set up shown in figure 5.3b and the corresponding results are shown in figures 6.5a and 6.5b.

In figure 6.5a, two major differences are observed in the reflectance spectrum of bulk and virgin DSL. Firstly, the bulk sample shows a higher reflectance value for most of the wavelength range investigated, indicating that the superlattice stack behaves slightly differently even well below the effective band gap. Note that they have nearly equal values around 980nm. Secondly, the DSL spectrum shows some regular but weak oscillations (interference peak) at wavelengths longer than about 1300nm.The starting point of the oscillation should be an indication of the point where the DSL becomes transparent. This oscillation is due to a slight difference in refractive index, which produces multiple reflections (constructive/destructive interference) between the air-DSL and DSL-bulk interfaces. At around 1350nm the modulation is disrupted, presumably due to the presence of a strong absorption feature of water vapour, which could not be completely eliminated by flushing with dry nitrogen. Above the effective band gap the DSL is no longer transparent and the DSL bulk interface plays no role at all. One can consequently roughly estimate the position of the effective band gap by noting the wavelength where the oscillations start.

Figure 6.5b present reflectance spectra obtained at room temperature in the range 800nm to 1450 nm for hydrogen ion implanted DSL's at three different doses. The strong dependence of reflectance on the implantation dose is clearly shown in this figure. For the implantation dose of $10^{12}\,cm^{-2}$ and $10^{16}\,cm^{-2}$, the reflectance increases with increasing dose. However the situation for the sample (DSL) implanted at a dose of $10^{14}\,cm^{-2}$ is quite different. The reflectance of this sample between 800 nm and ~980 nm is higher than for both the virgin GaAs DSL and bulk GaAs. It is lower than both bulk and virgin DSL in wavelength range of ~980 nm to ~1120 nm and finally has nearly the same values as the bulk as one goes to the longer wavelength side while it is higher than the virgin DSL. Generally speaking the reflectance spectrum for the DSL at $10^{14}\,cm^{-2}$ roughly resembles that of bulk GaAs at longer wavelengths, as is also shown in the calculations of constant parameters in the SEO model (next section). Note that all spectra exhibit some interference modulation at wavelengths beyond 1300 nm.

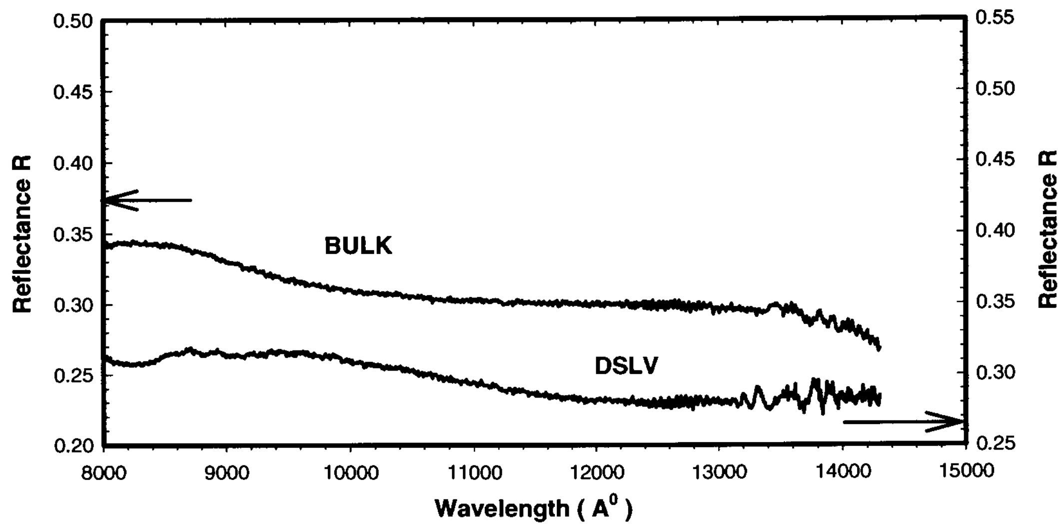

Figure 6.5a shows the near infrared room temperature reflectance spectra for bulk GaAs (Top and left hand axis) and for a virgin doping superlattice (Bottom and right hand axis).

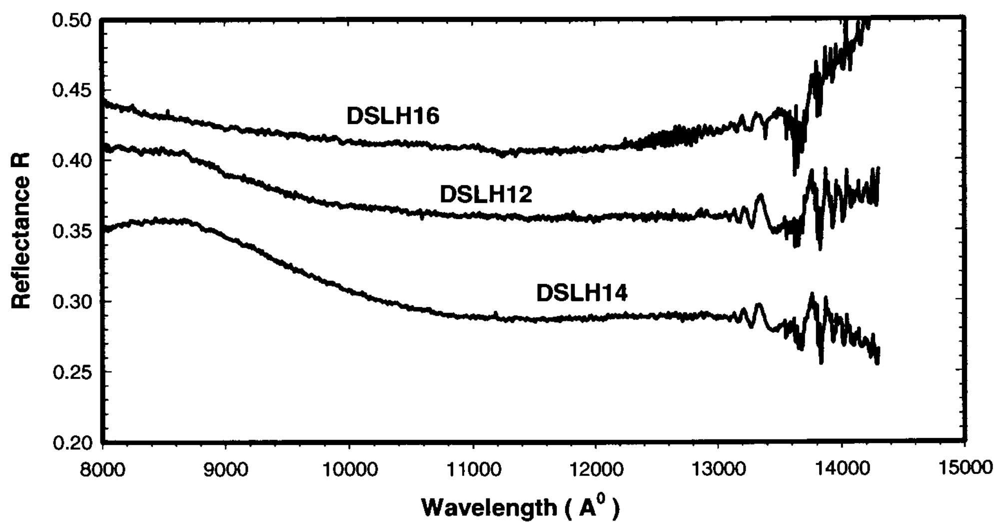

Figure 6.5b shows the near infrared room temperature reflectance spectra for hydrogen ion-implanted GaAs doping superlattices. The implantation doses are 10^{12} cm^{-2} *(DSLH12) middle,* 10^{14} cm^{-2} *(DSLH14) bottom and* 10^{16} cm^{-2} *(DSLH16) top curves.*

6.2.2- Evaluation Of The Real Refractive Index

As already stated before, the oscillations in the reflectance spectra are due to a low refractive index contrast at the DSL-bulk interface. As the amplitude of these oscillations is quite low compared to the average reflectance, one can, to a good first approximation, ignore the DSL-bulk interface by simply extrapolating a smooth curve through the oscillations. This approximation changes the system from a double interface (air-DSL-bulk) to a single interface (air-DSL) and hence allows the application of equation 2.6b [$n = \frac{(1+\sqrt{R})}{(1-\sqrt{R})}$] for the evaluation of the effective refractive index of the superlattice. Note that a p-type reflectance is always lower than for an s-type for angles of incidence other than zero and 90. They are equal at these angles. In this experiment the angle of incidence was nearly zero (normal incident) hence the formulas for either the parallel (R_p) or the vertical (R_s) reflectance components can be used as R in equation 2.6b. R here is the measured reflectance value. Applying equation 2.6b to the spectra in figures 6.5a and 6.5b allows the determination of the index of refraction and therefore also the inverse of susceptibility, $\chi^{-1} = (n^2 - 1)^{-1}$, enabling one to construct an experimental plot according to equation 2.10b given below

$$\frac{1}{\chi(E)} = \frac{1}{n(E)^2 - 1} = \frac{E_p}{E_d} - \frac{1}{E_p E_d} E^2 .$$

Plots of the inverse of susceptibility, $\chi^{-1} = (n^2 - 1)^{-1}$, versus square of photon energy E^2 are shown in figure 6.6a for bulk GaAs and a virgin DSL, where the dashed lines in the figures are defined by equation 2.10b and are the best single-effective-oscillator (SEO) fit to the data in the low energy range, as this model works well in this region.

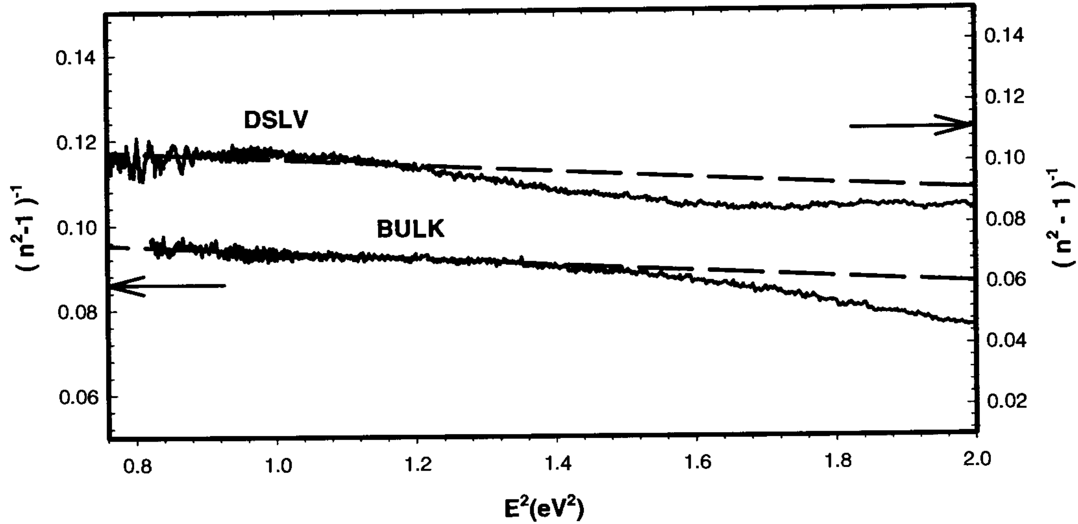

Figure 6.6a plot of inverse susceptibility $\chi^{-1} = (n^2 - 1)^{-1}$ *versus photon energy squared (* E^2 *) for bulk GaAs (bottom and left hand axis) and for a virgin doping superlattice (DSLV), top and right hand axis. Dashed lines are the best single-effective-oscillator fit to the data.*

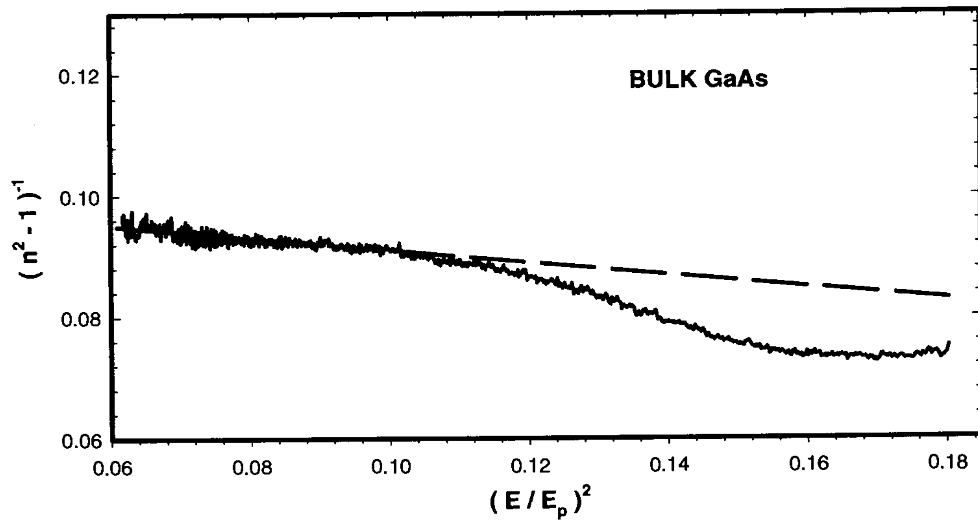

Figure 6.6b Plots of inverse susceptibility $\chi^{-1} = (n^2 - 1)^{-1}$ *versus* $(E/E_p)^2$ *for bulk GaAs, where E is the photon energy and* E_p *is the energy position parameter in the single-effective-oscillator model. Dashed lines are the best single-effective-oscillator fit to the data.*

For the bulk material a good fit is obtained for photon energies below 1.2 eV (~1.4 eV^2 on the figure), but between this point and the room temperature band gap at 1.42 eV (2 eV^2 on the figure) a considerable deviation is observed. This is exactly in accordance with the work of Afromowitz [5]. For an easy comparison between this work and that of Afromowitz inverse of susceptibility $(n^2-1)^{-1}$ versus $(E/E_p)^2$ is plotted in figure 6.6b for a bulk sample.

The negative curvature deviation observed at short wavelengths is due to the proximity of the band edge and the excitonic absorption. The largest deviation occurs when strong excitation peaks are present below the interband edge [4]. This emphasises the reason why the more advanced three-parameter model, which takes care of the effect of the near band gap, was developed. S.H. Wemple et al [4] and Afromowitz (for AlAs) [5,26] also obtained an exact fit of the SEO model to the reflection data without any deviation (not shown). At longer wavelengths, a positive curvature deviation from linearity is usually observed due to the negative contribution of the lattice vibrations to the refractive index [4]. The curve for the virgin DSL has roughly the same shape, but seems to be shifted as a whole to lower energies. This is due to the position of lowest effective energy band gap of the DSL. Unfortunately the curve is very noisy at lower energies as the limits of our detection arrangement is approached and the straight-line fit is not as good for the DSL as for the bulk material.

Since the best straight line fit in figures 6.6a is represented by equation 2.10b, the slopes and intercepts obtained should correspond to $-\dfrac{1}{E_pE_d}$ and $\dfrac{E_p}{E_d}$ respectively. And from this correspondence the two parameters of the SEO model, i.e. the dispersion energy E_d and the energy position E_p, are determined. The values are E_p=3.65 eV, E_d=36 eV for the bulk GaAs and E_p=3.27 eV, E_d=29 eV for a virgin DSL (table 6.2a). The dispersion and the energy position values for the bulk material agrees exactly to the result reported by Afromowitz [5] while slightly lower values

are obtained for a virgin DSL. This is reasonable as the effective band gap for a DSL is lower than that of the bulk material.

	Bulk	DSLV	DSLH12	DSLH14	DSLH16
Slope	-7.590E-3	-1.046E-2	-4.254E-3	-7.972E-3	-7.0722E-3
Intercept	1.0111E-1	1.1201E-1	7.1254E-2	1.0736E-1	6.1007E-2
E_P (eV)	3.65	3.27	4.09	3.67	2.937
E_d (eV)	36.098	29.22	57.43	34.18	48.143

Table 6.2a. *Single effective oscillator (SEO) parameters for bulk, virgin and ion implanted DSL's. Implantation doses are 10^{12} cm^{-2} (DSLH12), 10^{14} cm^{-2} (DSLH14) and 10^{16} cm^{-2} (DSLH16).*

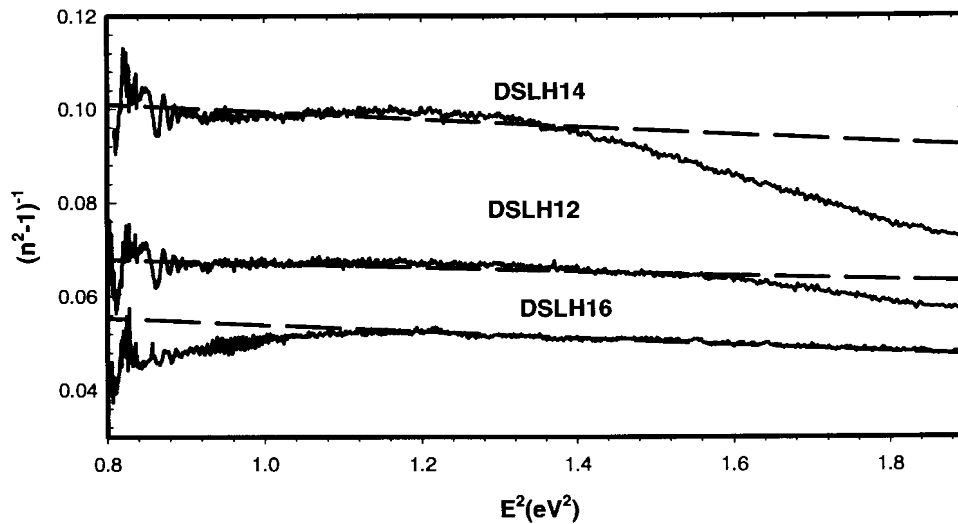

Figure 6.6c plot of inverse susceptibility $\chi^{-1} = (n^2 - 1)^{-1}$ versus photon energy squared (E^2) for hydrogen ion implanted GaAs doping superlattice. The implantation doses are 10^{12} cm^{-2} (DSLH12) middle, 10^{14} cm^{-2} (DSLH14) top and 10^{16} cm^{-2} (DSLH16) bottom curves.

The inverse susceptibility spectra for the ion-implanted samples are shown in figure 6.6c. The corresponding SEO parameters are summarized in table 6.2a. At an implantation dose of 10^{12} cm^{-2} the inverse susceptibility dropped and substantially modifies the parameter values to E_p = 4.09eV, E_d = 57 eV. This is not primarily due to a change in effective gap, but rather to some overall change in material properties combined with a partial destruction of the superlattice space charge potential due to the formation of traps at defect sites. Further implantation to a dose of 10^{14} cm^{-2} modifies the superlattice to something resembling the bulk material with E_p = 3.67eV, E_d = 34.18eV. Increasing the dose to 10^{16} cm^{-2} results in such severe lattice damage that a straight-line fit can no longer be made to the low-energy region (photon energy less than 1 eV) where the single oscillator model should fit well. Clearly the model is no longer valid. At photon energies beyond 1 eV a straight-line fit is possible giving values of E_p = 2.94 eV and E_d = 48 eV, but the validity is certainly questionable.

The other three unknown parameters in the Afromowitz model η, E_f and E_g were also determined in this experiment and are tabulated in table 6.3. These constants were evaluated in the following way. Firstly $\varepsilon_2(E) = 2nk$ is determined using the data's for real (n) and imaginary (k) parts of the refractive index obtained from the ellipsometer measurement (table 6.1b), well above the energy band gap but below E_f (~4 to 5 eV). From this and equation 2.15

$$\varepsilon_2(E) = \begin{cases} \eta E^4, & E_g \le E \le E_f \\ 0, & otherwise \end{cases},$$

the proportionality constant η was determined. The optical constants obtained from ellipsometer using 632.8 nm were used for the parameter calculation. This is because of a better fit to the $\varepsilon_2(E)$ spectrum at lower photon energy than at higher photon energy (figure 2.1b).

	Bulk	DSLV	DSLH12	DSLH14	DSLH16
E_f (eV)	4.968	4.469	5.636	5.00	-
E_g (eV)	1.400	1.188	1.303	1.395	Imaginary
η	0.10258	0.14138	0.08767	0.09421	0.26169

Table 6.2b. *Values for the Afromowitz parameters for bulk, virgin and ion implanted DSL's. Implantation doses are* $10^{12}\,cm^{-2}$ *(DSLH12),* $10^{14}\,cm^{-2}$ *(DSLH14) and* $10^{16}\,cm^{-2}$ *(DSLH16).*

As before values for the bulk material ($\eta = 0.103$, $E_f = 4.97\,eV$, $E_g = 1.40\,eV$) agrees well with the published values of Afromowitz [5] ($\eta = 0.102$, $E_f = 4.96\,eV$, $E_g = 1.42\,eV$). For the untreated DSL somewhat different parameter values ($\eta = 0.141$, $E_f = 4.47\,eV$, $E_g = 1.18\,eV$) are obtained. As expected the effective band gap is substantially lower than that of the bulk material, but it is still higher than the gap for a room temperature ground state superlattice (~0.963eV). It is therefore evident that even the low intensity light source used in this measurement produced some partial excitation of the superlattice caused by a partial neutralization of the space charge potential by photo carriers. According to equation 4.16, illumination dropped the space-charge potential to about half (0.27eV) of the ground state value (0.55eV). In spite of this the sample still behaves like a superlattice and can be used to study the influence of ion implantation.

As expected, ion implantation is a violent process in which energetic ions are forced into the target material. During their slowing down in the solid, large amounts of damage are inflicted on the sample until the implants come to rest. It is important to bear in mind that, unless the implantation-related damage is annealed out, a process that is accompanied by excessive diffusion (i.e., intermixing of layers), most measurable changes in the implanted layer are due to damage and not directly to the presence of the implanted species [19].

As shown in table 6.2b, implantation to a dose of 10^{12} cm^{-2} raised the effective gap to 1.3 eV and according to equation (4.16) reduces to space charge potential to 0.15 eV due to traps at defect sites. Increasing the dose to $10^{14}\ cm^{-2}$ moves the effective band gap to almost the bulk material value. At this point $2V_0$ is essentially zero due to a complete neutralization of the bare space charges. Further implantation (to 10^{16} cm^{-2}) mainly affects the material properties of the GaAs lattice itself as the DSL space charge potential is already neutralized. The Afromowitz model fails for this high dose sample as it produces an imaginary value for the effective band gap (table 6.2b).

If the parameter constants E_d, E_P, and E_g can be measured in a separate experiment, the real refractive index of a semiconductor (below the band gap) can be obtained by equation (2.22b), which was derived from the two and three parameter models.
The parameters E_d, E_P, and E_g are all obtained in this experiment and the real refractive index as a function of photon energy can therefore be calculated (equation 2.22b).

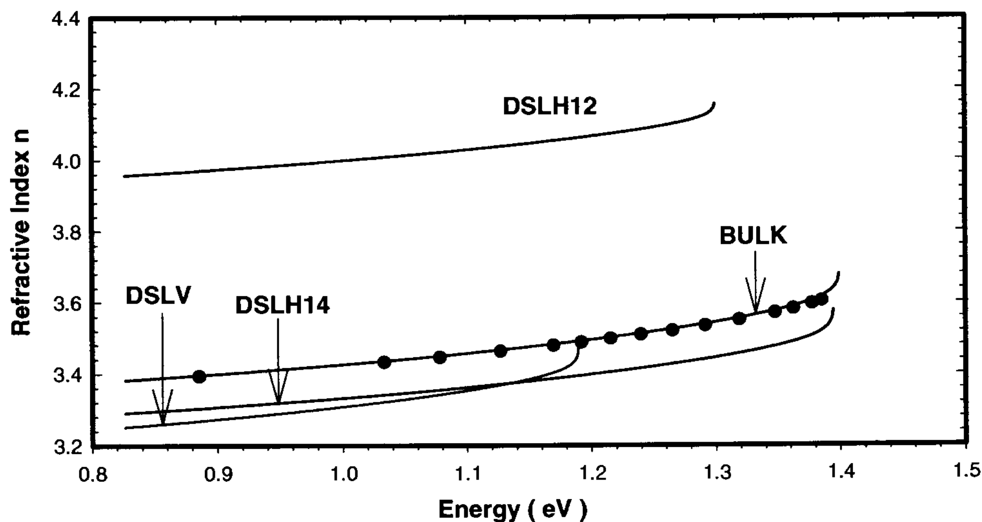

Figure 6.7a Plot of refractive index obtained using 2.22b versus photon energy for bulk, virgin DSL and hydrogen ion implanted GaAs doping superlattice. The implantation doses are 10^{12} cm^{-2} (DSLH12) and 10^{14} cm^{-2} (DSLH14). Closed circles are refractive index data for bulk GaAs taken from reference [27,28] for comparison.

Figure 6.7a shows the calculated refractive index value versus energy in a limited range for samples: bulk, DSLV, DSLH12 and DSLH14. In this figure a positive curvature at the right end of each curve is observed. This indicates that the material is no longer transparent above this point (it is an indication of the position of the direct lowest band gap).

6.3- Photoluminescence And Raman Measurements

Photoluminescence has become a very powerful tool in characterizing and detecting impurities and defects in semiconductors and DSL's [9,10,29]. A given impurity produces a set of characteristic spectral features that serves to identify it. In figures 6.8a and 6.8b photoluminescence spectra covering the range of 800 nm to 880 nm obtained from the virgin and implanted GaAs doping superlattices before and after annealing is displayed respectively at excitation intensity $15W / cm^2$ and 13 K sample temperature.

6.3.1a- Photoluminescence Measurement Before Annealing

Photoluminescence (PL) measurements were performed mainly to monitor implantation damage and the recovery of the superlattice opto-electrical structure after thermal annealing. The intensity of PL is very sensitive to the presence of lattice defects as these usually provide an alternative, non-radiative, recombination channel for optically generated electron-hole pairs [29]. As shown in figure 6.8a the untreated DSL exhibited a PL spectrum with a broad peak centred at 850 nm and a tail extending to past 880nm. This shift of effective energy gap from about 820nm for bulk GaAs to longer wavelengths is due to the spatial separation between the electrons in the n-layer and the holes in p-layer. Illuminating a DSL at a moderate intensity shifts the effective band gap back towards that of the bulk material. This can be explained in the following way:

When light of intensity around $15W / cm^2$ is incident on a DSL's two-dimensional carrier concentration, electrons and holes are generated. The (negative) electron space charge compensates the (positive) donor space charge in the n-layer and the hole space charge does the opposite in the p-layer [1]. The modulation of the band edges is thus reduced and the effective band gap of the DSL is shifted to a higher value and finally approaches that of the gap of bulk material as the excitation intensity is increased.

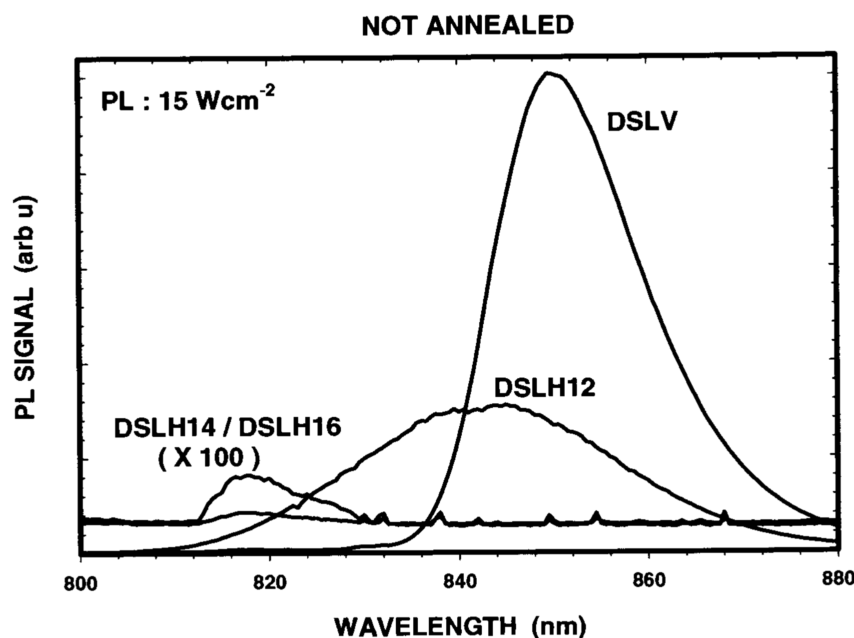

Figure 6.8a shows photoluminescence spectra of virgin (DSLV) and ion-implanted DSL's. The implantation doses are $10^{12}\,cm^{-2}$ *(DSLH12),* $10^{14}\,cm^{-2}$ *(DSLH14) and* $10^{16}\,cm^{-2}$ *(DSLH16). The PL signals for DSLH12 and DSLH14 are magnified* $(\times 100)$.

As observed with ellipsometry and IR reflectance, ion implantation gradually shifts the effective band gap and therefore also the PL peak towards shorter wavelengths. For an implantation dose of $10^{14}\,cm^{-2}$ the PL peak reached the band edge position for bulk GaAs, but it was considerably reduced in intensity and smeared out due to the presence of a high density of lattice defects. The similarity in peak position of the PL

spectrum of this sample (DSLH14) with bulk GaAs is expected, since nearly the same energy gap values for DSLH14 (1.39eV) and bulk (1.4eV) were obtained from ellipsometry and the room temperature near IR reflectance measurement. At a higher implantation dose ($10^{16}\,cm^{-2}$) no further shift in peak position was observed, but the PL intensity dropped even lower. This is expected as implantation increases since more non-radiative recombination channels are induced, which considerably reduce the PL intensity. Note that at very low excitation intensities, a PL signal could only be detected for a virgin DSL's (not shown).

The effect of ion implantation on the variation of the space charge potential depth and therefore on the shift of the effective band gap of the DSL's can be explained in terms of the pumping factor r [17] (4.30c),

$$r = \frac{n^{(2)}}{n_D d_n}.$$

Where $n^{(2)}$ is the injected two-dimensional carrier density (injected optically or electrically). The varying space charge associated with a variable electron ($n^{(2)}$) and hole ($p^{(2)}$) concentration induced a strong change in the effective energy gap E_g^{eff}, which is always smaller than the band gap of the unmodulated semiconductor material, E_g^0. For a compensated doping superlattice $N = 0$ (refer equation 4.31), the pumping factor r changes from nearly zero up to 1 for high excitation [17]. As the value of r increases, the space charge potential depth (4.34) decreases thereby increasing the effective band gap. At r = 1 the space charge potential become zero and the DSL's behave like bulk material. In this experimental work, a compensated DSL's was used, and hence the value of r is nearly zero at a ground state [17]. Which results in reducing equation 4.34

$$2\Delta V = \frac{e^2 n_D d_n^2}{4\varepsilon_0 \varepsilon_R}[1-r]^2 \ ,$$

to a ground state space charge modulation depth (equation 4.29b)

$$2\Delta V = \frac{e^2 n_D d_n^2}{4\varepsilon_0 \varepsilon_R} \ .$$

Photoluminescence measurement, figure 6.8a, shows the shift in effective band gap from the ground state value (~1279nm) to the energy (~880nm) value shown in the spectra for the virgin DSL's. This is because the intensity of the excitation laser ($15 Wcm^{-2}$) generates electrons and holes thereby increasing the two dimensional carrier densities. This results in changing the value of the pumping factor from nearly zero to some value between zero and 1 say r_{virgin}. However, ion implanted samples possess a higher effective pumping factor ($r_{imp} > r_{virgin}$), as can be expected from equation 4.34 and from the effective band gap shift obtained in the PL measurement (figure6.8a). This is presumably due to the introduction of traps at defect centres in doped layers by the ion implantation, which possibly results in: (1) preventing the out diffusion of optically injected (generated) carriers, (2) enhancing the electron hole recombination life time and hence allowing the generated carriers to neutralize the space charge impurities, which in turn reduce the modulation depth. In other words, reducing the effective concentration of ionized impurities given by $n_D^+ = n_D(1 - r_{virgin})$ to $n_D^+ = n_D(1 - r_{imp})$ [17], and hence reducing the modulation depth. The concluding remark, which can be made at this point, is that ion implantation introduces an effective pumping factor, which tunes the DSL's.

6.3.1b- Photoluminescence Measurement After Annealing

Figure 6.8b shows the photoluminescence spectra for ion implanted samples annealed at $500^0 C$ and $600^0 C$. After annealing at $500^0 C$ for two hours, the DSL implanted at $10^{12}\ cm^{-2}$ recovered almost completely as the PL peak closely matches that of the virgin DSL sample in shape, position and intensity (fig.6.8b DSLH12). Annealing the

DSL sample implanted at $10^{14}\,cm^{-2}$, however, showed only partial recovery (see figure 6.8b DSLH14a). An additional annealing step at $600^{o}\,C$ for another two hours moved the peak position to almost the right value (figure 6.8b DSLH14b), but the PL intensity still only recovered to about a third of the original value, indicating that a considerable defect density was still present. A similar behaviour was observed for the higher implantation dose sample (only shown for annealing at $600^{o}\,C$ for sample DSLH16b). It should be realized, however, that PL is a very sensitive measure of implantation damage.

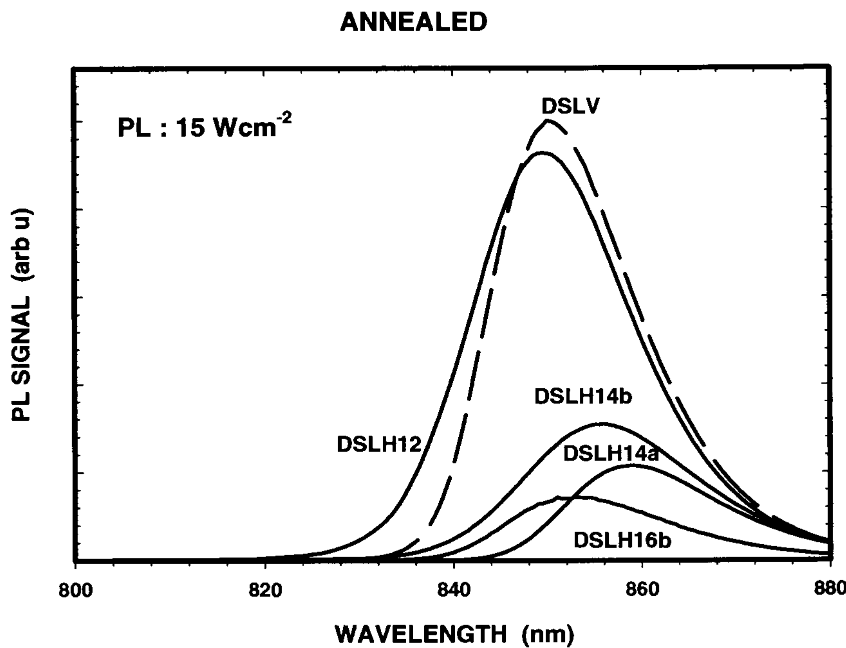

Figure 6.8b shows recovery of ion-implanted DSL's after thermal annealing according to photoluminescence measurements for ion-implanted DSL's. The implantation doses are $10^{12}\,cm^{-2}$ (DSLH12), $10^{14}\,cm^{-2}$ (DSLH14) and $10^{16}\,cm^{-2}$ (DSLH16). Curves (a) represent samples annealed at $500^{0}\,C$ and curves (b) are for samples annealed at $600^{0}\,C$.

6.3.2a- Normal Raman Measurement Before Annealing

Raman scattering can be used to determine the damage due to ion implantation and can monitor the effectiveness of annealing. Sharp phonon modes, which are characteristic of crystalline materials, change to broad peaks if the material becomes amorphous. As a crystalline material becomes amorphous, the intensity of the RS signal decreases [19]. In our present work, room temperature normal Raman spectra were recorded using a laser Ar^+ at 514 nm as excitation source in the backscattering geometry as shown in the figure 5.5. The Raman spectra obtained for the virgin and ion implanted samples are shown in figure 6.9a.

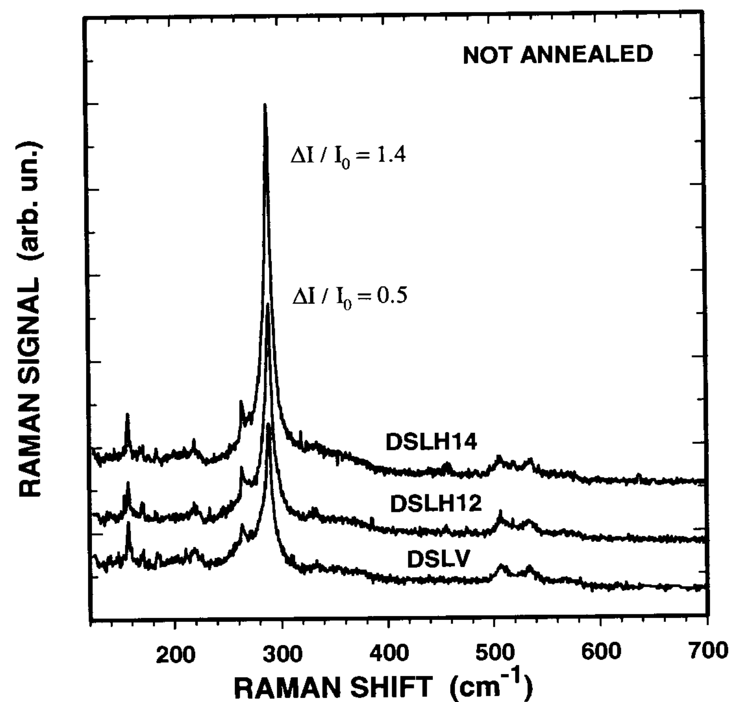

Figure 6.9a. Raman spectra of virgin and ion implanted doping superlattices excited by 514 nm laser light and recorded in the back scattering configuration. Change in the peak height of the LO line is indicated as $\Delta I / I_0$*, where* $\Delta I = I - I_0$ *and* I_0 *is the peak height for the virgin sample. An artificial baseline offset has been introduced to separate the spectra.*

In this figure, we compare three Raman spectra collected for not-annealed implanted samples, DSLH12 and DSLH14, and a virgin DSL (DSLV). The symbols I_0 and I denote the respective intensities of the sharp optical modes observed for virgin and implanted samples respectively and $\Delta I = I - I_0$. These Raman spectra represent the collective response of the whole GaAs lattice and are sensitive to lattice damage. In most semiconductors the LO-line (290 cm^{-1} for GaAs) broadens and drops in intensity as implantation dose is increased [30,31]. In this experimental work the opposite effect was observed. Notice the gradual increase of the sharp LO- phonon mode with increasing implantation dose in figure 6.9a. This can be understood if it is born in mind that the DSL's are heavily doped ($10^{18}\,cm^{-3}$) and that free carriers cause a plasmon to LO coupling, which drops its peak height. As implantation damage reduces the free carrier density one can therefore expect a more prominent LO peak as long as the material is not substantially amorphised by the implantation.

6.3.2b- Normal Raman Measurement After Annealing

As shown in figure 6.9b samples implanted at $10^{12}\,cm^{-2}$ (DSLH12) and $10^{14}\,cm^{-2}$ (DSLH14) and annealed at $500^0 C$ recovered almost completely as far as their Raman spectra are concerned. The sample implanted at $10^{16}\,cm^{\ 2}$ (not shown) exhibits only partial recovery after annealing at $500^0 C$ and $600^0 C$ in the sense that the TO Raman peak, which is symmetry forbidden in the backscatter configuration by selection rules, became quite prominent and the LO mode was lower than for the virgin sample. This effect is attributed to the disordering of the crystalline structure. A similar effect was observed in the work of S.G. Kim et al work [32]. S.G. Kim et al investigated the damage induced and its recovery after annealing for GaSb implanted with Ga. They have shown that with increasing dose, the LO phonon becomes weaker while the TO mode becomes stronger.

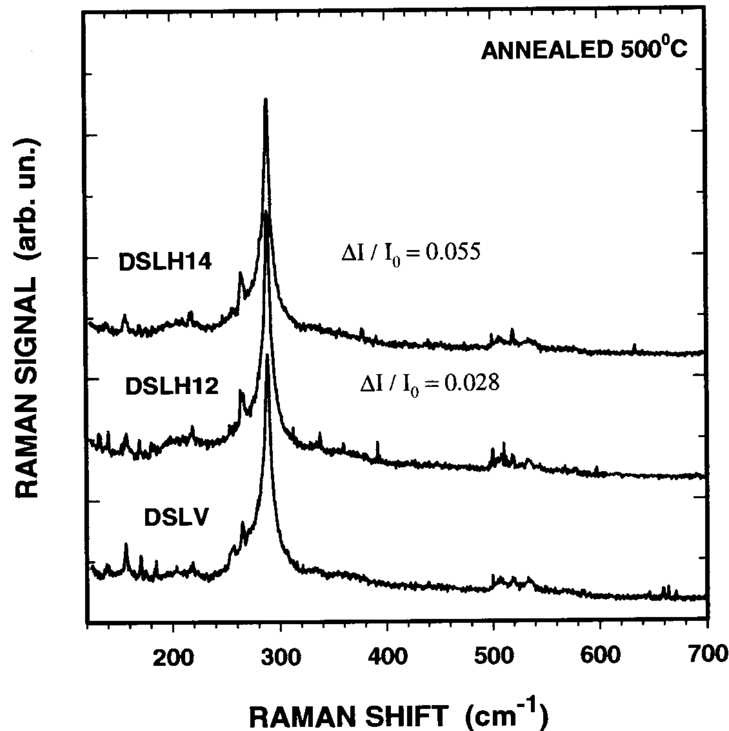

Figure 6.9b shows the Raman spectra for 514 nm laser excitation after thermal annealing at 500^0. *As in figure 6.9a differences in peak height for the LO Raman line are indicated as* $\Delta I / I_0$. *An artificial baseline offset has been introduced to separate the spectra.*

6.3.2c- Resonance Raman Measurement

In resonant Raman work the final result of the process is to transfer an electron from the μ_l to the μ_h (l < h) state in the quantum well of the conduction band. For these measurements there are selection rules (not studied in this work) that distinguish between single particle and collective excitation spectra. These can be separated by varying the polarization of the incoming and outgoing light. The single particle spectrum consists of transitions between the energy levels in the conduction band quantum well.

In general, the intensity of these spectra is very weak and it can only be observed by doing resonance Raman spectroscopy; that is, the exciting laser line must be close to a strong, real interband (conduction to valence band) excitation [24,33,34]. In our present work, the laser line wavelength was chosen to correspond to the k = 0 (k is the wave vector) split-off valence band to conduction band transition at about ~1.96eV (633 nm). As this resonant scattering process is specifically related to the modulation potential in a doping superlative (GaAs) structure, it is useful to monitor its destruction by ion implantation and its recovery after thermal annealing.

The bare single-particle intersubband excitation energies are measured by the spin-flip scattering signal, which is polarized, perpendicular to the exciting beam. In this experiment the scattering signal is observed at 90^0 to the exciting beam and is vertically polarized (Z) while the exciting beam is horizontally polarized (X). This is denoted as Z(XZ)X scattering. Figure 6.10a and 6.10b show the single particle excitation for a virgin DSL and ion-implanted samples before and after annealing respectively. In the figures $\Delta = 1$ stands for all possible transitions between first-nearest subbands, $\Delta = 2$ between second and $\Delta = 3$ between third nearest. Three peaks indicated by $\Delta = 1$, $\Delta = 2$ and $\Delta = 3$ sitting on the top of the hot-band luminescence (spontaneous conduction to split-off band transitions) were clearly observed for the virgin DSL (figure 6.10a). For the ion implanted sample at $10^{12}\ cm^{-2}$ before annealing the peaks are generally diminished, particularly $\Delta = 2$ and $\Delta = 3$. As implantation increased to $10^{14}\ cm^{-2}$ peaks $\Delta = 2$ and $\Delta = 3$ were smeared out while a broad shifted and very low peak at $\Delta = 1$ still remained indicating that some superlattice behaviour still existed, but the sample implanted at $10^{16}\ cm^{-2}$ (not shown) did not produce any trace of the resonant peaks.

In the work of G.H. Dohler et al [24] they showed that the intersubband spacing $\varepsilon_{c,\mu+\Delta} - \varepsilon_{c,\mu}$ for $\Delta = 1$ and $\Delta = 2$ is much less sensitive to changes of the two-dimensional carrier concentration $n^{(2)}$, than the gap energies $\varepsilon_{c,\mu} - \varphi_p$ [24]. Our experimental results of PL and resonance RS also support this. In our work the traps

produced by ion implantation were the main source of the changes in $n^{(2)}$ when comparing virgin samples to implanted samples. This is reflected by a change in the pumping factor r. The effect on the carrier concentration dependent shape of the superlattice potential is a decrease of the subband spacing as a function of increasing subband population. The decrease of the subband energy difference $\varepsilon_{c,\mu} - \varepsilon_{c,\nu}$ ($\mu > \nu$) is a result of the flattening of the quantum well [1]. Therefore one can expect a peak shift in characteristic spectra as a result of decreased subband spacing.

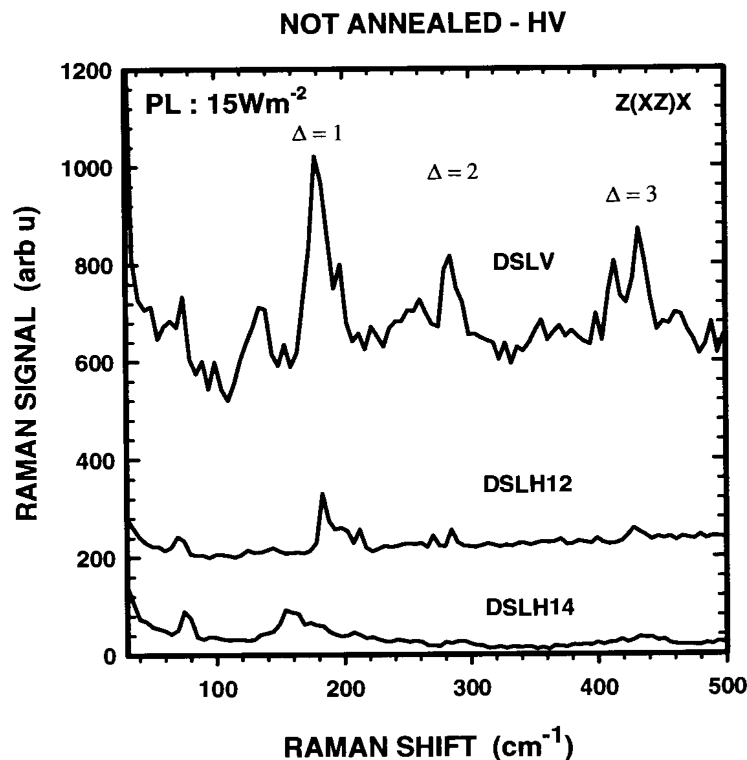

Figure 6.10a. Single particle resonant Raman spectra of ion implanted DSL's excited by 632.8 nm laser light in a Z(XZ)X 90^0 scattering configuration. The baseline offsets for the three curves are real. They are due to the hot-band luminescence caused by spontaneous conduction to split-off band transitions.

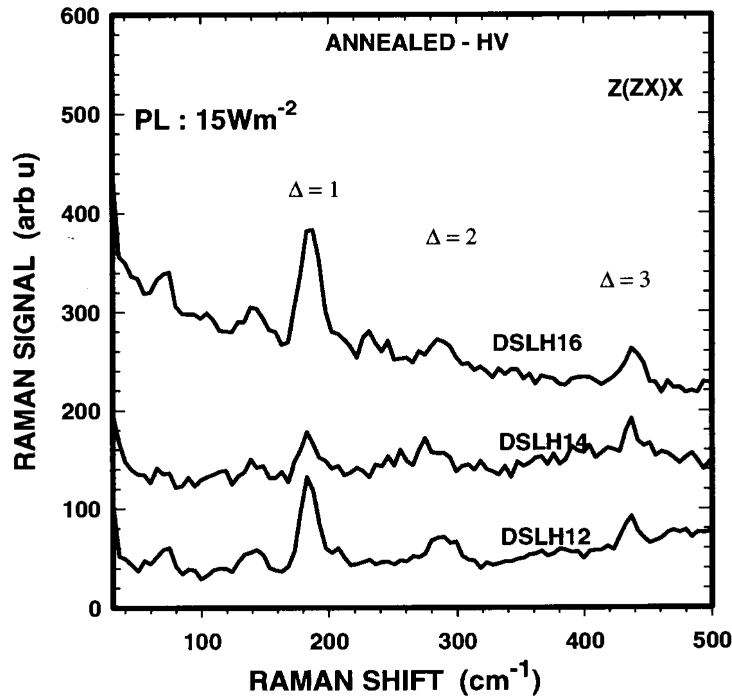

Figure 6.10b shows the recovery of ion-implanted DSL's after thermal annealing at $500^0 C$ according to single particle resonant scattering. An artificial baseline offset has been introduced to separate the spectra.

The resonance Raman scattering technique can show this energy shift. In our present work, a measurable peak shift is obtained for the sample implanted at $10^{14}\,cm^{-2}$ ($\sim 25\,cm^{-1}$) compared to that of the virgin DSL's (see figure 6.10a). The peak for the sample implanted at $10^{12}\,cm^{-2}$, DSLH12, remained at nearly the same position as that of the virgin DSL. However, from the PL measurement, a measurable shift in effective band gap $(\varepsilon_{c,\mu} - \varphi_p)$ towards a higher energy was observed for both samples, implanted at $10^{12}\,cm^{-2}$ and $10^{14}\,cm^{-2}$ (see figure 6.8a). This confirmed the higher sensitivity of the gap energy $\varepsilon_{c,\mu+\Delta} - \varphi_p$ to changes in $n^{(2)}$ compared to the intersubband spacing $\varepsilon_{c,\mu} - \varphi_p$ and therefore to the work of G.H. Döhler [24]. Recovery of the superlattice structure after annealing is summarized in figure 6.10b. Clearly all DSL's including the heavily implanted $10^{16}\,cm^{-2}$ sample, exhibited a fair degree of recovery. Note that the peak positions also recovered.

UNIVERSITEIT VAN PRETORIA
UNIVERSITY OF PRETORIA
YUNIBESITHI YA PRETORIA

CHAPTER 7

Conclusion..100

Suggestion For Future Work...101

CHAPTER 7

Conclusion

In this work, we have studied (1) the applicability of the two (SEO) and three parameter (Afromowitz) models, (2) the semi permanent tunability of the DSL's with energetic hydrogen ion-implantation and (3) the recovery process of these hydrogen ion implanted DSL's samples after normal thermal annealing. The DSL's were implanted at three different implantation doses $10^{12}\,cm^{-2}$ (DSLH12), $10^{14}\,cm^{-2}$ (DSLH14) and $10^{16}\,cm^{-2}$ (DSLH16). Single wavelength ellipsometry and near infrared reflectance measurements show that a GaAs DSL's can be modelled as a SEO well below the effective band gap and by the Afromowitz three-parameter model closer to the band gap. These techniques also prove the applicability of these models for DSL samples implanted with hydrogen up to a dose of $10^{14}\,cm^{-2}$, however when the dose reaches $10^{16}\,cm^{-2}$ both models break down.

It was found that the hydrogen ion implanted GaAs DSL samples exhibit different features from that of virgin DSL's. Ellipsometry confirms the changes in free carrier concentration with implantation dose, as it indicates a slight difference in extinction coefficient for the lower implantation samples (DSLH12 and DSLH14) and large variation for higher implantation dose sample (DSLH16) with respect to the virgin DSL's. PL measurements show an intensity drop and peak shift towards higher energy with increasing implantation dose. This is due to radiationless recombinations via defect centres and trapping of free carriers. Normal Raman spectroscopy showed an inverse relation between Raman peak height and ion- implantation due to plasmon to LO coupling. A measurable shift in subband spacing was also observed for the sample implanted at $10^{14}\,cm^{-2}$ with the resonance Raman scattering measurement.

Note that all results, including ellipsometry above the band gap, infrared reflectance recorded below the band gap as well as PL indicated that an implantation dose of $10^{14}\ cm^{-2}$ modified the optical response of the DSL's to something resembling the bulk material. In this way the optical constants as well as the effective band gap can be tuned semi-permanently to the bulk values.

Raman spectroscopy and PL showed that the implantation effects could be reversed to a substantial degree by a simple thermal annealing step. Damage caused by ion-implantation with small doses (DSLH12) was minor, and even at low-temperature annealing restored the samples back to their full crystalline structure.

Suggestion For Future Work

The near infrared reflectance measurements presented in this work suffered from two shortcomings. Firstly, the spectra were rather noisy, especially in the long-wavelength regions. This can be improved drastically by using a modified Fourier transform spectrometer. During the course of this work it could unfortunately not be done due to time and cost constraints.

A second limitation of the present work is the slight excitation of DSL's during measurements. This can in principle be avoided by placing the samples under investigation at the exit slit of the mononchromator, where they will be illuminated at a much lower intensity level by below-band gap radiation. Again time constraints prevented us from implementing this modification.

APPENDIX A

Mathematical derivations for some equations given in chapter two are given in this appendix. This section is divided into parts 1 and 2.

PART 1:

In one dimension, the delta function, written $\delta(x-a)$, is a mathematical improper function having the properties [35]:

(1) $\delta(x-a)=0$ for $x \neq a$, **1**

and

(2) $\int \delta(x-a)dx = 1$, **2**

if the region of integration includes $x = a$, and is zero otherwise.

From the definition above it is evident that, for an arbitrary function $f(x)$,

(3) $\int f(x)\delta(x-a)dx = f(a)$. **3**

The single oscillator model requires two parameters, oscillator energy position E_p and dispersion energy E_d, where the imaginary part of the dielectric constant $\varepsilon_2(E)$ of the material is assumed to be a delta function at E_p and the strength of an effective oscillator at energy E_p was defined to be $\frac{\pi E_d}{2}$. (Section 2.3.2 pp 11).

Writing the above statement mathematically as:

$$\varepsilon_2(E) = \begin{cases} \frac{\pi E_d}{2} & for \quad E = E_p \\ 0 & for \quad E \neq E_p \end{cases} . \qquad 4$$

Or writing this in terms of a delta function:

$$\varepsilon_2(E) = \delta(E)\frac{\pi E_d}{2} . \qquad 5$$

Introducing this quantities (5) into the following equation of the KK relation

$$\varepsilon_1(E') = 1 + \frac{2}{\pi}\int_0^\infty \frac{E\varepsilon_2(E)}{E^2 - E'^2} dE , \qquad 6$$

we obtain

$$= 1 + \frac{2}{\pi}\int_0^\infty \frac{E}{E^2 - E'^2}\delta(E)\frac{\pi E_d}{2} dE .$$

Taking out the constant from the integral as

$$= 1 + E_d \int_0^\infty \frac{E}{E^2 - E'^2}\delta(E) dE \qquad 7$$

and applying the delta property 3 to the above equation at energy $E = E_p$ we get:

$$\varepsilon_2(E) - 1 = n(E)^2 - 1 = \frac{E_p E_d}{E_p^2 - E^2} , \qquad 8$$

which is the single effective oscillator formula, equation 2.10a (Section 2.3.2 Pp 11). Note that the region of integration in equation 7 includes $E = E_p$ and the constant a is zero in this case.

PART 2:

A function given by:

$$f(x-a) = \sum_{n=0}^{\infty} C_n (x-a)^n , \tag{9}$$

is a power series with its interval of convergence centred at a, where a is any fixed number and n is the term order. In particular, if $f(x-a)$ possesses a derivative of all orders at a, then we call

$$f(x-a) = \sum_{n=0}^{\infty} \frac{f^n(a)(x-a)^n}{n!} , \tag{10}$$

the Taylor series of $f(x-a)$ about the number a.
Rewriting equation 2.11, chapter 2 pp 12

$$\varepsilon_1(E') - 1 = n(E')^2 - 1 = \chi(E') = \frac{2}{\pi} \int_{E_g}^{\infty} \frac{E\varepsilon_2(E)}{E^2 - E'^2} dE$$

as:

$$\chi(E') = \frac{2}{\pi} \int_{E_g}^{\infty} \varepsilon_2(E) \frac{1}{E} \left[\frac{1}{1 - \left(\frac{E'}{E} \right)^2} \right] dE \tag{11}$$

allowed a power series expansion.

For simplicity let us first consider the function $f(x)=\frac{1}{1-x}$. The power series expansion of this function using equation 9 is:

$$f(x)=\frac{1}{1-x}=1+x+x^2+x^3+\ldots \qquad \mathbf{12}$$

Similarly the power series expansion of $\frac{1}{1-\left(\frac{E'}{E}\right)^2}$ in equation 11 is given by:

$$f(x)=\frac{1}{1-x}=\frac{1}{1-\left(\frac{E'}{E}\right)^2}=1+\left(\frac{E'}{E}\right)^2+\left[\left(\frac{E'}{E}\right)^2\right]^2+\left[\left(\frac{E'}{E}\right)^2\right]^3+\ldots \qquad \mathbf{13}$$

Putting the above equation into 11 we get:

$$\chi(E')=\frac{2}{\pi}\int_{E_g}^{\infty}\varepsilon_2(E)\frac{1}{E}\left\{1+\left(\frac{E'}{E}\right)^2+\left(\frac{E'}{E}\right)^4+\left(\frac{E'}{E}\right)^6+\ldots\right\}dE$$

$$=\frac{2}{\pi}\int_{E_g}^{\infty}\varepsilon_2(E)\left\{\frac{1}{E}+\frac{E'^2}{E^3}+\frac{E'^4}{E^5}+\frac{E'^6}{E^7}+\ldots\right\}dE \qquad \mathbf{14}$$

which is equation 2.12 in chapter 2 page 12.

The imaginary part of the dielectric constant $\varepsilon_2(E)$ in the energy region defined by $E_g \le E \le E_f$ is given by the Afromowitz model as (2.15) [4],

$$\varepsilon_2(E)=\begin{cases}\eta E^4, & E_g\le E\le E_f \\ 0, & otherwise\end{cases}. \qquad \mathbf{15}$$

Substituting the above equation into equation 14 we get:

$$\chi(E') = \frac{2\eta}{\pi}\left\{\int_{E_g}^{E_f}\left[E^3 + EE'^2 + \frac{E'^4}{E} + \frac{E'^6}{E^3} + \ldots\right]dE\right\}. \quad \mathbf{16}$$

Integrating this results in:

$$\chi(E') = \frac{\eta}{2\pi}\left[E_f^4 - E_g^4\right] + \frac{\eta E'^2}{\pi}\left[E_f^2 - E_g^2\right] + \frac{2\eta E'^4}{\pi}\left[ln\, E_f - ln\, E_g\right] + \frac{\eta E'^6}{\pi}\left[\frac{1}{E_g^2} - \frac{1}{E_f^2}\right] + \frac{\eta E'^8}{2\pi}\left[\frac{1}{E_g^4} - \frac{1}{E_f^4}\right] + \ldots$$

$$= M_{-1} + M_{-3}E'^2 + \frac{\eta E'^4}{\pi}\left[\frac{ln\, E_f}{ln\, E_g}\right]^2 + \frac{\eta}{\pi}\left\{\frac{E'^6}{E_g^2} + \frac{E'^8}{2E_g^4} + \frac{E'^{10}}{3E_g^6} + \ldots\right\} - \frac{\eta}{\pi}\left\{\frac{E'^6}{E_f^2} + \frac{E'^8}{2E_f^4} + \frac{E'^{10}}{3E_f^6} + \ldots\right\}$$

$$= M_{-1} + M_{-3}E'^2 + \frac{\eta E'^4}{\pi}\left\{\left\{ln\, E_f^2 - \frac{E'^2}{E_f^2} - \frac{E'^4}{2E_f^4} - \frac{E'^6}{3E_f^6} + \ldots\right\} - \left\{ln\, E_g^2 - \frac{E'^2}{E_g^2} - \frac{E'^4}{2E_g^4} - \frac{E'^6}{3E_g^6} - \ldots\right\}\right\}$$

$$\chi(E') = M_{-1} + M_{-3}E'^2 + \frac{\eta E'^4}{\pi}\left\{\left\{f_1(E'^2)\right\} - \left\{f_2(E'^2)\right\}\right\} \quad \mathbf{17}$$

where
$$f_1(E'^2) = ln\, E_f^2 - \frac{E'^2}{E_f^2} - \frac{E'^4}{2E_f^4} - \frac{E'^6}{3E_f^6} - \ldots, \quad \mathbf{18}$$

and

$$f_2(E'^2) = ln\, E_g^2 - \frac{E'^2}{E_g^2} - \frac{E'^4}{2E_g^4} - \frac{E'^6}{3E_g^6} - \ldots. \quad \mathbf{19}$$

The functions $f_1(E'^2)$ and $f_2(E'^2)$ are a Taylor series expansion of $ln(E_f^2 - E^2)$ and $ln(E_g^2 - E^2)$ respectively. This can be proved by expanding the functions $ln(E_f^2 - E^2)$ and $ln(E_g^2 - E^2)$.

Note that the derivatives in the expansion should be taken with respect to E^2 and evaluated at $E^2 = 0$. Therefore one can write equation 17 as:

$$\chi(E') = M_{-1} + M_{-3}E'^2 + \frac{\eta E'^4}{\pi}\{\{ln(E_f^2 - E^2)\} - \{ln(E_g^2 - E^2).\}\}$$

$$= M_{-1} + M_{-3}E'^2 + \frac{\eta E'^4}{\pi} ln\left\{\frac{(E_f^2 - E^2)}{(E_g^2 - E^2)}\right\} \quad \mathbf{20}$$

Direct substitution of the following equations (see chapter 2 page 14-15)

$$M_{-1} = \frac{\eta}{2\pi}\left(E_f{}^4 - E^4{}_g\right) \quad \mathbf{21a}$$

$$M_{-3} = \frac{\eta}{\pi}\left(E_f{}^2 - E^2{}_g\right) \quad \mathbf{21b}$$

$$E_f = (2E_p{}^2 - E_g{}^2)^{\frac{1}{2}} \quad \mathbf{22c}$$

$$\eta = \frac{\pi E_d}{2E_p{}^3(E_p{}^2 - E_g{}^2)} \quad \mathbf{22d}$$

into equation 20 will results in (see chapter 2 pp16):

$$n(E)^2 - 1 = \frac{E_d}{E_p} + \frac{E_d E^2}{E_p{}^3} + \frac{\eta E^4}{\pi}\ln\{\frac{2E_p{}^2 - E_g{}^2 - E^2}{E_g{}^2 - E^2}\} \quad \mathbf{23}$$

APPENDIX B

In this section the introduction of the pumping factor r to the potential depth profile equation given by (Chapter 4 pp 46)

$$2\Delta V = v_O(\frac{d}{2}) - v_O(0) = (\frac{e^2}{\varepsilon_0 \varepsilon_R})[\frac{n_D(d_n^+)^2}{2} + \frac{n_A(d_P^-)^2}{2} + n_D d_n^+ d_i], \qquad \mathbf{1}$$

is shown.

The effective doped layer width in terms of the pumping factor r is given by equation 4.30,

$$2d_n^+ = d_n(1 - \frac{n^{(2)}}{n_D d_n}) = d_n(1-r), \qquad \mathbf{2a}$$

and

$$2d_p^- = d_p(1 - \frac{p^{(2)}}{n_A d_p}) = \frac{n_D d_n}{n_A}(1-r), \qquad \mathbf{2b}$$

where r is defined as

$$r = \frac{n^{(2)}}{n_D d_n} \ . \qquad \mathbf{2c}$$

Substituting the above equations: $d_n^+ = \frac{d_n}{2}(1-r)$ and $d_p^- = \frac{d_n n_D}{2n_A}(1-r)$

into equation 1, we get:

$$2\Delta V = \frac{e^2 n_D d_n}{4\varepsilon_0\varepsilon_R}\left\{\frac{d_n}{2}(1-r)^2 + \frac{d_n n_D}{2n_A}(1-r)^2 + 2d_i(1-r)\right\}, \qquad 3$$

$$= \frac{e^2 n_D d_n}{4\varepsilon_0\varepsilon_R}(1-r)\left\{\left(\frac{d_n}{2} + \frac{d_n n_D}{2n_A} + 2d_i\right) - r\left(\frac{d_n}{2} + \frac{n_D}{2n_A}\right)\right\},$$

$$= \frac{e^2 n_D d_n}{4\varepsilon_0\varepsilon_R}(1-r)\left(\frac{d_n(n_D+n_A)}{2n_A} + 2d_i\right)\left\{1 - \frac{r d_n(n_D+n_A)}{4d_i n_A + d_n(n_D+n_A)}\right\},$$

$$= \frac{e^2 n_D d_n}{4\varepsilon_0\varepsilon_R}(1-r)\left(\frac{d_n(n_D+n_A)}{2n_A} + 2d_i\right)\left\{1 - \frac{r}{1 + \dfrac{4d_i n_A}{d_n(n_D+n_A)}}\right\}. \qquad 4$$

which is the equation given in chapter 4 page 49.

REFERENCES:

1- K. Ploog and G.H. Döhler. Adv. Phys. **32,** 285 (1983).

2- P. Ruden and G.H. Döhler. Phys. Rev. B **27,** 3538 (1983).

3- G.H. Döhler, H. Kunzel, and K. Ploog. Phys. Rev. B **15** 2616 (1982)

4- S.H. Wemple and M. Didomenico. J. Phys. Rev. B **3**, 1338 (1971).

5- M. Afromowitz. Solid-State Com. **15**, 59 (1974).

6- Semiconductor Opto-electronucs. T.S Moss G.J. Burrell and B. Ellis. Butterworth & co (publishers), Australia, Canada, Newzealand, SouthAfrica.

7- S.H. Wemple, Physical Rev. B **7** 3767 (1973).

8- Manual on Ellipsometry. R. J. Archer. Gartner scientific corporation USA.

9- D.J. Brink, H.W. Kunert and R. Sieberhangen. J. App. Phys. **88** 2326 (2000).

10- H.W. Kunert, J.B. Malherbe, D.J. Brink. Applied surface science **135** 29-36 1998.

11- H.W. Kunert, J.B. Malherbe, D.J. Brink, R.Q. Odendaal, L.C. Prinsloo, J. Camassel, J. Allegre, K. Zeaiter, C. Llinares. Applied Surface Science **166** 77-81 2000.

12- GaAs and Related Materials. Bulk Semiconducting and Superlattice Properties. Sadao Adachi. Singapore; River Edge, NJ: World Scientific, c1994.

13- H.C. Casey Jr., D.D. Sell, and M.B. Panish. App. Phys. Lett. **24** 63 (1974).

14- Burn, Solid State Physics. Academic press, Inc. Harcourt Brace Jovanovich, publisher, Orlando San Diego, San Francisco New York, London, Toronto, Montreal, Sydney, Tokyo, Sao Paulo 1985

15- R. C. Eden, Stanford Electronics Laboratories, Stanford University, Report SEL-67-038 (1967).

16- R.M.A. Azzam and N.M. Bashara, Ellipsometry And Polarized Light. Elsevier science publisher B.V, The Netherlands 1977

17- D.V. Ushakov, V.K. Kononenko, and I.S. Manak Proceedings of the Sixth Annual Seminar NPCS'97.Stepanove Institute of physics, Belarusian University 1997.

18- The Art Of Electronics Second Editions. Paul Horowitz And Winfield Hill (Pp 997). Published by the press Syndicate of the University of Cambridge, New York, USA and Melborne, Australia 1980.

19- Effect Of Disorder And Defects In Ion-Implanted semiconductors Optical And Photothermal Characterization. R.K. Willardson and Eicke. R. Weber 1997. Academic press San Diego, London, Boston, New York, Sydney Tokyo, Toronto.

20- K. H. Zaininger and A. G. Revesz RCA Review B **27** 85 (1964).

21- Ronald K. Sampsom and Hisham, Z. Massoud. J. Electrochemistry. Soc **140** 2673 (1993).

22- P.J. Roussel, J. Vanhellemont and H.E. Maes. Thin Solid Film **234** 423-427 (1993).

23- Ohlidal and M. Libenzny. Surf.interface Anal. **17** 171 (1991).

24- G.H. Döhler, H. Kunzel, D. Olego, K. Ploog, P. Ruden, H.J. Stolz and G. Abstreiter, **47** 864 (1981).

25- Q. Kim and Y.S. Park. Surface Science, **96** 307-318 (1980).

26- R. E. Fern and Onton A., J. App. Phys. **42** 3499 (1971).

27- D. T. F Marple, J. App. Phys. **35** 1241 (1964).

28- Semiconductor and Semi-metals by Willardson R. K. and Beer Vol **3** Ac (Academic press, N.Y. (1967) page 513 ff.

29- H.W. Kunert and D.J. Brink. J. App. Phys. **81** 6948 (1997).

30- J. Camassel, S. Blanque, N. Mestres, P. Godignon, and J. Pascual. Phys. Stat. Sol.(c) **195** 875-880 (2003).

31- Hesse, J. F. and Compaan. J. App. Phys. **50**, 206-213 (1979). Refernec in [19].

32- S.G. Kim, H. Asahi, M. Seta, J. Takizawa, S. Emura, R. K. Soni, S. Gonda, and H. Tanoue, J.Appl.phys.**74** 579-585 (1993).

33- Ch. Zeller, B. Vinter, and G. Abstreiter. Phys. Rev. B **15** (1982).

UNIVERSITEIT VAN PRETORIA
UNIVERSITY OF PRETORIA
YUNIBESITHI YA PRETORIA

34- Two-Dimensional Systems, Hetrostructures, and Superlattices by Gbauer, F. Kuchar, and H. Heinrich.

35- Classical Electrodynamics. Jackson. (PP 29).

36- H.W. Kunert, D.J. Brink, J. Matjila, T.S. Modise superlattice and microstructure, **25** 389 (1999).

37- Semiconductor material and device characterization, Dieter K. Schroder 1998.